UNIVERSITAT DE BARCELONA

A portable device for time-resolved fluorescence based on an array of CMOS SPADs with integrated microfluidics

Joan Canals Gil

UNIVERSITAT DE BARCELONA

A portable device for time-resolved fluorescence based on an array of CMOS SPADs with integrated microfluidics

Programa de doctorat en Enginyeria i Ciències Aplicades

Joan Canals Gil

Departament d'Enginyeria Electrònica i Biomèdica

Barcelona, Febrer 2020

Director i Tutor: Dr. Angel Diéguez Barrientos

Programa de Doctorat: Enginyeria i Ciències Aplicades

Línia de Recerca: Enginyeria Electrònica

Universitat de Barcelona

Departament d'Engineria Electrònica i Biomèdica

A portable device for time-resolved fluorescence based on an array of CMOS SPADs with integrated microfluidics

Doctoral dissertation in partial fulfillment of the requirements for the degree of Doctor of Philosophy in Engineering and Applied Sciences

by Joan Canals Gil

Barcelona, February 2020

Advisor: Dr. Angel Diéguez Barrientos

Doctoral program: Engineering and Applied Sciences

Research line: Electronic Engineering

Acknowledgments

I would like to thank Dr. Angel Dieguez for including me in VLSI design group since my early years in engineering, for his dedicated supervision, encouragement, advice, guidance, and confidence during all these years, and for finally compelling me to write this thesis after a decade working in the exciting world of research.

I am grateful to Dr. Oscar Alonso, and Nil Franch, who have been actively working in this project, for their work and the good times that we spent inside and outside the lab. I also would like to thank all the co-workers who have walked the laboratory during all these years from whom I have learned so much during this long journey, Sergio Moreno, Victor Moro, Lluís Freixes, Eva Vilella, Raimon Casanovas, Anna Arbat, Andreu Montiel, Andreu Sanuy, Jaime Punter, Jordi Colomer, and many others. Thanks guys for all the good, bad and awkward moments.

I must also acknowledge Dr. Anna Vilà and Dr. Mauricio Moreno for the time they spent with me in the cleanroom, for their guidance and support in the micro-fluidics manufacturing. Very special thanks to Dr. Anna Vilà for their kindly revision of the papers.

Thanks also to Dr. Julià López, Dr. Sergi Hernández, and Dr. Blas Garrido for being so generous with their time, letting me use the electro-optical bench and helping me with the SPAD spectral response characterization.

I must also thank the prototype lab staff, especially to Andres Romero who runs the wire bonding machine like nobody else.

Finally, I would like to thank my wife Anna for all. My kids who were born during the development of this thesis, and who have given me so many excuses to stop writing these lines. My friends who have supported me and are always there when I need them. Last but by no means least, I would like to thank my family. My mum, dad, and sister for their support through all my life and for encouraging me to pursue my goals.

Table of Contents

Abbreviations

ADC	Analog-to-Digital Converter
APD	Avalanche PhotoDiode
AP-SoC	All Programmable System-On-Chip
BJT	Bipolar Junction Transistor
CAD	Computer-Aided Design
CDC	Clock Domain Crossing
CLB	Configurable Logic Block
CMOS	Complementary Metal-Oxide-Semiconductor
DCR	Dark Count Rate
DNA	Deoxyribonucleic acid
FPGA	Field-Programmable Gate Array
FMC	FPGA Mezzanine Card
FR	Free-Running
FWHM	Full-Width at Half Maximum
HV-CMOS	High Voltage Complementary Metal-Oxide-Semiconductor
IR	InfraRed
IRF	Instrument Response Function
LED	Light-Emitting Diode
LSB	Least Significant Bit
PBS	Phosphate Buffer Saline
PCB	Printed Circuit Board
PCR	Polymerase Chain Reaction
PD	PhotoDiode
PDP	Photon Detection Probability
PDMS	Polydimethylsiloxane
PMT	PhotoMultiplier Tube
POC	Point-Of-Care
POCT	Point-Of-Care Testing
QDs	Quantum Dots

MCP	MicroChannel Plate
MOS	Metal–Oxide–Silicon
MOSFET	Metal–Oxide–Semiconductor Field-Effect Transistor
MSM	Metal-Semiconductor-Metal
RF	Radio Frequency
SNR	Signal-to-Noise Ratio
SPAD	Single-Photon Avalanche Diode
TAC	Time-to-Amplitude Converter
TCSPC	Time-Correlated Single-Photon Counting
TDC	Time-to-Digital Converter
TDL	Tapped Delay Line
TG	Time-Gated
TIR	Total Reflection Index
UV	UltraViolet
USB	Universal Serial Bus
UART	Universal Asynchronous Receiver/Transmitter

Chapter 1

Introduction

Over the last two centuries, the discovery and understanding of the principle of fluorescence have provided new means of characterizing physical, biological, and chemical processes in a non-invasive manner. Fluorescence spectroscopy has become one of the most powerful and widely applied methods in life sciences, from fundamental research to clinical applications due to its high sensitivity and robust selectivity through targeted labeling of biological samples [1].

Traditionally, molecular analysis is performed in laboratories equipped with expensive instrumentation with trained personnel responsible for testing. Samples are usually collected and sent to the specialized laboratory to be analyzed, taking several hours to complete a single test. This paradigm has been changing in the last decades, as biosensor technology has become as accurate as desktop instruments, providing results in much shorter periods and also being portable, moving the diagnostic tests gradually out of the central laboratory and into testing sites closer to the point-of-care (POC) in a cost-effective way.

However, despite the inherent advantages of fluorescence lifetime spectroscopy applied to molecular diagnosis, it is only in the last decade that POC devices are being developed based on fluorescence detection, due to the challenge of realizing high-performance, portable, and low-cost spectroscopic sensors on an industrial scale.

1.1 Quick Overview of Fluorescence Measurement

In fluorescence bioassays, samples are labeled using fluorescent dyes (e.g., rhodamines and quantum dots (QDs)) that absorb an excitation light and emit fluorescence at a longer wavelength. This fluorescence emission is detected and quantified to give a quantitative measurement of the analyte.

Fluorescence measurements can be broadly classified into two types: steady-state and time-resolved measurements. Steady-state measurements, the most common type, are those performed with constant illumination and observation. The labeled sample is illuminated with a continuous beam of light, and the intensity or emission spectrum is recorded (Figure 1.1). Because of the nanosecond timescale of fluorescence, most measurements are steady-state measurements. When the sample is first exposed to light, steady-state is reached almost instantaneously. In time-resolved fluorescence measurement, the sample is exposed to a pulse of light, typically shorter than the fluorescence decay time (Figure 1.1). The intensity decay of the emission is then recorded with a high-speed detection system working on the nanosecond timescale [2].

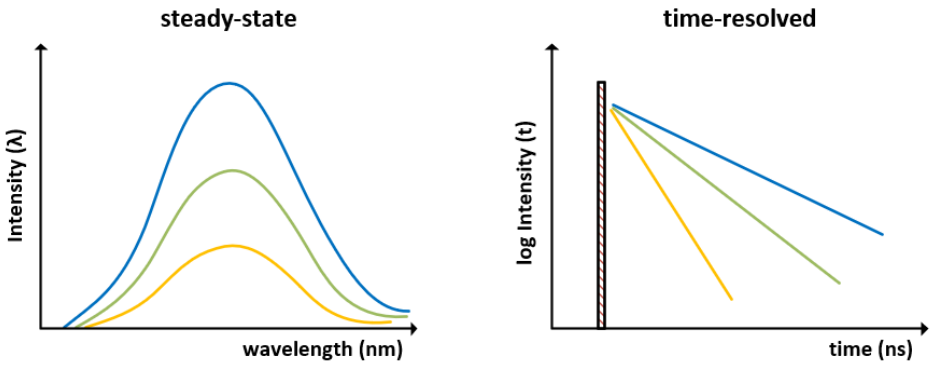

Figure 1.1 Comparison of steady-state and time-resolved fluorescence spectroscopy. Image adapted from [2].

Time-resolved fluorescence measurements are particularly useful in distinguishing target molecules from the fluorescent background, and differentiating between spectrally overlapping samples which exhibit different lifetime properties [3, 4]. Moreover, exploiting the time-dependent nature of fluorescence provides more

information about the molecular environment of the fluorophore than steady-state measurements. Since many macromolecular events occur at the same time scale as the fluorescence decay, its lifetime depends on rotational diffusion, resonance-energy transfer, and the dynamic quenching of molecules. Therefore, fluorescence lifetime measurements have become a common technique for observing biomolecular interactions [5, 6]. Among the different techniques used in time-resolved fluorescence, time-correlated single photon counting (TCSPC) and time-gated (TG) methods have been shown to be very efficient and robust for the imaging of biological specimens [7].

The TCSPC technique is based on the repetitive, precisely recording of the time elapsed between the excitation pulse and the detection of a single emission photon. Multiple pulses are used to construct a histogram of the number of detected photon counts as a function of time, providing the probability distribution of the fluorophore emission (Figure 1.2) [8]. TCSPC systems have high time resolution at the expense of long data acquisition because less than one photon is detected per excitation pulse. This low photon-counting rate is required to avoid the pileup effect, which distorts the TCSPC data to the earlier times, making the decay look faster than it is [9]. In the simplest case, the fluorescence decay curve is a mono-exponential process, given by equation 1.1.

$$I(t) = I_0 e^{-t/\tau} \tag{1.1}$$

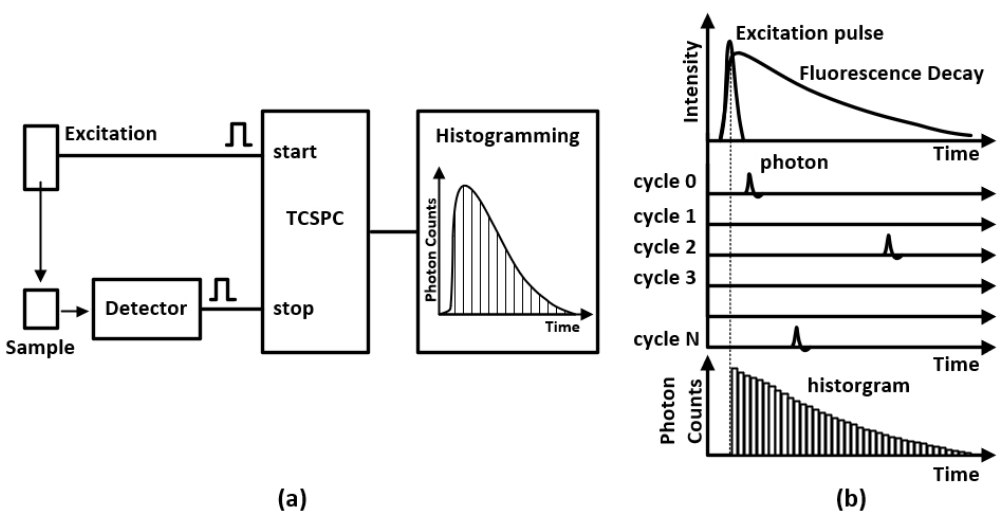

Figure 1.2 Time-correlated single photon counting (TCSPC) operation principle. (a) System schematic. (b) Timing diagram of the multicycle start-stop events.

where I_o is fluorescence intensity immediately after excitation, and τ is the fluorescence lifetime. Nevertheless, most fluorescence decays are multi-exponential. Furthermore, the observed decay is the convolution of the emission function with the instrument response function (IRF). An ideal system should have an IRF with the width of the incident pulse. However, nonideal real detection systems and electronics result in the broadening of the IRF, where the signal becomes exponential after the IRF drops to a negligible level [8].

Alternatively, the TG detection is achieved by means of gated photodetectors such as intensified CCD cameras (ICCD), photomultiplier tubes (PMTs), high-speed microchannel plates (MCPs), or avalanche photodiodes (APDs). After the excitation pulse, only the photons that arrive within specified time windows are detected. The fluorescence decay curve can be measured either within several time gates or by time gate scanning. In the first case, two-time gates are enough to measure mono-exponential fluorescence decay, whereas for multi-exponential decay more time gates are required [10]. For mono-exponential fluorescence decays the lifetime is calculated as,

$$\tau = \Delta T / \ln (I_1/I_2) \qquad (1.2)$$

where ΔT is the time interval between two time gates with equal width, the I_1 and I_2 are the intensity measured within the time gates, respectively (Figure 1.3.a). When $\Delta T=2.5\tau$ the error in the lifetime estimation is the smallest [11].

In the TG scanning technique, a narrow time gate (typically tens of picoseconds) synchronized with the excitation pulse is used to sweep the fluorescence profile.

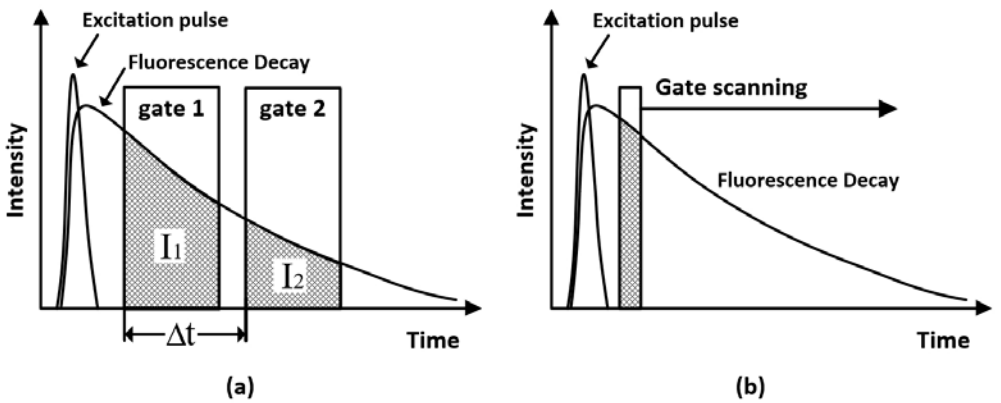

Figure 1.3 The two methods of time-gated fluorescence detection. (a) the fluorescence decay curve and (b) the time gate scanning.

After measuring the intensity at one time-position, the time gate shifts automatically by a known time step and the measure is repeated, thus building the histogram, as shown in Figure 1.3.b. However, since scanning a narrow gate over the signal rejects the majority of the detected photons, the gate scan technique has poor efficiency compared to TCSPC [12].

Since the fluorescent emission is typically orders of magnitude weaker than the excitation light, and the decay times of most of the used labels are in the nanosecond range (~ 1-100 ns), both methods require narrow excitation pulses, and an extremely sensitive and fast sensor, as well as a high-performance timing circuit.

At present, most of the commercial fluorescence lifetime measurement instruments are typically bulky and expensive, targeting laboratory-based applications [13, 14] (Figure 1.4). This is due to two key technological limitations in the electronic and optical domains. First, the picosecond temporal resolution requires complex signal processing electronics, as well as the generation of narrow excitation optical pulses (of few picoseconds FWHM). Second, a complex optomechanical system involving lenses and filters is applied to focus and extract the fluorescence emission light, generally a microscope. However, using modern technologies and manufacturing techniques, such instrumentation can now be made in complete integrated systems, with the potential for volume production and ubiquitous utility (e.g., in point-of-care).

Figure 1.4 Commercially available fluorescence lifetime instruments; (left) MicroTime 100, an upright time-resolved fluorescence microscope from PicoQuant; (right) DeltaPro™ lifetime system from Horiba Scientific.

1.2 Towards Miniaturization of Fluorescence Lifetime Instrumentation

In order to minimize system size, cost, and improve throughput, the limitations mentioned above must be overcome.

In terms of electronics, complementary metal-oxide-semiconductor (CMOS) technology enables low-cost and large-scale integration of transistors and physical sensing materials on tiny chips (e.g., <1cm^2), seamlessly combining the two key functions of biosensors: transducing and signal processing [15]. For more than a decade, single-photon avalanche diodes (SPADs) have been integrated into CMOS circuits, significantly improving time-resolved fluorescence measurements [16–18]. Thousands of SPADs can be integrated into the same substrate alongside signal conditioning and processing electronics [19, 20], estimating the fluorescence lifetime on-chip [21] and achieving excellent timing resolution down to 30 ps [15]. Moreover, large quantities of sensors can be integrated to improve performance further. This is particularly important in multiplexed bioassay tools that study multiple interactions simultaneously with a single measurement. The different target molecules are identified by labeling the analyte, which guarantees the robustness of the system in complex biological media. This has been used, for example, in CMOS chips for fluorescence and time-resolved fluorescence

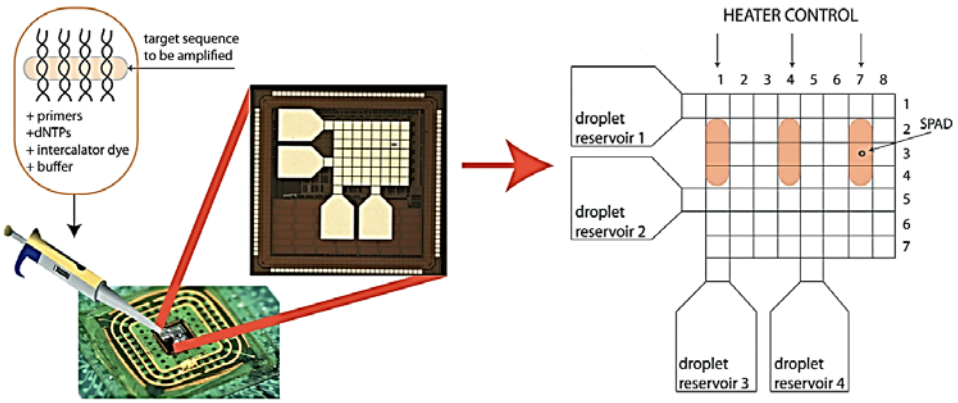

Figure 1.5 Droplets of the test sequence and PCR reagents are delivered to one of four reservoirs on the chip. The entire surface is heated with three heaters at columns 1 4, and 7, thermal cycling all test droplets simultaneously. PCR progression is monitored using an integrated SPAD at pixel (3, 7) [27].

measurements in DNA-microarrays for genomic analysis [22–26]. Besides, CMOS technology allows integrating additional functions such as electrowetting droplet transport and heaters with photodetector and processing electronics to build a complete quantitative-PCR lab-on-a-chip (Figure 1.5) as demonstrated by Norian et al. in [27].

In terms of optics, to reduce the cost and size of the fluorescence-based systems, several groups have used 3-D printing to develop custom optical instrumentation using low-cost lenses systems [28]. Forcucci et al. developed an all-plastic miniature fluorescence microscope for multiplexed bead-based assays with limit detection comparable to a commercially available desktop system [29]. In an attempt to simplify the optical path, Camou et al. [30] presented two optical fibers directly inserted into microfluidic channels that end with a polydimethylsiloxane (PDMS) 2D optical lens, which results in a cheap microchip with self-aligned fibers put near to the microfluidic channel. However, the use of fiber optics to guide both excitation light and fluorescence emission is discouraging due to the limitation and complexity that it introduces in the miniaturization of the system [31]. A better approach, in terms of miniaturization, consists in the use of a microfluidic chip with integrated lenses [32–34] or waveguides [35–37] guiding the excitation light to the sample and harvesting the fluorescence emission towards the detector. Comprehensive reviews about micro-optics for microfluidic analytical applications can be found in the literature [38–40]. Roulet et al. in [41] reported a multilayer system combining microfluidic (wet-etched in a Borofloat 33 (Pyrex) glass wafer) and micro-optical elements for fluorescence detection. The system is composed of the combination of refractive photoresist microlens arrays, chromium aperture arrays, and microchannels of 60 µm wide and 25 µm deep. Figure 1.6 shows the detection principle of the system, where the misaligned entrance aperture and exit apertures reject the excitation beam from the detector.

In order to eliminate the optical elements from the system, contact sensing must be adopted. Contact sensing is a method in which samples are placed near the sensor surface without intermediate optics. Contact sensing has proven to be optically efficient in a large variety of fluorescence-based applications, such as spectroscopy of moving particles [36], DNA analysis [23], cell manipulation process [42], high-resolution fluorescence imaging [43], and detecting cellular functions [44]. There are two approaches to contact sensing: on-chip and off-chip.

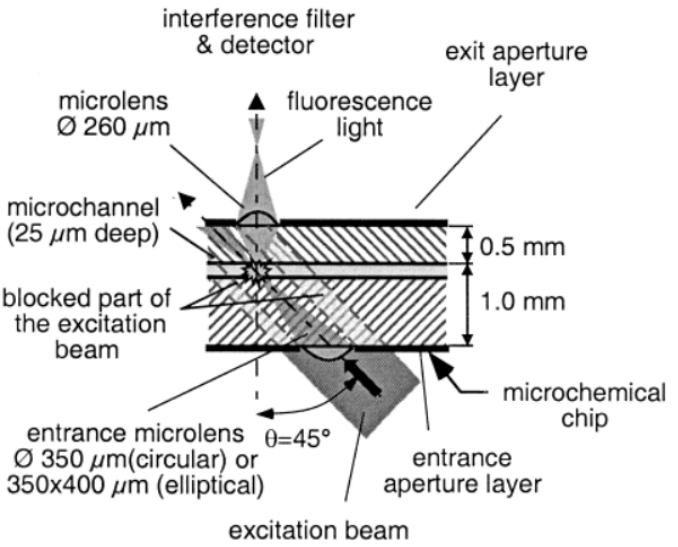

Figure 1.6 Cross-section view of the detection microsystem with an illustration of the detection principle [41].

In the on-chip devices, the analyte is placed directly on the built-in passivation layer atop the CMOS chip by means of a droplet [27] or embedded microchannel [45], usually making the sensor a single-use component. In contrast, the off-chip approach uses a disposable substrate (e.g., thin coverslip) or microfluidics chip [44] placed as close as possible to the sensor surface.

However, in both approaches of contact sensing, a way to cut or dim the excitation light source is necessary before reaching the sensor. Traditionally, high-performance optical blocking filters with optical densities between (4-6) are used at the expense of moving the sample away from the sensor. An example of the off-chip approach is [46], where the interference filter used is fabricated using a 60-layer coating of Nb_2O_5 and SiO_2 vapor-deposited onto a micro sheet of fused silica substrate, resulting in a total filter thickness of approximately 100 μm with an optical density of 6. In on-chip devices, the filters are generally fabricated directly on the surface of a CMOS die and present a thickness of a few microns depending on the optical density desired [47] (e.g., 88 single layers of SiO_2 / TiO_2 have a thickness about 4.5 μm with optical density >5 [48]). In the literature, different strategies can be found to avoid the use of filters, almost all of them based on the separation of the optical path of the excitation light from that of the fluorescence. The first one is the use of micro-lenses embedded in the microchannel as in the case shown

above. This approach is only applicable to off-chip systems. Another strategy is to use total internal reflection (TIR) to reflect the excitation beam after interacting with the sample volume [49]. The TIR process occurs at the bottom side of the sample device. The fluorescent emission from the excited sample does not entirely obey TIR and therefore can be directly detected without the use of any lenses. Another example of the application of TIR is shown in [36], where a fluidic waveguide is used, guiding the light within the target-containing medium, thereby enabling an extended interaction length. However, in fluorescence lifetime measurements where narrow pulses of light are used to excite the sample, the TG technique can be used to reject the excitation light source from the measurement window (Figure 1.7), eliminating the need to use filters or modify the optical path. In the literature, there are several examples of the application of TG to remove the excitation light from the observation window [27, 50–54].

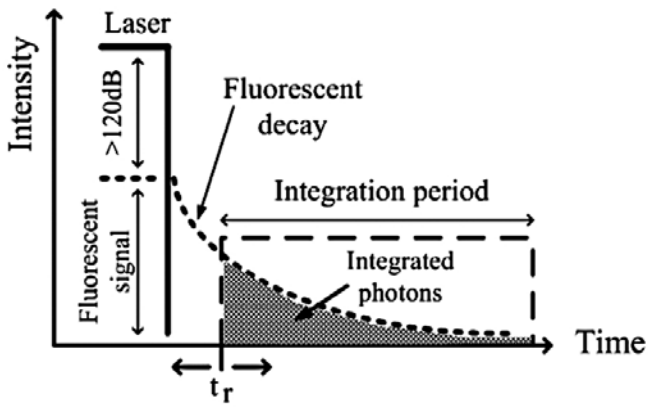

Figure 1.7 Diagram of excitation/background rejection in fluorescence detection by means of TG, where *tr* denotes the start of the integration period (or observation window) after the excitation light has been turned off [52].

Since Araki and Misawa in 1995 [55] demonstrated the use of commercially available blue InGaN/AlGaN LEDs for fluorescence lifetime measurement, the capacity to integrate LEDs arrays to perform multiplexed bioassay fluorescence analysis has been studied [56]. In [57] and [58], Rae et al. presented a highly integrated and portable micro-systems based on a micro-LEDs array and SPAD arrays. Both systems include an array of CMOS integrated LED drivers capable of generating narrow optical pulses of 777 ps and 1.2 ns at FWHM, respectively, but larger pules (2.5 ns and 8 ns respectively) were required for exciting the sample. In [57], a two-chips approach was reported (Figure 1.8.a). An 8×8 array of

AlInGaN blue micro-pixelated LED is bump-bonded to the LED drivers array chip, while the fluorescence emission is detected by a second, vertically-opposed 16×4 array of SPADs fabricated in HV-CMOS technology with in-pixel time-gated photon counting circuitry. Despite the array configuration, the device is only operated as a single spot device, however, with the addition of micro-optics, the pixelated excitation and detection devices have the potential to act as a 2-D sensor array. In [58], a single-chip microsystem capable of performing fluorescence lifetime measurements several by implementing an array of LED drivers and SPADs detectors in the same CMOS chip, in conjunction with external TCSPC hardware, to accurately measure the fluorescence lifetime of commercially available quantum dot samples. The CMOS chip was bump bonded to a 4×16 array of AlInGaN UV micro-LEDs (Figure 1.8.b). The sample was placed directly on top of the excitation source and detector array, minimizing the dimensions of the system. However, the system lacks a filter or TG circuit to reject the excitation light from the observation window, which blinds the corresponding SPAD. Indeed, the LED emission forces to use the SPAD situated eight rows away (800 µm, from the emitting LED), reducing considerably the signal-to-noise ratio (SNR). Both systems demonstrated that the use of 2D arrays of excitation sources and detectors eliminates the need for complex optical alignment in off-chip contact sensing approaches.

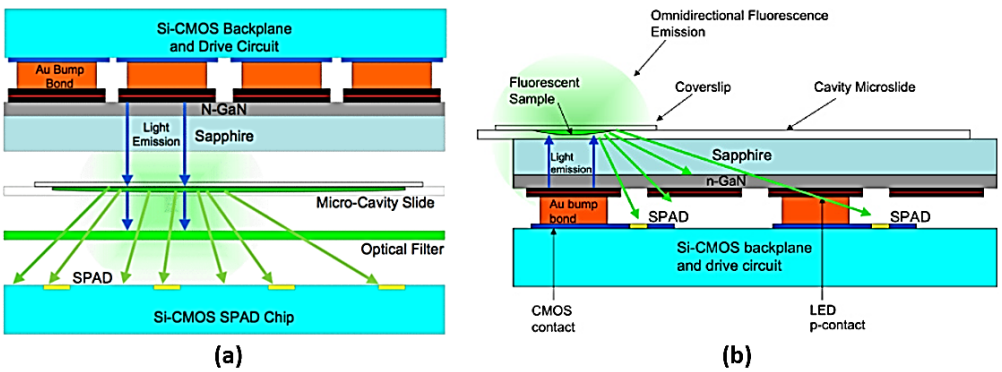

Figure 1.8 Cross-section of the integrated fluorescence micro-systems by Rae et al. (a) Two chips sandwich structure where the fluorescent sample is placed micro-cavity slide, and a long-pass filter eliminates the excitation light [57]. (b) Stack-up structure with the sample in the microcavity slide placed over the sapphire substrate of the LED array chip. The transparent sapphire substrate allows the fluorescence emission to pass and reach the SPAD below [58].

1.3 Fluorescence Lifetime Microdevices

Microdevices are defined as systems that employ analytical components and techniques at the micro- and nanoscopic scale, including microfilters, microchannels, microarrays, micropumps, microvalves, and microelectronics. These mechanical and electrical components can be integrated onto chips to analyze and control biological samples at the micro- and nano-scale [59–63]. Microdevices enable clinical and environmental diagnostics to be miniaturized for use at the POC.

The development of reliable and self-contained POC testing (POCT) devices depends on the integration of these key technologies on an industrial scale [64]. As seen above, for a time-resolved fluorescence-based contact sensing device, this includes microelectronics with microfluidics, highly sensitive detection methods, and the light source [65]. Many sensor platforms are demonstrated in the academic literature exhibiting different levels of system integration. Table 1.1 gives an overview of some developed contact sensing fluorescence lifetime measurement micro-systems.

Table 1.1 Overview of contact sensing fluorescence lifetime measurement micro-systems.

Ref.	Sensor	Excitation	Filter	Processing	Analyte	Sample Handling	Integration level
[25]	CMOS Differential PD array	external gain-switched laser	No	on-chip TG TIA+ADC	DNA-QDs	on-chip surface	Medium/ High
[27]	CMOS SPAD	external fianium laser	No	on-chip TG	DNA	on-chip surface	Medium/ High
[50]	CMOS SPAD array	external pulsed LD	No	on-chip TG	DNA	on-chip surface	Medium
[51]	CMOS SPAD array	external pulsed LD	No	on-chip TG scanning	QDs	off-chip µ-capillary	Medium/ High
[66]	SPAD	external pulsed LED	Yes excitation	external TCSPC	Coumarin 6	LCW	Low
[57]	CMOS SPAD array	integrated µLED array	Yes emission	on-chip TG	QDs	off-chip µ-cavity	High
[58]	CMOS SPAD array	integrated µLED array	No	external TCSPC	QDs	off-chip µ-cavity	Medium

LD: laser diode; LCW: liquid-core waveguide

A significant item of the table is the fact that most of the micro-systems use an external excitation source, usually a commercial picosecond laser with the corresponding bulky driving electronics. This is because the majority focuses on showing the sensor and the integrated timing electronics performance and forgets the integration of the light source into the system. Besides, most microsystems implement the TG technique that provides a strong rejection of excitation light combined with a picosecond pulsed light source.

Huang et al. [25] use an array of differential photodiodes with in-pixel TG [52] to detect DNA hybridization labeled with QDs (48 ns lifetime) on the functionalized chip surface, achieving resolutions down to 100 pM with a theoric limit of 7.2 pM according to sensor characterization [52]. In [27], Norian et al. integrate a miniaturized quantitative-PCR instrument using a TG SPAD for fluorescence monitoring of the reaction. The integrated SPAD had a detection limit of 1.7 µM at 50ºC, allowing the quantification of target DNA with more than four orders of magnitude of dynamic range and sensitivities down to a single copy per droplet. Maruyama et al. [50] present an all-digital TG CMOS fluorescence imager of 128x128 SPAD array with one-bit memory per pixel used as a DNA detector, reporting the detection of 9 µM of Cy5 labeled DNA molecules. The sample was placed directly on the sensor coated in PDMS to sustain the fluorescence sample and avoid short circuits. In a different approach, Stoppa et al. [51] report the use of a capillary to hold the sample over the chip surface, detecting concentrations down to 1.64 µM of DNA labeled with QDs (CdSe/ZnS, 15-20 ns lifetime). The implemented TG circuit includes a 17-bit counter to accumulate the time-gate counts on-chip. In [66], Wei et al present a liquid-core waveguide (LCW) TCSPC instrument implemented completely with off-the-shelf components. The LCW with the liquid sample in the core provides, strong interaction between the excitation and the sample, high excitation rejection based on TIR principle, and sample holding. A detection limit of 5 nM was obtained, measuring the fluorescence lifetime of Coumarin 6 (2.5 ns), using a commercial pulsed LED (nanoLED-455, Horiba). Finally, Rae et al. report two SPAD-based micro-systems that use AlInGaN micro-LED arrays bump-bonded to CMOS driving arrays [57, 58] (Figure 1.8). Both micro-systems were tested, measuring QDs samples of 57 µM concentration. Two factors caused this low performance in detection. First, the low optical power provided by the micro-LEDs (550 µW in DC operation) results in weak fluorescence emission. Second, the lack of TG operation of the sensor to

remove the excitation light that forces to increase the sample-detector distance to accommodate an emission filter in [57] and minimize the light from the LED in [58].

Despite the high-level of integration seen in different micro-systems, external control is required to control the measurement procedure, for data post-processing, user interface for data visualization, system configuration, and calibration. This external control is usually implemented by means of field-programmable gate array (FPGA) [57, 67] or microcontrollers [66].

1.4 Point of Care Testing Applications

Microdevices have been used in biosensors technologies at academic, and commercial settings detecting a range of analytes using many types of biological fluids [68–70]. These studies have demonstrated assays with better performance than benchtop tests with regards to speed, portability, sensitivity, and multiplexing [71–74]. The classes of analytes detected range from the proteins and nucleic acids to cells, and small molecules [63, 75]. Hence, different POCT devices have to be developed and applied depending on the target analyte and the final application.

In the literature, there are complete reviews of POCT applications and devices [74, 75, 84, 76–83], most of them focusing on clinical applications but not limited to it. The applications of POCT in healthcare refers to the performance of biochemical, hematological, coagulation, or molecular diagnostic tests at or near a patient, which allow for immediate clinical management decisions to be made [81]. In [85] Luppa et al. provide a list with the clinical relevant or evolving parameters to be analyzed, including but not limited to them: metabolic parameters (small metabolite and enzymes), inflammation markers (e.g., CRP and PCT), infectious agents (e.g., HIV, Influenza A & B), organ-specific injury (e.g., cardiac markers cTnT/cTnI, CK-MB, myoglobin), hematological parameters (e.g., hemoglobin, hematocrit, and CO-oximetry), humoral and cellular coagulation markers (e.g., PT/INT and D-Dimer), cancer markers (e.g., HER2 for breast cancer or prostate-specific antigen for prostate cancer) among many others.

Although initially, the POCT was considered as a supplement of the central laboratory. Now, POCT is a growing trend often used as the sole diagnostic approach

in a wide range of areas and especially in developing countries [86]. The POCT is continually increasing the test portfolio due to the high interest of the healthcare stakeholders [87]. Table 1.2 from [76] gives an overview of the meanwhile very extensive POCT spectrum, focused on medical use.

Table 1.2 Areas of POCT application (table extracted from [76]).

Within the hospital setting		**Outside the hospital setting**
Area of application	Intensive care unit Operating room/recovery room Delivery room/neonatal ward Lung function tests Invasive radiology Emergency room Specialized outpatients Diabetic care ward	Emergency physician (also for disaster control or in the military setting) Private practitioners (practice, house calls) Medical services Sports medicine Outpatient care Home care Pharmacy For forensic drug screening For patient self-monitoring (blood glucose, clotting)
Criteria for use	Outside the central laboratory's regular service hours Hospitals without laboratory	

The diagnostic market is full of devices to analyze one or several of these parameters, providing results in a few seconds or minutes. The design of the instrument varies from compact handheld devices (e.g. glucose measuring devices [88] and i-STAT a multiparameter analyzer by Abbot [89, 90], Figure 1.9) to desktop devices that integrate complex analytical systems (e.g. DiagCore a syndromic testing analyzer by Stat-Dx [91–93], Figure 1.9). Table 1.3 shows examples of POCT devices to be used in clinical settings adapted from [81]. The spectrum of the methods covers a range from simple test strips to complex immunochemical assays such as nucleic acid testing. In general, these POCT devices are almost completely automated and require only a few simple steps to move from sample preparation to the test result. The technology used in the different devices mostly derives from the analytical systems used in central laboratories but optimized for miniaturization, speed of analysis, multiplexing, and user-friendliness [76]. The miniaturization was possible by the development of microdevices and biosensors technology, performing analysis in a closed plastic test carrier with the reagents pre-charged and ready-to-use [94, 95]. The detection is usually implemented on an external reader through either electrochemical or optical methods. In the latter case, a large role is played by fluorescence or reflection spectroscopy [96–98].

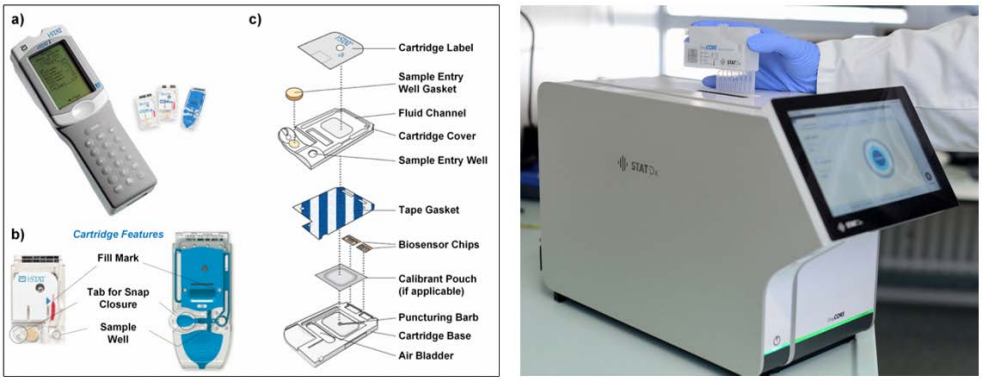

Figure 1.9 At left, the i-STAT system including (a) i-STAT handheld device (b) Photography of two different iSTAT cartridges and (c) Schematic explosion view of the i-STAT cartridges (image from [99]). At right, photography of the DiagCore system of Stat-Dx.

Clinically relevant POCT analyzers can be separated into six groups according to the critical review published by Luppa et al [81]. Table 1.4 from [81] provides the device categorization based on the instruments´ practical use in POCT. The measuring mode and the underlying detection principle are mentioned.

Table 1.3 Examples of POCT devices to be used in clinical settings (table adapted from [81]).

Parameter	Device for applications	Company
Hemoglobin A1C	Afinion POC HbA1c Analyzer D-100 InnovaStar Quo-Lab cobas b 101 DCA Vantage	Alere (Waltham, MA, USA) Bio-Rad (Hercules, CA, USA) DiaSys (Holzheim, Germany) EKF Diagnostics (Barleben, Germany) Roche Diagnostics (Mannheim, Germany) Siemens Healthcare Diagnostics (Eschborn, Germany)
Clinical chemistry parameters	Piccolo express Triage Meter Pro, Afinion AS100, Cholestech LDX Spotchem EZ SP-4430, BA PA-4140, D-Concept Smart 700/340, Cube c 111 Dri-Chem NX500 Labgeo PT10	Abaxis (Union City, CA, USA) Alere Arkray (Nakagyo-ku, Kyoto, Japan) Eurolyser Diagnostica (Salzburg, Austria) Roche Diagnostics Fujifilm (Minato, Japan) Samsung (Daegu, South Korea)
Urine stick and sediment	Urisys 1100 Clinitek Status+ URiSCAN Optima II	Roche Diagnostics Siemens Healthcare Diagnostics YD Diagnostics (Kyunggi-Do, South Korea)
Hematological parameters	QBC STAR Dry Hematology Analyzer HemoSpeed Hemocue WBC system Micros CRP, 60 Labgeo HC10 PocH-100i	Drucker Diagnostics (Port Matilda, PA, USA) EKF Diagnostics Hemocue America (Brea, CA, USA) Horiba Medical (Irvine, CA, USA) Samsung Sysmex (Kobe, Japan)
Immunoassay analytes	i-STAT Triage, Heart Check System m16	Abbott (Abbott Park, IL, USA) Alere Edan (Nanshan Shenzhen, China)

Table 1.3 *(Continued)*

Parameter	Device for applications	Company
Immunoassay analytes	Pathfast LSI	Medience Corporation (Tokyo, Japan)
	FREND system	NanoEnTek (Guro-gu, South Korea)
	Minicare I-20	Philips (Amsterdam, The Netherlands)
	AQT90	Radiometer (Copenhagen, Denmark)
	ReLIA mini	ReLIA Diagnostics (San Francisco, CA, USA)
	RAMP Reader	Response Biomedical (Vancouver, BC, Canada)
	Labgeo IB10	Samsung
	MICT	MagnaBioScience (San Diego, CA, USA)Randox
	Evidence MULTISTAT	Laboratories (Crumlin, UK)
	Stratus CS 200	200 Siemens Healthcare Diagnostics
	Getein 1100	Getein Biotech (Nanjing, China)
	Astute140 (NephroCheck)	Astute Medical (San Diego, CA, USA)
	Meritas POC Analyzer	Trinity Biotech (Bray, Co Wicklow, Ireland)
Blood gas analysis (BGA)	AVOXimeter 4000	Accriva Diagnostics (San Diego, CA, USA)
	Epoc	Alere
	i15	Edan (Nanshan Shenzhen, China)
	GEM Premier 3500, 4000	Instrumentation Laboratory (Bedford, MA, USA)
	Irma TRUpoint	ITC Medical (San Francisco, CA, USA)
	EasyBloodGas, EasyStat	Medica Corp. (Bedford, MA, USA)
	Stat Profile Critical Care, Xpress, Stat Profile Prime	Nova Biomedical (Waltham, MA, USA)
	OPTI CCA-TS2, OPTI R	OPTI Medical Systems (Roswell, GA, USA)
	ABL5, ABL800 FLEX, ABL80 FLEX, ABL90 FLEX	Radiometer
	cobas b 123, cobas b 221	Roche Diagnostics
	Rapidlab 800, 248/348EX, 1200, Rapidpoint 400/405	Siemens Healthcare Diagnostics
Coagulation Testing	Hemochron Jr. Signature+, Elite	Accriva Diagnostics
	INRatio2	Alere
Humoral Coagulation	Cascade POC, Abrazo	Helena (Beaumont, TX, USA)
	CoaguChek CS Pro, Plus	Roche Diagnostics
	Xprecia Stride	Siemens Healthcare Diagnostics
	qLabs Coag Panel 2	Micropoint Biotechnologies (Guangdong, China)
Thrombocyte function	Protime 3	ICT Medical
	VerifyNow	Accriva Diagnostics
	PFA 100/200	Siemens Healthcare Diagnostics
	Sonoclot	Sienco (Arvada, CO, USA)
	ROTEM	TEM International (Munich, Germany)
Continuous (glucose) monitoring	Freestyle Navigator II, (Freestyle libre)	Abbott
	HG1-c C8	Medisensors (San Jose, CA, USA)
	Glucowatch G2	Biographer Cygnus Inc. (Redwood City, CA, USA)
	Dexcom Seven Plus, G4	Dexcom (San Diego, CA, USA)
	Symphony	Echo Therapeutics (Iselin, NJ, USA)
	GlucoTrack	Integrity Applications (Ashkelon, Israel)
	Gardian RT	Medtronic (Minneapolis, MN, USA)
	Glucoday	Menarini (Florence, Italy)
	OrSense NBM-200G	OrSense (Petah-Tikva, Israel)
Molecular biology-based detection of Infectiousc agents (Nucleic Acid Test-POCT)	Alere i	Alere
	BioFire FilmArray	bioMerieux (Marcy-l'Étoile, France)
	GeneXpert, GeneXpert Omni	Cepheid (Sunnyvale, CA, USA)
	Unyvero	Curetis (Holzgerlingen, Germany)
	EnigmaML	Enigma Diagnostics (Salisbury, Wiltshire UK)
	LIAT	Roche Diagnostics
	GeneSTAT	DxNA (St. George, UT, USA)
	DiagCore	Stat-Dx (Barcelona, Spain)

IMPORTANT NOTE: The list is non-comprehensive. Due to the enormous numbers of different systems and manufacturers, it is impossible to list POCT devices for whole blood glucose (WBG), other qualitative strip-based POCT methods (e.g., pregnancy testing) and lateral flow assays for the detection of infectious agents.

Table 1.4 Categorization of POCT devices according to the underlying technological principles [81].

Type	Description	Principles	Examples for applications
1. Qualitative strip-based methods	These qualitative tests discriminate between plus/minus results and are mostly strip-based. The signaling is often performed by simple visualization or by optical detection modes performed by use of a simple readout device.	The detection principles span from chemical indicator reactions to immunological reactions, such as immunochromatography (performed as lateral flow assays, LFA [100, 101]).	Applications are urinary pregnancy testing, detection of blood in stool, urine dipstick analyses, detection of infectious agents in swab material, drug screening.
2. Unit-use analyzers	All these systems use unit-use test strips and whole blood obtained by finger prick making them most convenient for the patient. These test strips are one-use articles.	Simplest form of a quantitative POCT device. Detection modalities: optical or electrochemical or micromechanical (coagulation), with analyses taking place on the respective test strips. The reader is used to read out the strips, where the reaction has already taken place.	Glucometers for both home and the hospital POCT stations. Vitamin K-antagonist therapy monitoring by use of INR POCT devices [102].
3a. Benchtop analyzers	These instruments are generally more complex than the unit-use machines and use different analytical principles.	1. Spectrophotometric substrate and enzyme activity measurement 2. Hematological particle counting. 3. Immunoassay	Spectrophotometry/reflectometry is usually applied for clinical chemistry parameters. The analyzers use different test formats: E.g. centrifugal disks, test strips or cassette analyzers. Hematological multichannel analyzers use conventional techniques but are tailored for POCT needs. Immunological multichannel devices are also tailored for the special POCT applications. They use antibody-based immunoassay methodologies
3b. Benchtop blood gas analyzers (BGA) with CO-oximetry	These instruments are highly complex instruments for the measurement of various blood gas parameters inclusive CO-oximetry together with an electrochemical module for the analysis of electrolytes and metabolites	The CO-oximetry is a diode array multiwavelength spectrophotometry and analyzes the typical absorption spectra of the various hemoglobin (Hb) species. Many companies on the market have sophisticated oximetry units on board of their BGAs, having no counterpart in the central laboratory. Due to the fact that Hb species are found only inside the erythrocytes, some systems use a cell lysis step prior to the	The blood gas analyzers (BGA) use either potentiometric/amperometric or optical sensors for pH, pO_2 and pCO_2. Additional ion-sensitive electrodes for the measurement of electrolytes (Na^+, K^+, $Caion^{++}$, Mg^{++}) and other substrates (glucose, lactate, creatinine) are implemented. The analysis of the various Hb species by use of the CO-oximetry is performed in order to distinguish O_2–Hb (oxy-Hb) from other Hb

Table 1.4 *(Continued)*

Type	Description	Principles	Examples for applications
		spectrophotometry step, whereas others eliminate the erythrocyte-caused light scattering by applying matrix-assisted algorithms.	species and to determine the O_2–Hb-saturation: the percentage of O_2–Hb compared to the total amount of Hb, including CO–Hb, O_2–Hb, desoxygenated Hb (HHb with Fe^{2+}), and Met-Hb (HHb with Fe^{3+}).
4. Hemostaseological coagulation analyzers	These POCT compatible machines show high complexity. Although they are valid for use in POCT, only qualified personnel, such as trained technical assistants should operate them	The combined analysis of plasma clotting, thrombocyte function and fibrinolysis is termed viscoelastic coagulation tests	Systems for the determination of global humoral coagulation parameter, such as aPTT or PT/INR. Systems for the determination of thrombocyte function parameters: thrombelastometry, in vitro bleeding time, optical aggregometry
5. Continuous (glucose) monitoring	The most common example here is continuous glucose monitoring. Such analyzing and application systems are already available commercially. They are likely to replace the invasive, intravenous electrode by the minimally invasive location of a microdialysis catheter in subcutaneous tissue.	The systems using microdialyis are measuring low-molecular analytes by use of the same methodology as used for single measurements. Other non-invasive methods, such as microoperation or optical techniques in direct transcutaneous measurement of metabolic parameters, are atleastun like lytoprevail.	There are many systems available for continuous glucose monitoring. Other determinations of metabolites such as lactate or glycerol or BGA systems are still in their infancy.
6. Molecular biology-based devices for the detection of infectious agents	Molecular biology-based POCT devices for the detection of infectious agents	1. Qualitative test strips to detect infectious pathogens. The basic principle in most systems is immunochromatography (LFA). 2. There are devices using molecular biological methods (mostly the polymerase chain reaction, (qRT)-PCR, but also isothermal amplification techniques [103–105]) for POCT applications.	Infectious agents are bacteria, bacterial toxins and viruses. LFA measure specific microbial antigens (or more rarely, antibodies against bacterial/viral antigens) in the patient sample (urine, swab, whole blood), whereas with molecular diagnostics either specific DNA or RNA sequences are to be detected.

1.5 Thesis Motivation

The realization of combined high-performance, portable, and low-cost spectroscopic sensors remains a challenge. This work aims to develop a low-cost, robust, compact system for molecular diagnosis based on time-resolved fluorescence spectroscopy, which serves as a general-purpose platform for optical detection of a variety of biomarkers, bridging the gap between laboratory and the POC of the fluorescence lifetime based bioassays.

To overcome the limitations of current POC diagnosis systems based on time-resolved fluorescence measurement, different micro-technologies and techniques will be adapted and integrated. Specifically, it will be combined in an innovative approach in the fields of 1) high sensitivity imaging technology; 2) microfluidic technology; and 3) simple solid-state light sources as laser-diodes or LEDs (Figure 1.10).

A custom sensitive and fast SPAD-based detector combined with integrated microfluidics will enable performances comparable to desktop optical instruments with a measurement time of a few seconds. The integration of all these technologies will allow for an intrinsically robust, compact, mass-produced, and therefore low-cost final system.

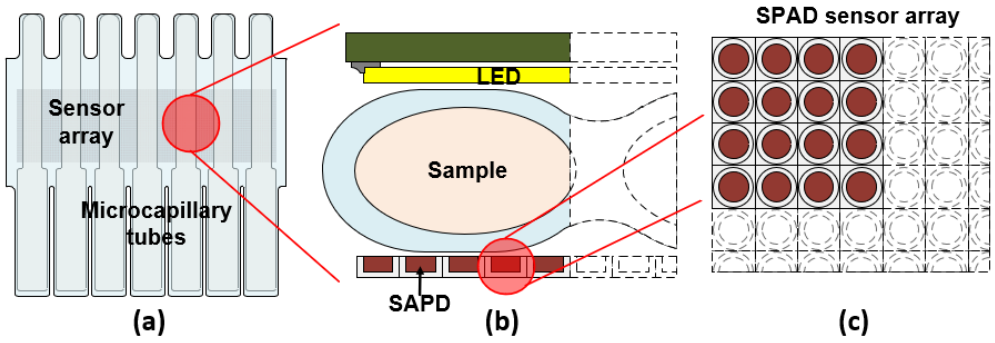

Figure 1.10 Initial schema of the proposed device. (a) The capillary pattern on the sensor matrix with liquid-pressure absorption. (b) Transversal section of the complete device, with the micro-fluid channel on the set of sensors and upper illumination. (c) Camera for molecular imaging based on SPAD detectors.

1.6 Organization of the Thesis

This thesis covers the design and characterization of a microfluidic device for time-resolved fluorescence based on an array of CMOS SPADs.

Chapter 2 introduces the SPAD detectors in terms of their basic performance parameters such as PDP, DCR, afterpulsing, and dead time. The chapter includes a review of their front end electronics, including basic quenching and recharge circuits, operation modes, and readout electronics. Finally, the design and characterization of the two SPAD-based sensor circuits designed in HV-CMOS 0.18 µm standard process are described.

The sample handling is addressed in Chapter 3, where a custom PDMS microfluidic chip is designed as a removable cartridge to place the sample over the sensor chip. The tolerances during the fabrication, as well as mass-production alternatives to the PDMS are discussed.

In Chapter 4, through a critical review of published work aimed at sub-nanosecond optical pulse generation using LEDs and laser diodes, two driving circuits are selected and implemented to drive a 405 nm laser diode as the excitation source. The chapter also includes the design and characterization of the timing electronics implemented in an FPGA to perform fluorescence lifetime measurements. In these measurements, one of the SPAD sensor circuits described in Chapter 2 is used.

After, Chapter 5 describes how these elements were brought together to create a compact system for fluorescence lifetime measurement. Two versions of the device are presented. The first one uses the SPAD-based circuit without any processing electronics, measuring the arrival time of photons and reconstructing the histogram off-chip. The second one uses the SPAD sensor with histogramming-in-pixel capabilities. A demonstration of the ability of each system to excite a fluorescence sample and capture the resulting decomposition curve is provided and discussed.

Finally, the conclusion section summarizes the most significant results presented over the different chapters of this thesis to achieve the initial goal.

1.7 Contributions

The contributions of this thesis are:

1) SPAD-based micro-system design oriented to off-chip contact sensing for fluorescence lifetime measurements.

The design of each element of the proposed microsystem was oriented to achieve high integration and easy assembly of the contact detection device. The geometry of the sensor chip (SPAD arrays size, arrays configurations, arrays-contact pads layouts, and SPAD size) was designed together with its packaging and the microfluidic chip, in order to allow the straightforward stacking of the microfluidic cartridge and the sensor array without any alignment procedure to perform fluorescence lifetime contact measurements (sections 2.2, 3.2 and 5.2). Moreover, the device implementes the TG technique to remove the excitation light form the measurement window avoinding the use of filters. The implemented micro-system was able to measure concentrations of QDs as low as 62.5 nM in a volume of 20 nl (section 5.4.1.2).

2) SPAD based pixel with analog histogramming circuit on-chip.

We presented a novel approach in which the fluorescence decay histogram is obtained directly on-chip in the analog domain by generating successive timing windows with an area-efficient design (section 2.2.3.3). The complete characterization of the circuit is found in section 2.2.3.4. This circuit has been implemented in a micro-system to measure concentrations of QDs (section 5.4.2).

This result has been patented under patent number PCT/EP2016/075211, 2017.

Chapter 2

CMOS SPAD Integration

The selection of the sensor to perform time-resolved fluorescence measurements is an important decision that determines the level of integration of the system. Traditional single-photon detectors based on the non-solid state form, as PMTs or high-speed MCPs, can provide high fill factor and good timing resolution, but they have many disadvantages: large size, vacuum-based operation, and high price. The alternative to these is the solid-state detectors. In particular, the single-photon avalanche diodes (SPADs), which, in addition to being able to detect single-photons with a sub-nanosecond temporal resolution, can be integrated with standard complementary metal-oxide-semiconductor (CMOS) technology.

The implementation of SPADs in CMOS technology opens new possibilities for the miniaturization of measurement instruments based on fluorescence and time-resolved fluorescence detection. Thousands of SPADs can be integrated into the same substrate alongside signal conditioning and processing electronics [19, 20], improving the cost and power consumption significantly [16, 17]. The selection of the CMOS technology node affects the performance of the detector in terms of sensitive, noise and fill factor [18]. In this thesis, the standard 0.18 µm HV-CMOS technology from Austria Micro-Systems (AMS) has been used to design a total of 3 SPAD-based sensor chips for fluorescence measurment. Since the two first chips were used to test basic SPAD structures and circuits in this technology, only the last implementation is presented because it includes all the circuits.

In this chapter, we discuss the design and characterization of the developed SPAD-based sensor chip aimed to measure the fluorescence decay rate of a variety of

fluorophores. Section 2.1 presents the SPAD sensors, its key parameters, and the front-end electronics required to perform fluorescence lifetime measurements. Finally, section 2.2 describes the sensor chip and the two implemented circuits to measure fluorescence lifetime with different levels of integration and their characterization.

2.1 Single-Photon Avalanche Diode in Standard CMOS Technologies

SPAD is an APD specifically designed to operate in Geiger-mode. The principle of operation relies on the impact ionization effect to generate a photon-triggered avalanche current pulse [106]. In standard CMOS technologies, SPADs can be achieved by different configurations of the p-n junction, being the most common a p+/n-well junction in a p substrate. Figure 2.1 shows the structure of SPAD in CMOS technology integrated for the first time by Rochas in 2003 [107]. This structure includes a guard ring of low doping p diffusion to prevent the premature edge breakdown of the device due to the high electric field [108].

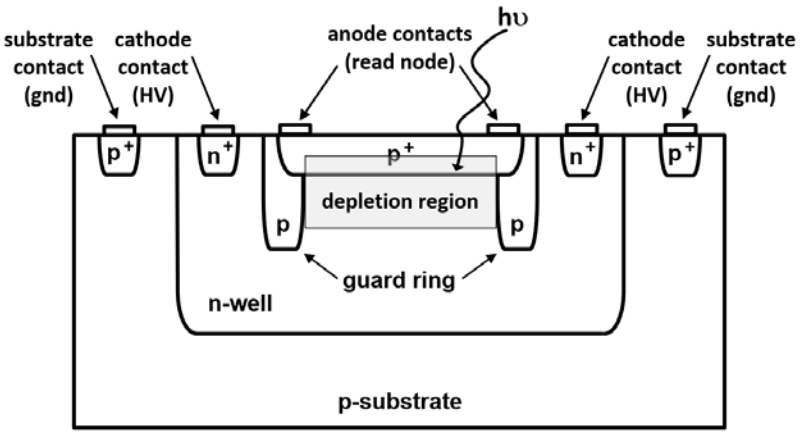

Figure 2.1 Cross-section diagram of the CMOS SPAD (also called Geiger-APD) structure proposed by Rochas in [107]. This structure has been successfully implemented in several CMOS processes (from 0.8 µm node to 90 nm node). The cross-section is not to scale.

The diode is reverse-biased at a high voltage (V_{HV}) beyond the breakdown voltage (V_{BD}) of the p-n junction by an overvoltage bias (V_{OV}), $V_{HH}=V_{BD}+V_{OV}$. In this regime, the electric field in the depletion region is so strong that a single electron-

hole pair generated by absorption of a photon can trigger, by impact ionization, a self-sustaining avalanche. As a result, a macroscopic current pulse is generated in a few picoseconds marking the arrival time of the detected photon. This time reference is used in TCSPC applications.

The fast avalanche pulses generated by the SPADs are typically discriminated through in-pixel electronics. The binary nature of the SPAD response makes unnecessary the use of preamplifiers, keeping the readout electronics as simple as a CMOS inverter that acts as avalanche discriminator and digitizer [51, 109–111]. Although, alternative implementations can be found in the literature such as voltage comparators [112, 113] or source follower circuits [114].

SPADs require additional electronics to quench the avalanche to prevent the destruction of the device, and a recharge circuit to get ready for the next detection. The quenching process is achieved by lowering the bias voltage below V_{BD}, and once the avalanche is halted, the recharge circuit raises the bias voltage above the V_{BD} again so that it can detect subsequent photons. In the literature, different techniques have been proposed to implement quenching and recharge mechanisms, partitioned in passive [107, 115–117] and active [118–121]. methods, although mixed approaches are commonly used [122–124]. In passive circuits, the reverse bias voltage applied to the device is self-adjusted through a resistive element in series with the sensor (Figure 2.2.a), providing a weak control over the quenching and recharge times. On the other hand, the active circuits sense the rise of the avalanche pulse, typically by comparing it to a threshold and react back on the SPAD bias to quickly quench the avalanche and reset the SPAD after a hold-off time.

Depending on the quenching and recharge circuits, the SPADs can be operated in either free-running (FR) or gated modes. In the former mode, the SPAD is always biased above the V_{BD} except for the quenching time after each avalanche. Hence, the SPAD is always ready to trigger an avalanche. However, for time-resolved fluorescence, where the expected signal arrival time is known in advance, it is more convenient to operate the SPADs in gated-mode, relegating the FR-mode to the characterization of performance parameters such as afterpulsing and crosstalk.

In gated operation, the sensor bias is kept below the V_{BD} and periodically increased to the desired V_{OV} for a defined time around the arrival time of the expected signal.

The gated operation is achieved using an active recharging circuit controlled by an external signal, which, in its simplest form, is implemented by a MOS transistor [110]. In addition to the gated operation also allows the suppression of the unwanted background signals [125].

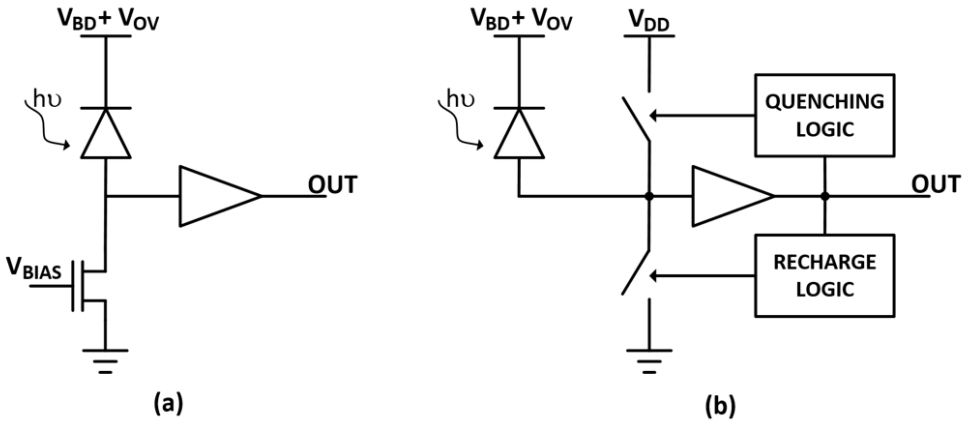

Figure 2.2 Basic schematic diagram of passive quenching and recharge circuits (a) and active quenching and active recharge circuits (b).

2.1.1 Key Parameters of SPADs

This section introduces the key performance parameters related to the underlying principles of SPAD that help to understand their technological limitations.

2.1.1.1 Shot Noise

Shot noise (or Poisson noise) is associated with the particle nature of light and is an inevitable noise source in photon-based measurement. The shot noise can be expressed as $\sigma_{shot\ noise}=\sqrt{signal}$ where *signal* refers to the number of detected photons.

2.1.1.2 Dead Time

The SPAD dead time is the time required to quench the avalanche and recharge the diode to its excess bias. During the dead time, the SPAD cannot process another event limiting the maximum count rate, and relegating SPADs to the MHz-GHz range depending on the technology node used [126].

2.1.1.3 Dark Count Rate

The noise of the SPAD, or dark noise, is the generation of primary carriers in the absence of illumination. These dark carriers can trigger avalanches that are impossible to distinguish from the photon-generated avalanches. The avalanches pulses generated by the dark carriers are known as dark counts and constitute an uncorrelated noise source. The average number of dark counts per second, or dark count rate (DCR), is used to characterize the intrinsic noise of the SPADs, fixing the detection limit (minimum detectable number of photos) of the device.

The primary sources of dark carriers are the thermal generation (explained by the Shockley-Read-Hall theory) and the band-to-band tunneling [106]. Both mechanisms are technological process dependent since the silicon is doped with impurities to assist the process of electron-hole pair generation. The traps created by these impurities act as intermediate states between the valence and conduction bands, increasing the probability of dark carriers generation. This is known as trap-assisted generation.

Consequently, the dark count noise depends on the doping profile (trap concentration), the electric field in the depletion region (revers bias overvoltage), as well as the temperature and the detection area. In particular, the thermal contribution increases with the overvoltage applied and it is proportional to the active area. The rise is due not only to the increase of the avalanche breakdown probability but also to the enlargement of the depletion region. Obviously, it is a function of the working temperature with exponential dependence [127]. In contrast, tunneling contribution has a weak dependence on temperature, but it is extremely dependent on the doping profile, and the overvoltage applied [128, 129].

The contributions of the two noise sources can be observed with a temperature sweep at a constant overvoltage. Above room temperature, the thermal generation dominates, and the dark count noise is roughly divided by two every 10ºC. While, at low temperatures, the tunneling becomes the dominant mechanism. The weights of these two contributions become equivalent at the corner temperature, which varies from -5ºC up to 10ºC depending on the technology process [130, 131]. Since the dependence of tunneling on the temperature is very weak, the dark count noise is only slightly decreased by lowering the temperature below the corner temperature. However, several techniques have been demonstrated to reduce the

DCR, such as special doping structures to reduce the trap-assisted tunneling, making more effective the cooling-based techniques to reduce the thermal generation contribution [132–134].

Therefore, depending on the technology process and SPAD structure, the DCR varies from 10^{-1} up to 10^{4} counts per second per micrometer square at room temperature [135].

2.1.1.4 Afterpulsing

Afterpulsing is a source of correlated noise that is related to the previous avalanche. When an avalanche is triggered, either by photon-generated carriers or by dark carriers, the depletion region is flooded with charge carriers, and some of them are temporarily trapped by the impurities (deep-level traps) in the semiconductor lattice. If one of these carriers is released after the sensor dead time, it can trigger a new avalanche pulse causing a noise count called afterpulse.

The afterpulsing probability depends on the quality of the fabrication process (which defines the concentration of deep-level traps) and the number of charge carriers generated during the avalanche [136]. Therefore, the afterpulsing probability can be almost completely avoided by extending the dead time of the SPAD with a hold off time longer than the lifetime of the trapped carriers. However, while operating at low temperatures minimizes the thermal contribution of the noise, lower operating temperatures increase the trap lifetimes, requiring longer dead times to reduce the afterpulsing effects [137]. Longer dead time affects the dynamic range limiting the SPAD performance [138].

More sophisticated techniques allow reducing the probability of afterpulsing without the need to increase the effective dead time of the SPAD. These techniques rely on the reduction of the charge carriers generated during the avalanche. The most extended are: decrease the parasitic capacitance seen by the sensing node of the SPAD [135] and use active quenching circuits for a premature deactivation of the avalanche [139].

Experimentally, the afterpulsing can be measured by collecting information on inter-arrival time between avalanches [140]. Typically the afterpulsing with active recharge is usually below 10% with dead times between 10 and 100 ns [17].

2.1.1.5 Crosstalk

Crosstalk is another source of correlated noise, which is present in SPADs arrays. An avalanche pulse in one detector can trigger a secondary avalanche in adjacent detectors. There are two types of crosstalk depending on the generation mechanism: the electrical crosstalk and the optical crosstalk. The electrical crosstalk occurs when secondary carriers diffuse to neighboring pixels and eventually trigger a new avalanche pulse. Nevertheless, isolating each SPAD in its well prevents the electrical crosstalk at expenses of the array fill factor.

On the other hand, optical crosstalk occurs due to impact ionization-based photon emission. The probability of both phenomena increases due to a large number of carriers generated during an avalanche. The optical crosstalk can be reduced by limiting the avalanche current and also by surrounding each detector with a deep thin trench filled with polysilicon [141].

In the same way as the afterpulsing, the crosstalk can be measured by collecting information on inter-arrival time between counts in the two adjacent pixels [142].

2.1.1.6 Photon Detection Probability

In SPADs, not all carriers generated in the depletion region might trigger an avalanche pulse. So, the SPADs sensitivity is measured as photon detection probability (PDP), which is the probability that an incident photon of a specific wavelength will trigger an avalanche. PDP can be expressed as

$$PDP = QE(\lambda) \cdot P_a \tag{2.1}$$

where *QE(λ)* is the quantum efficiency (ratio at which incident photons will produce electron-hole pairs) at a specific wavelength and P_a is the avalanche probability related to the ionization coefficient, which increases with the overvoltage applied at the p-n junction.

However, the PDP is experimentally calculated as,

$$PDP = \frac{total\ counts - noise\ counts}{incident\ photons}. \tag{2.2}$$

In CMOS implementations of SPADs, the sensitivity range is mainly in the visible spectrum (from near-ultraviolet to near-infrared) because of the absorption of light

in silicon [143]. Most of the current CMOS SPADs have a peak PDP at around 450 nm [144]. Peak PDP is comprised between 20% and 50%, with high diversity in spectral responsivity [145].

2.1.1.7 Timing Jitter

SPAD timing jitter is the statistical variation in the time between a photon reaching the sensor and the rising edge of the detector output pulse [143]. This elapsed time depends on the photodiode and the delay of the readout electronics. The timing jitter of the SPAD is attributed to the position and depth where the photon is absorbed in the depletion region and its statistical fluctuations. In particular, the variations in the diffusion time of the carriers generated outside the depletion region (this only occurs when working with lower wavelengths of incident light [146]), the transit time of the carriers inside the depletion region and the lateral diffusion of the avalanche process [147]. The timing jitter is measured at full-width at half maximum (FWHM) and is in the range of 30 ps to 200 ps [144, 145, 148].

2.1.1.8 Count Suppression and Pile-up Effects

Count suppression and pile-up effect are related to the photon-detection mechanism of SPAD. The photon-carries generated during the dead time or an avalanche process are not detected. So, the measured count rate (*m)* under an incident light with a photon rate (*i*) will never reach the theoretical rate (*n*) given by,

$$n = \left(1 + P_{after}\right)(PDP \cdot i + DCR) \tag{2.3}$$

where P_{after} is the afterpulsing probability.

Although the count suppression is closely related to the pile-up effect, the pile-up is more associated with timing measurements and the tendency to detect the early photons (fastest ones) in a detection cycle [149, 150]. In applications such as fluorescence lifetime measurement, the pile-up and dead time effects can distort the decay histogram reconstruction, and thereby the lifetime extracted. Single-photon statistics must be maintained low in order to minimize both effects. So, low count rates at the detector are required, typically below 5% of the excitation rate, but consistent results can be achieved with detection rates of 10 to 20% [12].

2.1.2 Front-End Electronics for Time-Resolved Fluorescence

For time-resolved fluorescence, besides the specific quenching and recharge mechanisms required to operate the SPAD in gated-mode, an accurate and precise timing electronics is required to reconstruct the decay histogram and calculate the lifetime. In the case of the TG technique, the timing circuits are in charge of generating the different time gates synchronized with the excitation pulse. On the other hand, the TCSPC requires timing circuits capable of measure the arrival time of the photons with respect to the excitation pulse at picosecond resolution. In both techniques, the binary nature of the SPAD only allows detecting one photon per excitation-detection cycle, making necessary, multiple cycles to perform one measurement.

2.1.2.1 Time-Gated Implementation

The TG is based on the generation of multiple windows to measure the intensity of the fluorescence decay curve at different times to calculate the fluorescence lifetime components. The simplest TG implementation consists of a detector, followed by a discriminator, feeding a logic gate, and a counter (Figure 2.3).

As mentioned above, the discriminator in the case of the SPAD sensor is a simple inverter or buffer that digitizes the avalanche current pulse. The discriminator output pulse is sent through a logic gate, and only the pulse within the gate pulse is counted. The gate pulses are triggered externally, e.g., by a reference synchronized with the excitation pulse. In practice, the time-gating is achieved by applying the gate pulse directly to the SPAD through the quenching and recharge circuits, which inhibit and restore it. Typically, the gate pulse is also combined with the first counter stage Figure 2.3. The input of the first flip-flop of the counter only changes when a clock event arrives within the gate pulse is high. This implementation has low detection and time performance. In terms of detection, the majority of the photons are rejected due to the small time gates. From the point of view time, the fluorescence lifetime calculation requires repeated measurements with different time gates. Thus, the total measurement time increases proportionally to the number of time gates needed.

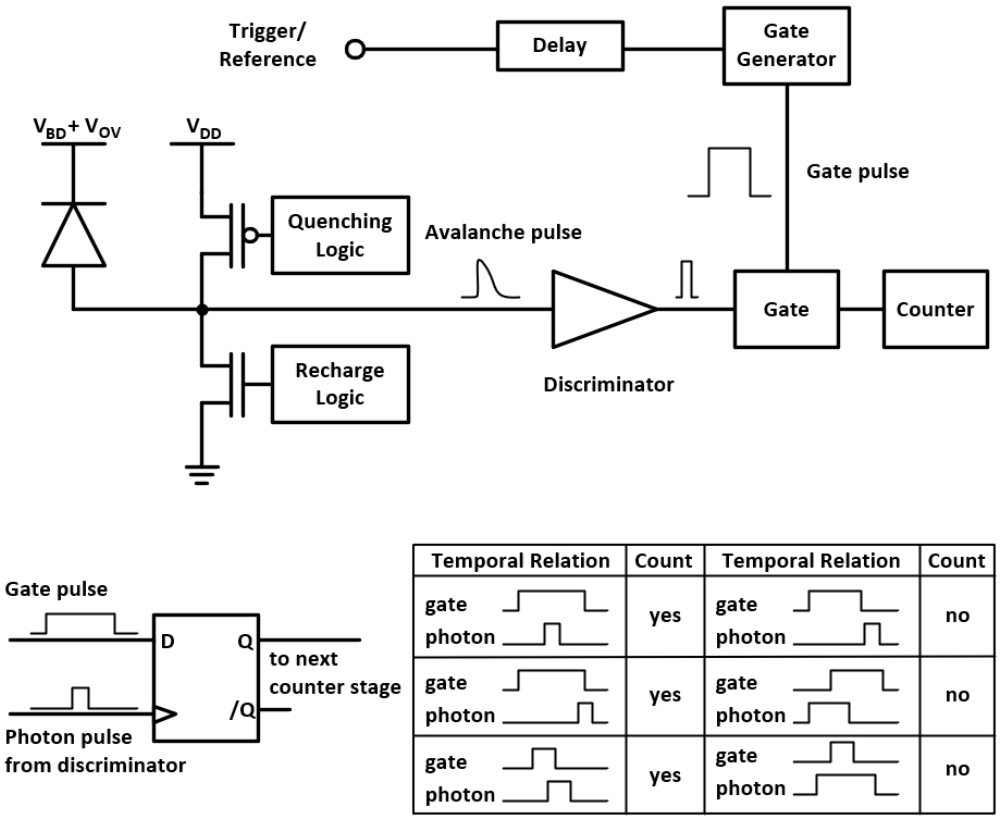

Figure 2.3 Time gated photon counting. Combination of the gate with the first counter stage. The circuit counts only photon pulses whose leading edge is within the gate pulse. Image adapted from [12].

The multiple-gate architecture (Figure 2.4) solve either the temporal and detection limitations, achieving counting efficiency close to one for fluorescence decay. This technique counts the photon pulses, using several gated counters in parallel. Each counter has its own gate delays and gate pulse generator. If the consecutive time gates completely cover the fluorescence lifetime, all the photons detected are counted. However, this technique is limited by the number of counters that can be integrated (2 up to 10). This limitation results in the undersampling of the decay signal. Fortunately, fluorescence decay curves are either single exponentials or a weighted sum of a few exponentials [12]. Thus, the lifetime components of decay functions can be determined from the photons collected in the multiple time gates. This makes the TG one of the standard techniques of fluorescence lifetime imaging (FLIM) [8, 151–153].

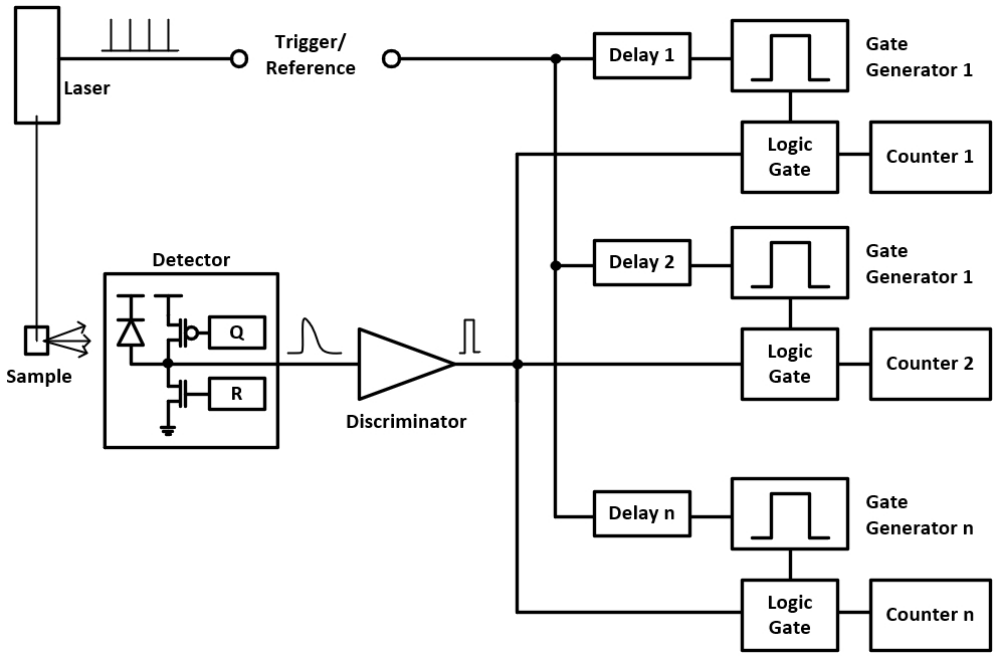

Figure 2.4 Time-gated photon counting with several parallel gates. Image adapted from [12].

2.1.2.2 TCSPC Implementation

The TCSPC is based on the measurement of the detection time of individual photons with respect to a temporal reference, e.g., usually the excitation pulse of fluorescence. There are several different time measurement techniques applicable to TCSPC.

The classic implementation is based on time-to-amplitude converter (TAC) is shown in Figure 2.5. The TAC generates an output voltage proportional to the time interval between the excitation and the detection pulses. It consists of switched current source charging a small capacitor with a constant current, thereby creating a linearly rising voltage ramp. When a photon is detected, the voltage value is amplified and converted by the ADC into a digital word. This word is the digital representation of the photon detection time that assigns the photon count to a corresponding histogram bin. In general, TAC-ADC implementations achieve high accuracy and can resolve time differences of a few ps [154], but have a limited temporal measurement range, and high-temperature dependence, leading to the need for temperature control or frequent re-calibration [2, 12]. Other issues of

TAC-ADC-based TCSPC are the long dead times due to the conversion time, and the differential nonlinearity (DNL) in the voltage ramp and in the ADC. The DNL becomes pronounced when attempt to shorten the dead time. Effectively such nonlinearities lead to nonuniformity of histogram bin widths and consequently to distortions of the recorded decay shapes [155].

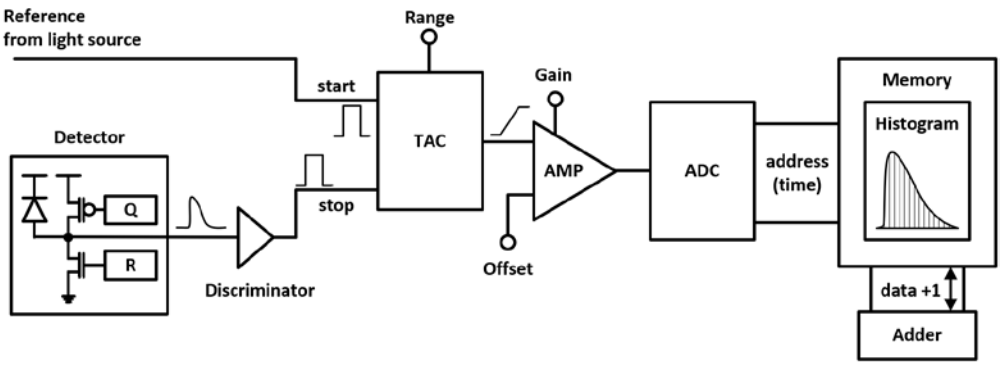

Figure 2.5 Classic TCSPC setup. Image adapted from [12].

In recent years, modern high-speed digital electronics are the means of choice to integrate direct digital time measurement circuits, namely time-to-digital converters (TDCs) [156]. This is mainly for three reasons: (1) the option to use crystal clocks, thereby eliminating calibration issues; (2) the possibility to obtain and process digital results directly; and (3) compatibility with modern production processes for cost-efficient monolithic integration [155].

There are many ways to implement the TDC reported in the literature [157–159]. The most common is by dividing time into coarse and fine measurements. Coarse measurement is achieved operating a counter at moderate clock speed, which sets the maximum range for the TDC measurement. The fine measurement is obtained by subdividing each clock period into smaller units using a tapped delay line (TDL). The TDL commonly consists of gates with the same delay, where the status of the start signal propagating through the delay line reflects the phase within the clock cycle (Figure 2.6).

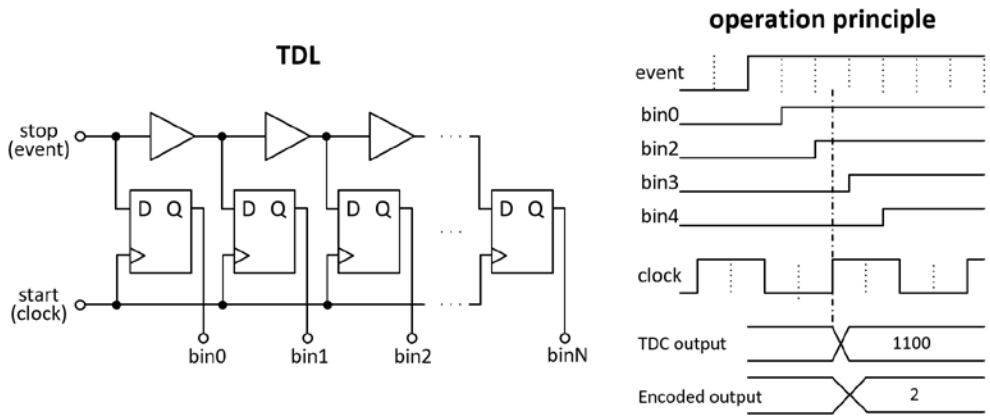

Figure 2.6 Example of a tapped delay line circuit for high-resolution TDCs (left). Example of the delay propagation and capture of the tapped delay line with 4 delay elements (right).

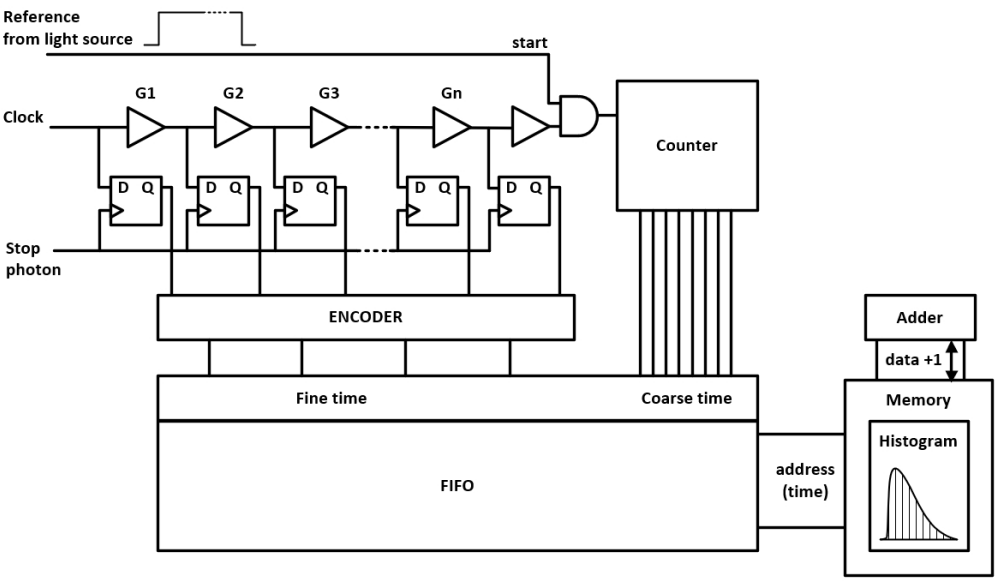

Figure 2.7 Architecture of digital TDC.

Figure 2.7 shows the operation principle of a TDC-based TCSPC. The measurement starts usually synchronized with the excitation light pulse, which enables the propagation of the start signal through the TDL. When an event is detected, the stop signal is activated simultaneously to the clock inputs of all the registers, capturing the status of TDL and disabling the counter. The encoded TDL output

combined with the counter value generates a binary code that represents the photon arrival time. As in the TAC-ADC approach, the resulting code addresses a memory location whose content is increased, thus building the histogram of the photon-emitted profile. The FIFO memory acts as a buffer, storing the times before assigning the photon count to the corresponding histogram bin. This allows reducing the total TDC dead time before the next measurement, increasing its throughput. A more efficient way to reduce the dead time is pipelining the output of the delay line [160] or alternating the input of the delay line (from rising to falling edge) [161] but at expenses of increasing the complexity of encoder logic in the latter case.

The TDCs issue is that the elements of the delay line are not uniform, causing a high differential nonlinearity (DNL). The DNL of the TDC can be characterized by conducting a density test [162]. A uniform time interval generator is attached to the TDC input. Ideally, this should generate all possible TDC output codes with the same probability (number of counts), as shown in Figure 2.8.a. However, the actual result is more similar to that presented in Figure 2.8.b. Delay elements with smaller delay present fewer counts in the histogram, while larger delays accumulate more.

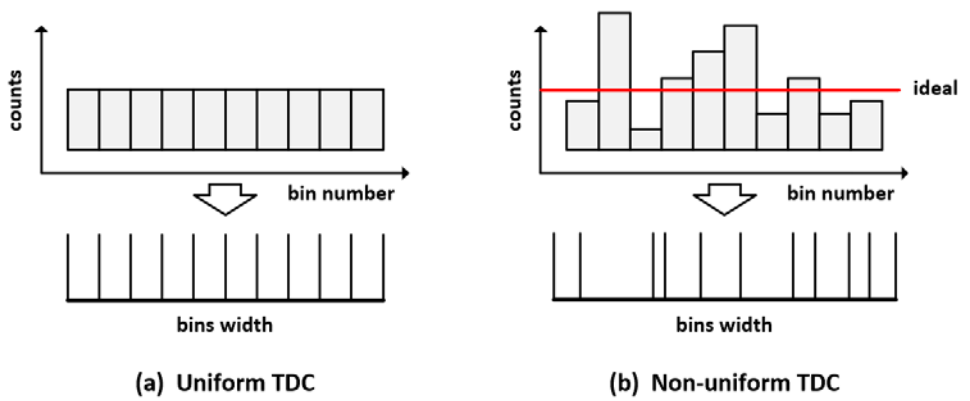

Figure 2.8 TDC density results for (a) uniform TDC and (b) nonuniform TDC.

The DNL of a bin *i* can be calculated as,

$$DNL(i) = C_i/E_i - 1 \tag{2.4}$$

where the C_i is the number of counts on that bin and E_i is the expected ideal number of counts per bin. The nonuniformity per bin is usually expressed in terms of least significant bits (LSBs), which is the resolution for the delay chain.

There are several origins for nonlinearities: uncertain logic delays, voltage and temperature variations during the measurement, routing mismatches and fabrication defects [163]. Many of those limitations can be controlled and compensated in ASIC-based TDCs during the design step by implementing tunable delay elements [164]. However, in FPGA implementations, the analog compensation is almost impossible, so it is usually done digitally after characterizing the nonlinearities. The accumulated DNL per bin, the integral nonlinearity (INL, 2.5), is used in FPGA-based TDC implementations as correcting vectors that are applied in real-time [160].

$$INL = \sum_{i=0}^{N-1} DNL(i). \tag{2.5}$$

The resolution and accuracy of the TDC depend on the implemented architecture, the clock speed used, and in the case of the FPGA implementations also the device performance. Several architectures exist, used both in ASIC and FPGA based designs, Vernier delay line [153], based on RS latches [165], high precision ring oscillators [166] and TDL based [140]. Although sub-ps resolution TDCs are reported in CMOS implementations [167–169], for TCPSC applications, TDCs are usually designed to target resolutions in 5–50 ps range [170–173] with tunable delay elements to minimize the DNL [174]. Besides, FPGA implementations of TDC are feasible, achieving resolutions down to 5 ps [166, 175] even with additional restriction, such as the limited resources and the predefined rigid structures.

2.1.2.3 State of the Art of SPAD-based TG and TCSPC

The literature shows different integration levels of time-resolved measurement techniques used to measure fluorescence lifetime. Stoppa et al., using a single SPAD measured fluorescence by TG with a sensor fabricated in a 0.35-µm CMOS process, and demonstrated a 10-ns observation window with 60-ps time-steps to displace the gating window generated with an external Field-Programmable Gate Array (FPGA) [51]. Rae et al. [58] used a 0.8 µm CMOS SPAD in conjunction with an external TCSPC hardware to resolve the lifetime of quantum dots. In

another study, Rae et al. [176] applied a similar system, but with an integrated TCSPC based on gating the SPAD response in the timeframes generated on-chip. Villa et al. [177] presented a smart pixel fabricated in a 0.35 µm CMOS process that integrated the Time-to-Digital Converter (TDC) into the pixel. Schwartz et al. demonstrated a fully-integrated SPAD imager for lifetime imaging, using an array of 64x64 pixels fabricated in a 0.35 µm CMOS process, and an on-chip TDC that performed both TCSPC and TG [178]. Additional functions have been incorporated into pixels, and larger cameras have been made. For example, the MEGAFRAME128 sensor fabricated in a 0.13 µm process [179] includes 160x128 SPAD-TDC pixels that generate over 20x109 10-bit timestamps per second with a timing resolution of 52 ps. Furthermore, the SwissSPAD [180] and SwissSPAD2 [181] sensors provide resolutions of 512x128 and 512x512 pixels, respectively, with a global gating circuit for accurate timing information that produces frame rates as high as 156 kfps and 97 kfps, respectively, with TG controlled externally [54].

Until quite recently, the histogram of the photon-arrival times was always reconstructed off-chip, with performances being limited by the readout bandwidth and the required power. The first chip classifying photon-arrival times on-chip was reported in [182]. In this 64x4 pixel array in a 0.35 µm process, fluorescence decay was estimated by binning in 4 externally programmable timeframes. Dutton at al. [183], evaluated the TDC for TCSPC to build the histogram from a combined 32x32 pixels single output. More recently, a 1024x8 line sensor in the 130nm process was reported to provide both TCSPC and histogramming functions [184]. The sensor integrates 512 TDCs of 16 b, which can pass time-event values to the histogramming modules of up to 204.8 ns in 32 bins of 10 b. The histograms can be chained to increase the dynamic range to 20 b, decreasing the number of bins to 16 [54].

In-pixel analog storage circuits can store data efficiently and save area [185–187], with a fixed charge injected into a capacitor after each photon is detected. An image sensor using this technique in a 0.35 µm CMOS process with 160×120 pixels, has been applied in time-resolved fluorescence microscopy [188]. Photons are measured by TG with the aid of an additional external programmable device. [54]

2.2 Design and Characterization of the CMOS SPAD Circuits

The SPAD sensor chip was implemented in a standard 0.18 µm HV-CMOS process. The 3.6 mm × 1.4 mm chip (Figure 2.9), contains two SPAD arrays circuits with different levels of integration, aimed to measure the fluorescence decay rate of a variety of fluorophores. The first one (highlighted in red) consists of a 1-D array of 10 SPAD pixels without any processing electronics, measuring the arrival time of photons and reconstructing the histogram off-chip. The second one (highlighted in green) consists of a 1-D array of 5 SPAD pixels with histogramming-in-pixel capabilities.

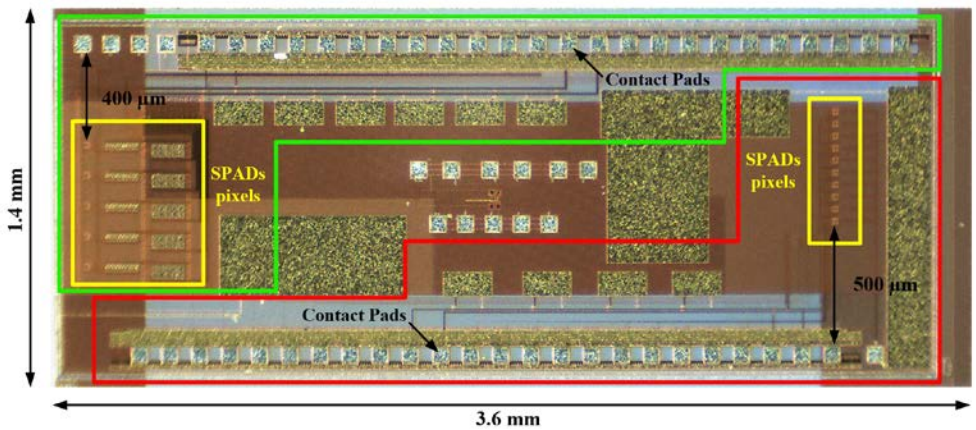

Figure 2.9 Photography of the ASIC with the two implemented 1-D array sensors highlighted. In red the 10 SPADs pixels array without processing electronics. In the opposite side of the chip highlighted in green, the 5 SPAD pixels array with histogramming in-pixel. Both circuits have the first SPAD pixel situated at 500 µm and 400 µm from the edge of their contact pads.

The geometry of the implemented circuits (SPAD arrays size, arrays configurations, arrays-contact pads layouts, and SPAD size) was designed together with its packaging and the microfluidic cartridge, in order to allow the straightforward stacking of the microfluidic cartridge and the die without any alignment procedure. The easiest way to align a microfluidic channel with a SPAD pixel is by using an array of n-pixels.

The array-contact pads layout of both circuits is similar but placed on opposite sides of the chip. All the connection pads are situated on the long edge of the chip,

with the 1-D SPAD array perpendicular to them. The first SPAD of each circuit is placed at 500 µm and 400 µm (for the 10 SPADs and 5 SPADs circuit, respectively) from the edge of the bonding pads. This layout configuration allows a simple microfluidic design, with one or three 100 µm microchannels crossing the SPAD arrays, as well as good margins its fabrication and for sensor packaging. However, since the microfluidics will slide over the SAPD array from one long side of the chip, only one circuit per chip can be used. Therefore, only one circuit will be wire-bond and encapsulated. Further details on microfluidic design and direct alignment in Chapter 3.

2.2.1 SPAD Pixel Design

The generic schematic diagram of SPAD pixels used in both circuits of the chip is shown in Figure 2.11.a. The basic pixel consists of a SPAD, active inhibition and active reset (recharge) switches to perform the time-gated operation and a readout circuit for the detection of low avalanche voltages.

The photodiode is based on the structure proposed by Rochas in [107], briefly described in section 2.1. The SPAD is implemented using a p+/n-tub junction on a p-substrate (Figure 2.10). The SPAD is done with a low doped ring surrounding the main diffusion (deep p-tub in Figure 2.10) to avoid the premature breakdown of the junctions at the edges. Moreover, the active area of the sensor has an octagonal shape with a 4 µm apothem (mimicking a round shape) to avoid electric field peaks at the edges. The active area is kept low to have a low dark count noise. The only reason to use SPADs with a larger active area would be to align them quickly, but this is solved by the use of 1-D array and the sensor packaging.

The deep n-tub cathode is biased at a $V_{HV}=V_{BD}+V_{OV}$, being V_{BD} the breakdown voltage of the sensor and V_{OV} the reverse bias overvoltage to operate in Geiger-mode. V_{BD} is ~11.7 V for this process and structure. Owing to the use of low-voltage transistors, the maximum V_{OV} that is possible to apply is $V_{DD} = 1.8\ V$ in this technology. The avalanches are sensed at the p+ anode due to its lower intrinsic capacitance to ground, which is beneficial in reducing the timing response, as well as the afterpulsing probability [189].

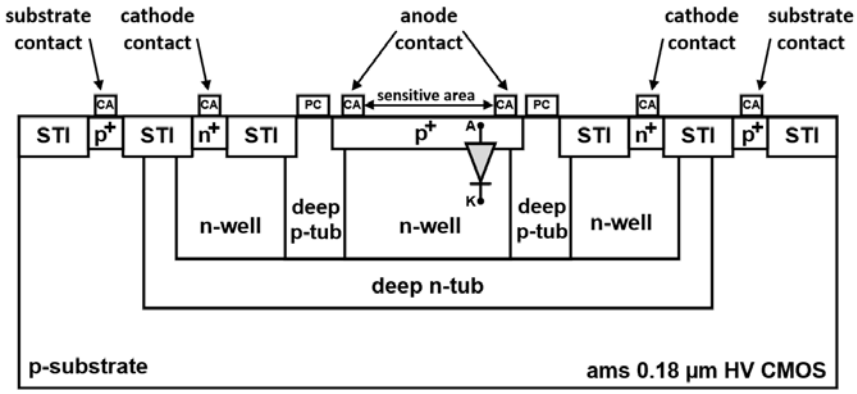

Figure 2.10 Cross-section of the SPAD designed and fabricated with 0.18 µm HV-CMOS process. STI stands for Shallow Trench Isolation, A for Anode, K for Cathode, PC for poly and CA for contact to metal layer 1. The cross-section is not to scale.

The SPAD is operated in gated-mode to partially eliminate the after-pulsing and reduce the probability of detecting dark counts instead of desired events [190]. Gated operation is accomplished by means of two signals (*RST* and *INH*) through MOS transistors Figure 2.11.

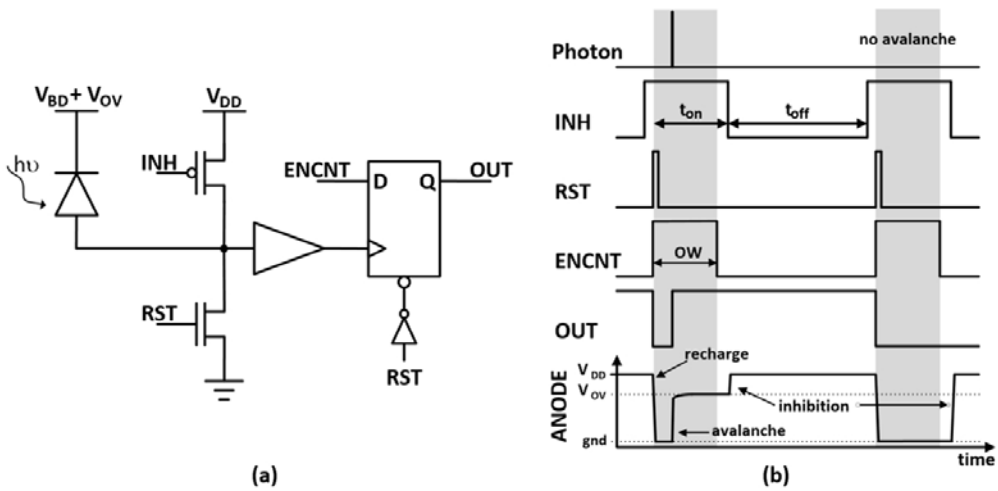

Figure 2.11 SPAD pixel schematic diagram of the SPAD pixel detector (a) and the timing diagram of waveforms to operate the time-gated SPAD pixel detector (b).

When the *RST* signal is set high, the sensor bias quickly increased up to $V_{BD}+V_{OV}$. Hence, the sensor is recharged, and the gate-on period starts. Given that

avalanches can still occur while the sensor is in the reset state, the *RST* pulse has to be as short as possible in order to avoid low resistive paths quenching the avalanche. In contrast, when the *INH* is set low, the polarization of the sensor is reduced to $V_{BD}+V_{OV}-V_{DD}$, with the $V_{OV} < V_{DD}$. The sensor is then gated-off, and it remains in this state until the next rising of the *RST* signal. When an avalanche is triggered, the self-sustained current, which flows through the junction, discharges the sensor capacitance and charges the parasitic capacitance of the sensing node. As a result, an analog voltage pulse is generated in the sensing node in picoseconds. When the voltage pulse reaches an amplitude equal to V_{OV}, the sensors bias drops down to V_{BD}, and the avalanche quenches. No active circuits aimed to quench the avalanches have been included in order to minimize the electronics.

The sensing node is connected to the two-stages readout electronics (Figure 2.11). The first stage is composed of a buffer that converts the analog voltage into a digital pulse. The second stage, a flip-flop, performs two tasks. The first is to determine the observation window (OW) within the gate-on period of SPAD (ton) through the ENCNT signal. The second is to keep the captured event during the gate-off period of the SPAD (toff), allowing to start the inhibit period (which should be held relatively large to avoid the afterpulsing) while the event is processed. Therefore, when an avalanche occurs, it is digitalized by the buffer and triggers the clock of the flip-flop, capturing the state of the ENCNT signal. If ENCNT is high, the event is transferred to the output (OUT), and it is maintained until the SPAD is reset, whereas if the ENCNT is low, the event is filtered.

2.2.2 Pixel Array with External Timing Circuit

2.2.2.1 Design

The general architecture of the first circuit is shown in Figure 2.12. The implemented circuit consists of a 1-D array of 10 SPAD pixels with a 50 µm pitch. Each SPAD pixel has its digital output, whereas the control signals and the bias voltage are common to the 10 SPADs. The control signals (*RST*, *INH,* and *ENCNT*) can be generated internally by triggering the *START* signal (Figure 2.12) or externally with integrated multiplexers. When signal generation is internal, the pulse width of the *RST, INH,* and *ENCNT* are fixed to 300ps, 13ns, and 10ns, respectively. The

timing of the generated signals is generated with chains of inverters and NAND gates.

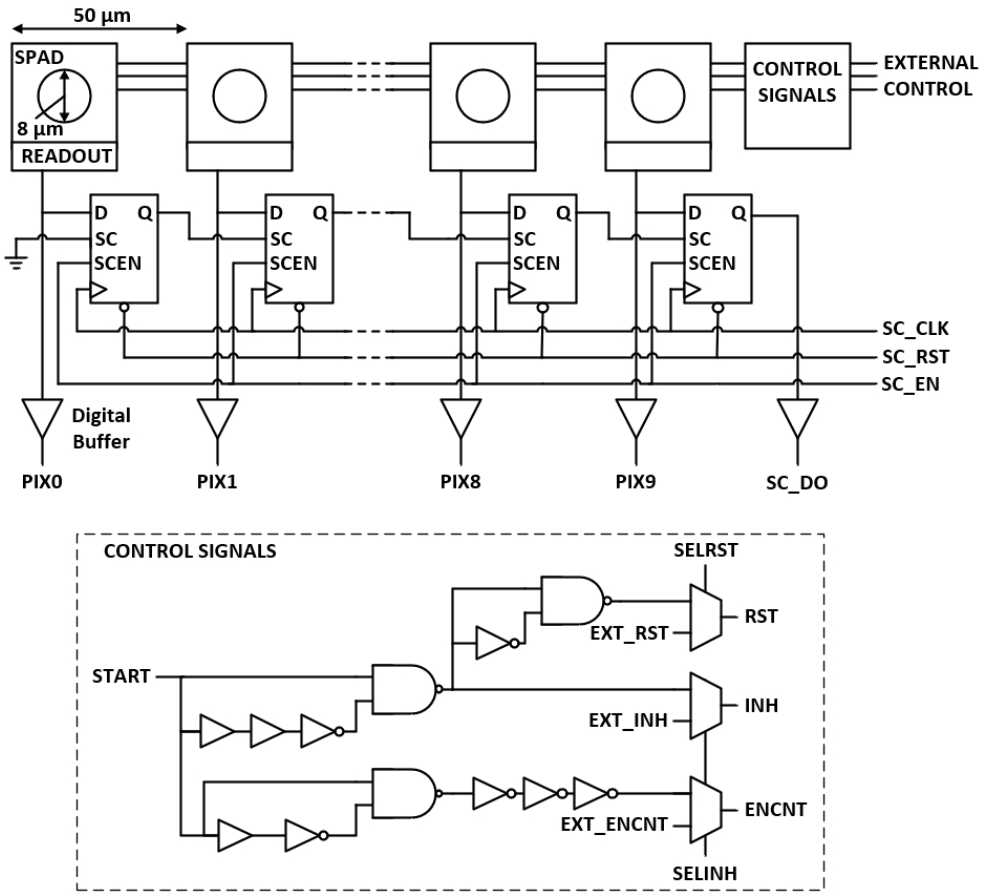

Figure 2.12 Architecture diagram of the 10-pixel, and a detail of the simplified schematic of the control signals generation circuit.

Besides the parallel output of the 10 SPADs, the circuit allows the serial output of the in-pixel registered values by using a scan flip-flops connected in daisy-chain mode, thus reducing the number of connections required in intensity measurement applications.

2.2.2.2 SPAD Detector Characterization

The 10-pixels sensor array circuit was used to characterize the SPAD detector. The chip was connected to a custom printed circuit board (PCB), which includes

the additional electronics necessary to power the device. A Zynq-7020 AP-SoC FPGA (from now on Z-7020) development board was used to generate the control signals (*RST*, *INH*, and *ENCNT*) that are necessary to operate and read out the pixels. The FPGA was also used to count off-chip the number of pulses generated by the detectors, to measure their arrival time, and to manage the communication with a computer via a USB.

DCR was measured on 13 sensor chips, to take into account its variability over different SPADs. Figure 2.13 shows the cumulative plot of the DCR at 1.1 V, 1.4 V, and 1.7 V of overvoltage at room temperature. Almost 70% of the pixels had a dark count rate lower than 8 kHz (at V_{OV} = 1.4 V), which is in line with other works [129, 191]. Figure 2.14 shows a typical dark count profile of the SPAD sensor array at normal operating conditions for different overvoltages.

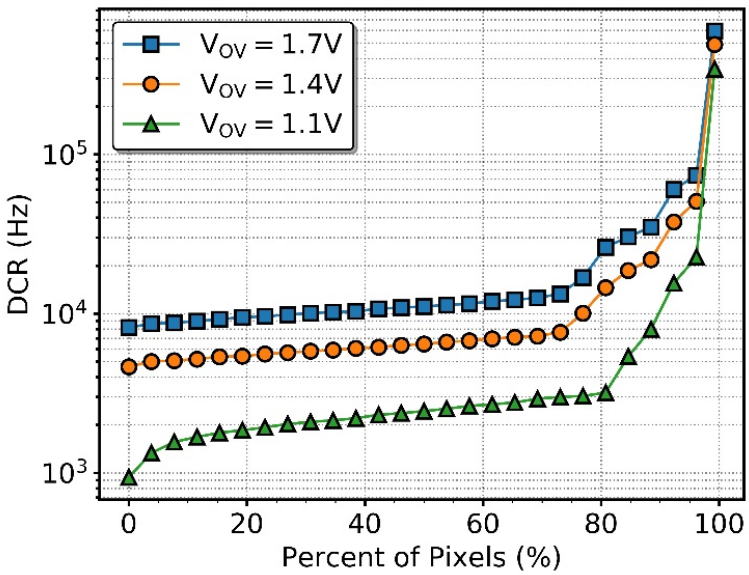

Figure 2.13 Dark count rate distribution measured across the SPAD array of 13 chips at 1.1 V, 1.4 V, and 1.7 V of overvoltage and room temperature with a maximum relative error of 0.5%.

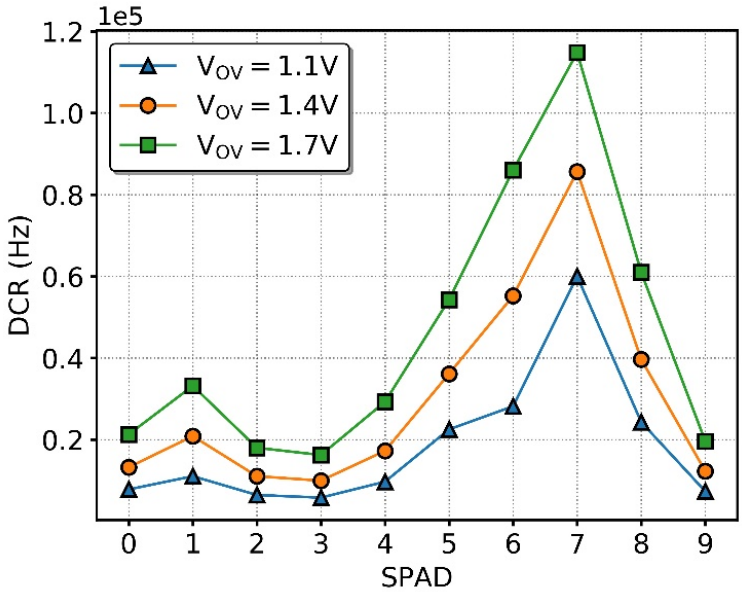

Figure 2.14 Dark count rate profile (with a maximum relative error of 0.5%) of the 1-D SPAD sensor array at 1.1 V, 1.4 V and 1.7 V of overvoltage and room temperature.

The PDP spectral response of the SPAD was measured using an electro-optical bench composed by a white-light source, a monochromator filter, and a calibrated reference detector. Figure 2.15 shows the PDP of a single SPAD in a wavelength range 300–1000 nm at 1.1 V, 1.4 V, and 1.7 V of overvoltage at room temperature. In good agreement, with other works such as [192]. The SPAD presented a good efficiency over the visible range with a maximum of 40% at about 480 nm (at V_{OV} = 1.4 V).

The afterpulsing was measured as the interarrival times between pulses operating the SPAD in FR mode and dark environment. Figure 2.16 shows the inter-avalanche time histogram for 1.4 V of overvoltage at room temperature. These sensors show almost negligible afterpulsing (<0.2%), which is in line with other works [192] and can be avoided almost entirely with 200 ns of off time.

The timing jitter for these sensors was expected to be below 80 ps for 1.4 V of overvoltage and 8 µm SPAD size, accordingly with similar SPADs found in the literature [192].

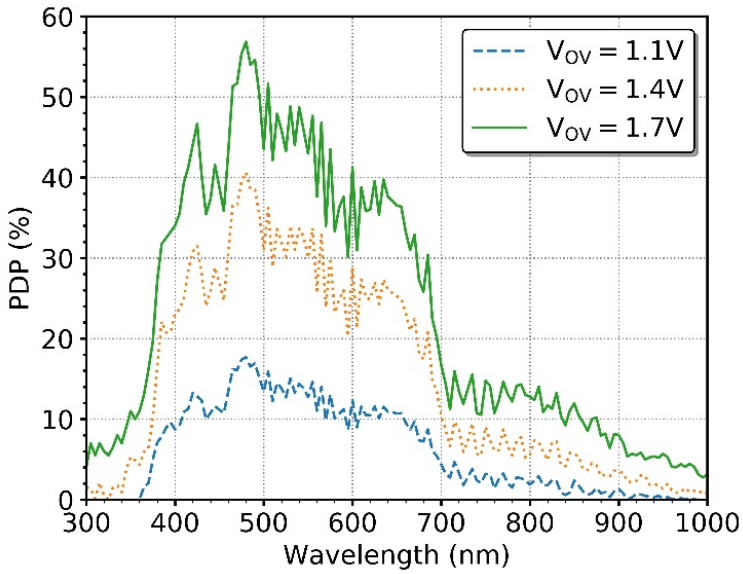

Figure 2.15 Spectral dependence of the PDP of a single SPAD at 1.1 V, 1.4 V, and 1.7 V of overvoltage with a maximum relative error of 0.5%. The PDP shows interference patterns caused by the passivation layers [140].

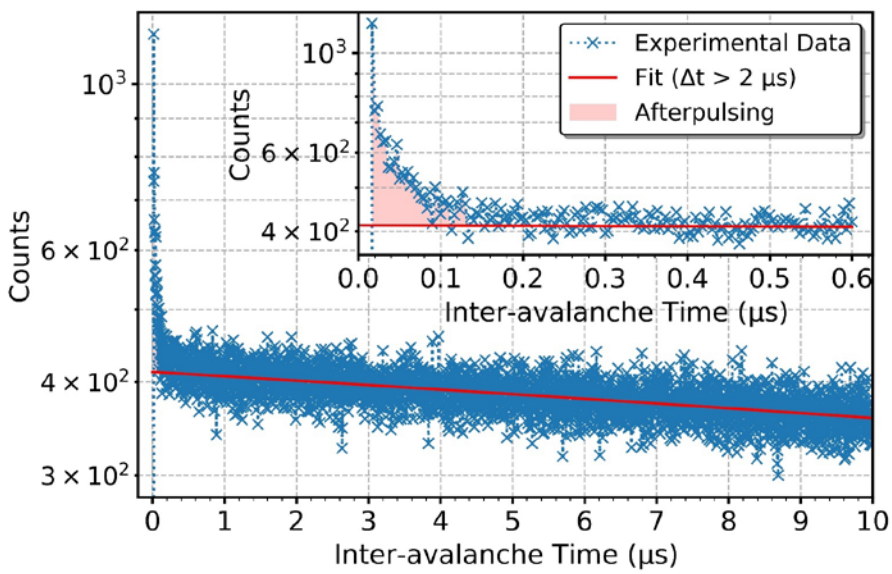

Figure 2.16 The inter-avalanche time histogram measured from a SPAD in the dark. The afterpulsing phenomenon causes counts over normal exponential response due to the Poisson statistics [193].

2.2.2.3 Timing Circuit

Since the pixel array only integrates quenching and recharge circuits with basic readout electronics, the timing and processing electronics required to perform the TCSPC technique were implemented in a Z-7020.

The use of Z-7020 is preferable over a conventional FPGA, because it introduces great flexibility brought by connecting a software platform directly with an FPGA. This solution enables the construction of an independent system with high flexibility by reprogramming either software or hardware.

As discussed earlier in section 2.1.2.2, the basis of a TDC-based TCSPC is to locate the input timing signal within the reference clock period and represent that location with a digital value. The resolution and accuracy of the TDC depend on the architecture, the clock speed used, and the device performance.

TDC ARCHITECTURE

The TDC architecture selection criteria were based on a critical review of the published work of TDC implementation in FPGA. There are different ways of building a TDC on an FPGA. The major architectures are based on TDL and Vernier delay lines [160, 161, 194–200]. Also, other structures have been invented to take advantage of the properties of the FPGA logic [163, 165, 166, 201]. Finally, the tapped delay method described in [161, 199] was selected to implement the TDC, due to the Z-7020 device has the same configurable logic blocks (CLBs) structure, the few resources required and its overall performance (achieving 17 ps and 15 ps resolution, respectively).

The overall architecture of the implemented TDC is shown in Figure 2.17. The TDC consists of a free-running counter as a coarse time measurement and a tapped delay line implemented in a carry chain as a fine time measurement within one coarse cycle. The measurement starts resetting the TDL and enabling the coarse counter. When an event occurs, the status of the delay line is captured, and the counter is stopped. The TDL output and the counter value are stored in the asynchronous FIFO before resetting them and start a new measurement. The stored TDL values are binary encoded by the encoder. The encoded TDL and the corresponding coarse value are combined by the historgammer that assigns an event

count to the corresponding memory position, building up the histogram of the event times. The control unit generates all the control signals for the TDC operation. The TDC implementation have two clock domains separated by the asynchronous FIFO. The control unit the TDL and coarse counter work at the counter clock (300 MHz), while the encoder and the rest of the blocks operate at a lower frequency (100MHz). With this configuration, the TDC achieves a throughput of 60 MS/s.

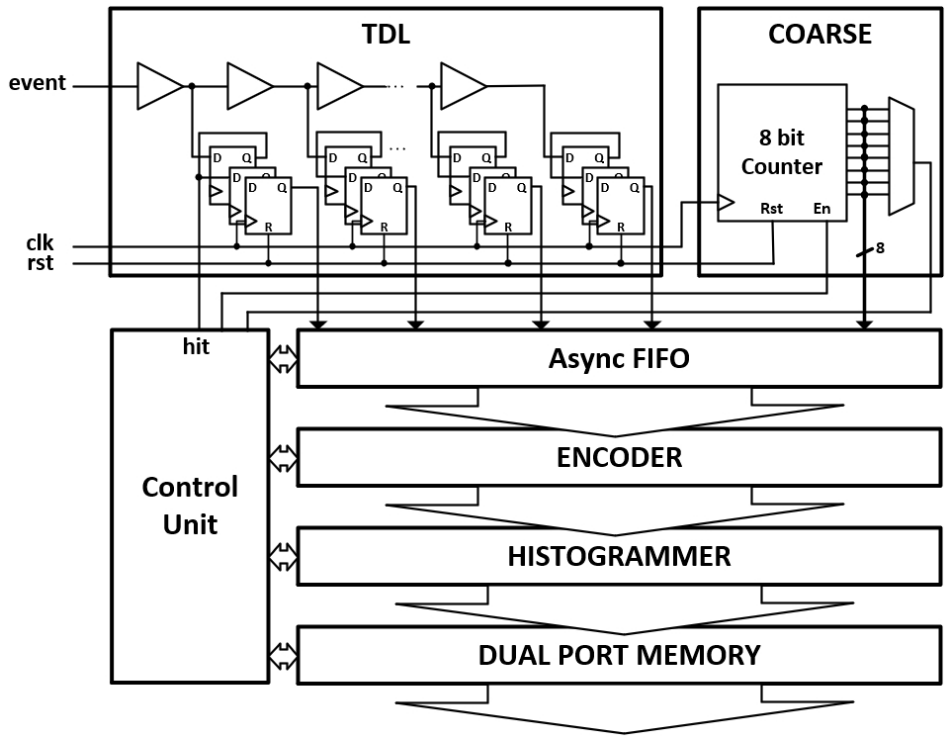

Figure 2.17 Architecture of the TDC.

Fine time measurement

The TDL of the TDC is implemented using the carry propagation logic, as described in [199]. This logic is intended to propagate carry signals in ripple-counters or adders, having dedicated routing resources, which relieves the need for manual constraining of the design. Additionally, each bit of the carry logic has a register very close to store the results of the operations. We use only one bit of

the carry logic to get more uniform TDL, and so avoid the variability introduced by the look-ahead logic implemented in the carry logic [202].

The carry lines propagate upwards within the FPGA structure, crossing multiple clock distribution regions, each 50 slices tall (Figure 2.18). The delay chain has to be within one of such regions to avoid significant clock skew effects breaking the delay chain. This sets the constraint for the clock of the TDC. The 50 elements must cover an entire clock cycle. The adequate clock was found to be of 300 MHz, using up to 49 of the carry elements, each one with a 68 ps of average delay.

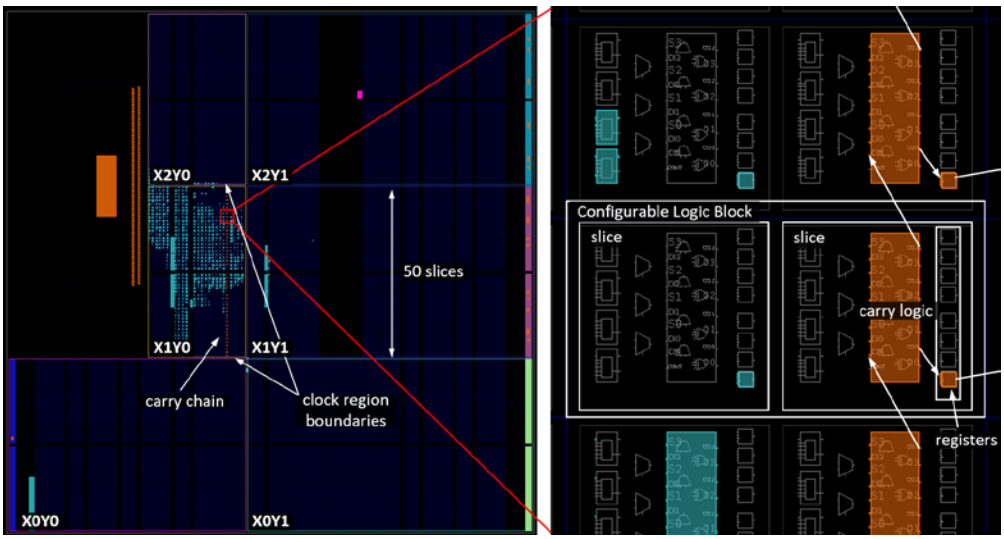

Figure 2.18 FPGA internal structure wit the implemented TDC with an insight of the carry propagation line with the registers. The different clock regions identified as XnYm, where each has a heigh of 50 slices (or configurable logic blocks tall).

The outputs of the delay chain are first stored in the registers present at each cell containing the carry logic to minimize propagation delay (insight of Figure 2.18), and then are subsequently registered through two additional registers to eliminate metastability. The resulting array of 49 bits is then stored in a small FIFO to synchronize it to the 100 MHz clock domain used for the encoding process.

Coarse time measurement

The coarse time measurement was implemented with an 8-bit counter, which keeps track of the cycles passed since the TDC is enabled, and stop once photon

is detected. If no event occurs in the TDC range, the counter generates an overflow signal that discards the measurement and resets the TDC.

The range of the TDC is configurable by means of a multiplexer that selects which bit of the counter is used as overflow. Therefore, the range of the TDC is given by $2^{overflow\ bit} \cdot T_{clk}$. At the clock frequency used (300 MHz), that means a range from 3.3 ns up to 426.67 ns. Thus, the complete measurement process will be faster since the duration of a measure can be adapted to the lifetime of the substance of interest, which typically ranges from ps to tens of ns.

Encoder

The result of the TDL is an array of 49-bit thermometer coded, ideally containing successive ones until where the hit signal propagated, and successive 0 from that point until the end. However, the clock skew between registers and the internal structure of the carry blocks used in the delay chain can cause alternating zeroes and ones, called bubbles, to be found near the edge of the changed propagation values [203] resulting in a pseudo-thermometer code.

In order to properly translate the TDL output into time, the pseudo-thermometer code has to be encoded to binary. The implemented encoder was described in [204] and consists of two stages. Figure 2.19 shows the architecture of the encoder together with an example for better understanding.

First, the pseudo-thermometer code is converted into a one-hot code, where only the last position to which the hit signal propagated remains high, and the rest is set low. This conversion is implemented by AND gates with 3 input inverted followed by flip-flops to store the conversion result. During the conversion of pseudo-thermometer code to one-hot encoding, up to 2-bit bubbles can be corrected through the AND operation. In the second step, the fat-tree encoder converts the one-hot word into the binary count of the number of bits changed in the TDL, with a length of *log2(N-Delays)* where N-Delays is the number of bits of the TDL. The resulting binary number represents the time inside a clock period where the event occurs.

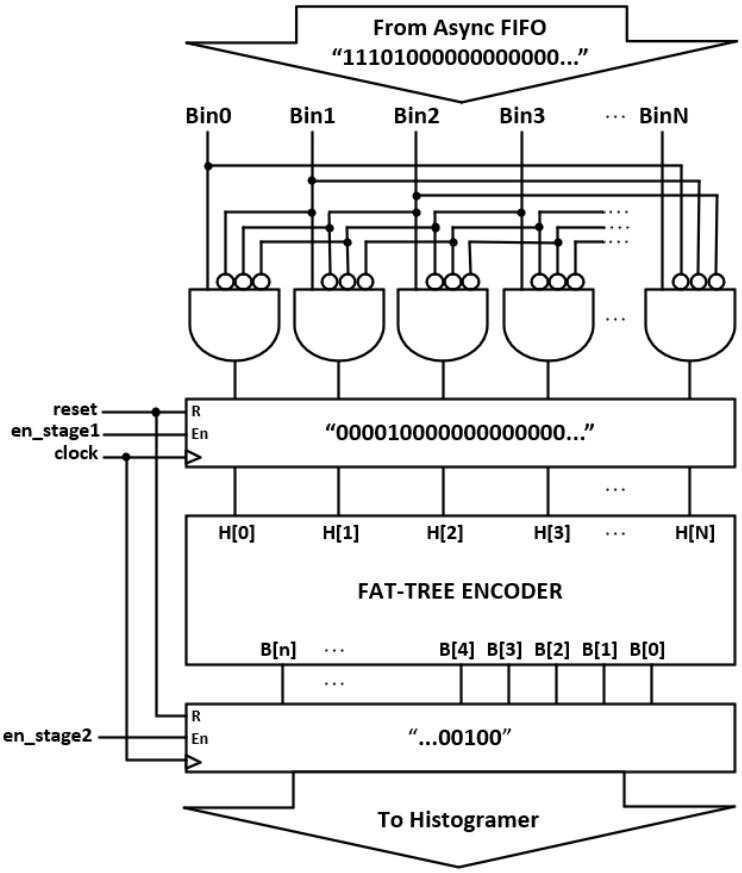

Figure 2.19 General flux diagram of the encoder operation with pipeline registers represented.

Histogrammer

In order to reconstruct the histogram of the measured signal, the whole range of the TDC (all the time bins) is mapped into internal memory. Each memory position corresponds to a time bin of the width of the fine delay element used (or LSB of our system).

After each event, the address (time bin number) is calculated by (2.6), and the value stored in that memory position is automatically increased by one, counting the number of times the bin came out and thus building the resulting histogram for the measure.

$$address = N_c \cdot N_{DELAYS} - N_d \tag{2.6}$$

Where Nc is the number of clock cycles returned by the coarse TDC counter, NDELAYS are the number of delay elements in the delay chain (49 in this case) and Nd is the binary encoded of the TDL (the number of bits turned).

The memory used is a block RAM of 13-bit deep and 32-bit wide, which is enough to accommodate the 6.272 time bins (Nc·NDELAYS) of the TDC and to establish enough repetitions to build the histogram of the measure.

TDC CHARACTERIZATION & CALIBRATION

Characterization

The whole range of the TDC has to be characterized by performing a density test. To do so, we took advantage of the dark noise of the SPAD sensor, which follows a Poissonian distribution described by, $P_{dc} \sim Pois(k) =\cdot \lambda^k e^{-\lambda}/k!$, where k is the number of events in the interval, and λ is the average number of events in the interval (given by $\lambda = DCR \cdot t$ where t is the time interval) [186]. From the equation, it can be inferred that the decay rate of the exponential function depends on the DCR of the SPAD. Therefore by maintaining a low count rate, it is possible to attain approximately a uniform distribution across the TDC range [205].

Since a SPAD with a low count rate is required, we made 500 million of measurements in order to obtain a large number of counts per bin to characterize the individual time each delay bin represents. Figure 2.20 shows the histogram of a dark noise measurement used to characterize the TDC. As can be seen, there is a high dispersion of counts per container due to the nonlinearities of the TDL. Figure 2.21 shows the calculated DNL for the implemented TDL.

According to the DNL, the TDL presents a variation smaller than one LSB (where 1 LSB is 68 ps), except for bin 25 and bin 26 that presents DNL of -1 LSB and +1 LSB, respectively. This is because the bin 25 has an effective time of 0 seconds and the next bin accumulates the counts of two bins. The rest of the bins (90%) exhibits a deviation below 0.5 LSB. Figure 2.22 shows the density function of the width of the TDL bins with an average width of 68 ± 21 ps.

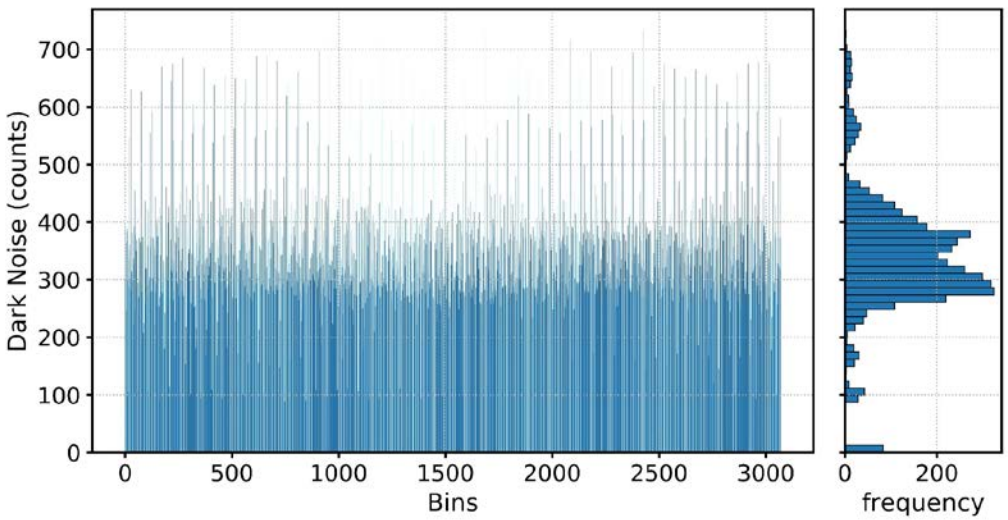

Figure 2.20 Data slice of dark counts measured over time with the implemented TDC (left) and the density of the counts per bin (right).

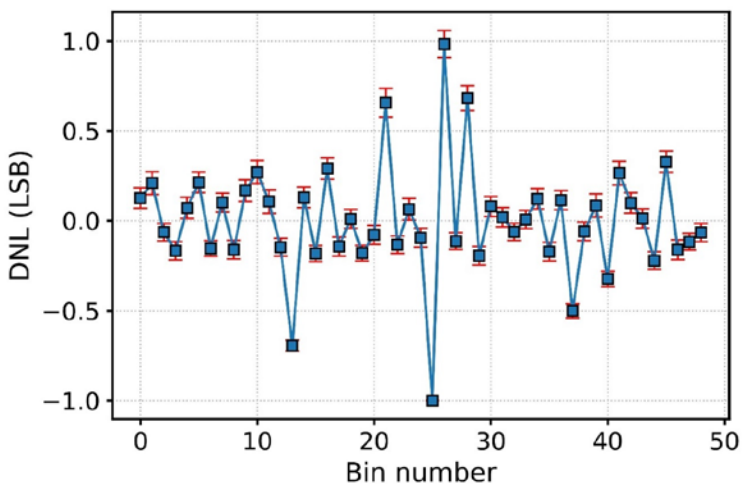

Figure 2.21 DNL of the TDL implemented in the TDC. The error bars were obtained from the multiple repetitions of the TDL through the whole range of the TDC.

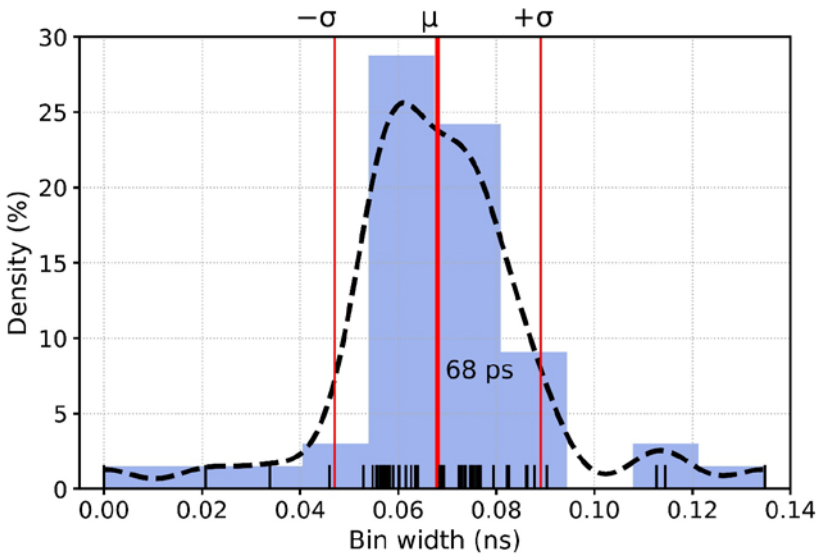

Figure 2.22 Bins density function of the TDC implemented.

The error accumulated in the measure (the INL) is presented in Figure 2.23. The error is always below 0.8 LSB, and it returns to 0 for the final bin, confirming that it covers a whole clock cycle as expected.

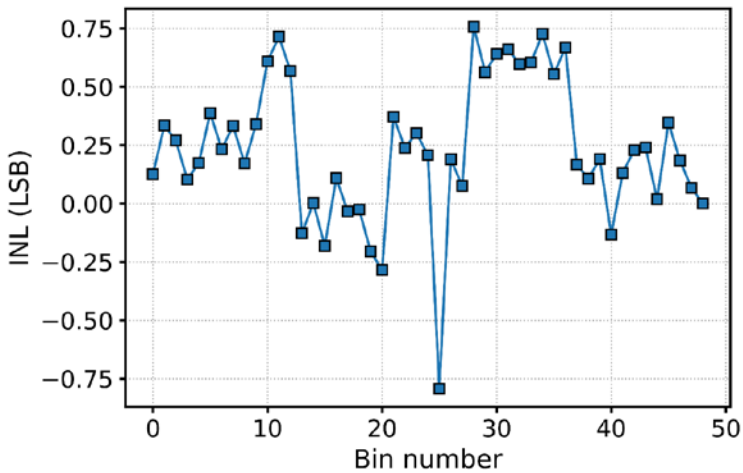

Figure 2.23 INL of the TDL of the implemented TDC.

Calibration

The bin-by-bin self-calibration (using the INL) has not been implemented in hardware. Instead, we use the DNL and the processing system of the Z-7020 to automatically perform a post-calibration procedure, applying the calibration to the resulting histogram once it has been generated.

The calibration process starts with a dark noise measurement. Then the DNL of each TDL element is automatically calculated and stored in a look-at-table in the processing system to be used as correction factors. The DNLs values are used to correct the aspect ratio of the bins. In particular, the DNL values are used as a width factor that adjusts the bin duration, while the DNL-1 adjusts the bin height. After each measurement, the correction factors are applied as the histogram is read from the internal memory before sending it to an external device for further processing or visualization.

Figure 2.24 shows a dark noise measurement after calibration, with a dramatic reduction of the bin counts dispersion compared with Figure 2.20.

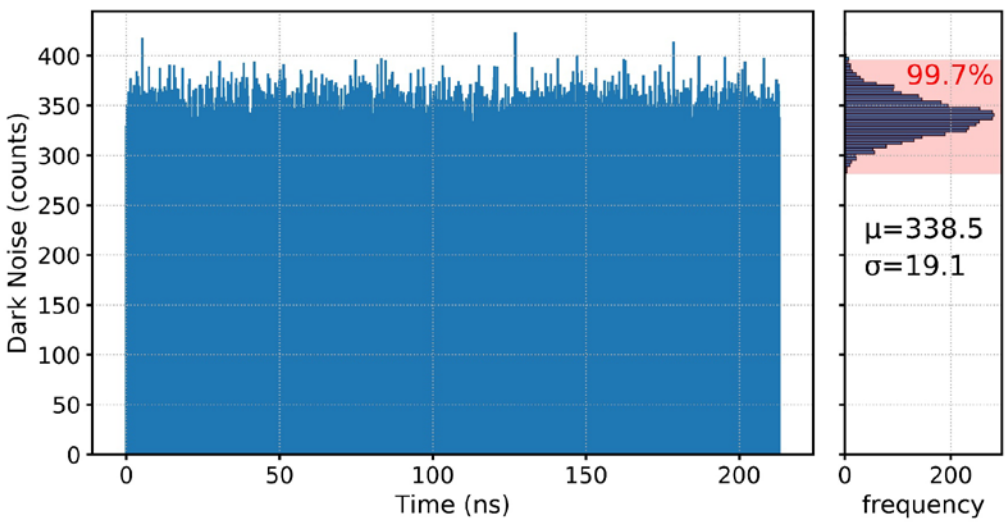

Figure 2.24 TCSPC of dark noise measurement after calibration (left) and the histogram showing the density of the counts per bin (right).

2.2.3 Pixel Array with Analog Histogramming on-Chip

2.2.3.1 Operation Overview

The circuit implements the TG technique to obtain the fluorescence decay curve and classifies the time-arrival of the photons in the analog domain on-chip. The entire operation of the system for one pixel and 7 repetitions is illustrated in Figure 2.25. Concurrently, a set of time windows is created with the *Start* signal (*bin[0]* to *bin[2]* in Figure 2.25). The pixel output inside *bin[i]* is resolved with the *binsel[i]* signal, which enables the injection of current into an internal capacitor. In this manner, analog signals proportional to the number of photons detected in each window (*out[0]* to *out [2]*) are observed simultaneously and used to build the histogram that describes the actual decay [54].

The size of the time windows is configurable. Therefore, the circuit can operate with very small lifetimes, such as those of organic dyes (some ns), as well as with relatively large decays, such as those of some types of quantum dots (tens of ns) [54].

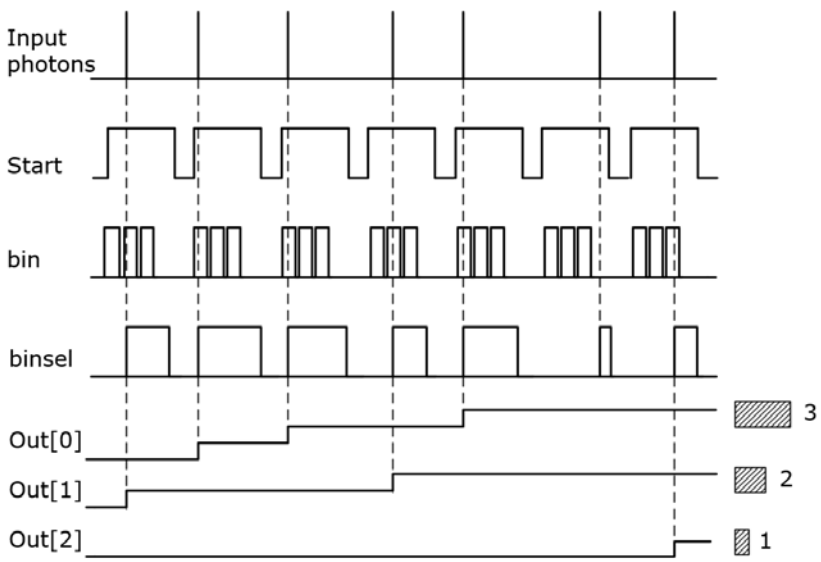

Figure 2.25 Timing diagram showing random input photons during 7 measuring periods, the *Start* signal, 3 time-windows (bins), the *binsel* signal after selecting in which window the photon dropped, and 3 outputs. The counts of all the windows (histogram) are shown on the right. For simplicity, only 3 bins and 3 outputs are shown. [54]

Changing the injection time on each capacitor, the current injected after photon detection is also configurable. However, there has to be a compromise between the accuracy required and the measuring time. Although only 3 bins are shown in Figure 2.25 for simplicity, we used 9-time bins for the circuit, which has been reported to be more than enough for mono-exponential decays [11, 54, 206, 207].

2.2.3.2 General Architecture

The overall architecture of the system is shown in Figure 2.26. A 1-D array of 5 pixels distributed linearly and spaced 125 µm has been implemented. Each pixel consists of a basic SPAD pixel (described in section 2.1.1) connected to an analog histogramming circuit. All the control signals and bias voltages are common to all the pixels and generated externally. Since the circuit does not include any ADC to read out the analog bins values, each bin output was connected to an analog buffer. To minimize I/O count, we used a 5:1 analog MUX per bin. Thus, one pixel was selected to measure all its bins simultaneously. The generation of the control signals can be generated internally (as described in section 2.2.2.1 but using the external INH signal as start signal) or externally [54].

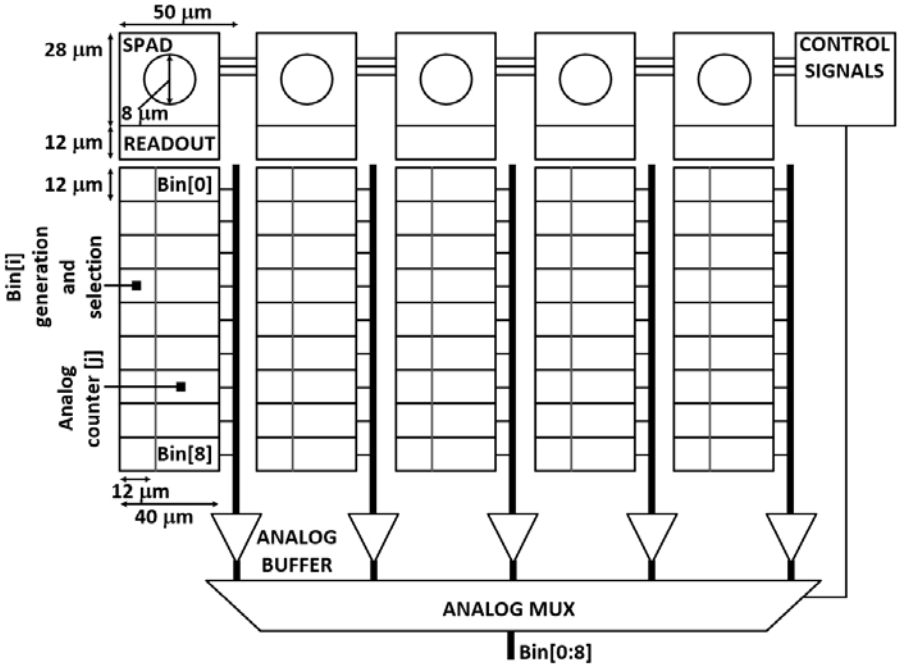

Figure 2.26 Architecture of the implemented 5-pixel circuit with dimensions [54].

2.2.3.3 Analog Histogramming Circuit Description

For clarity, the relevant signals of the circuit are shown in Figure 2.27 for three-time bins. Photon arrivals are classified in a set of time bins that are created from the triggering of the *Start* signal (Figure 2.28). First, the *Start* signal is an input of a current-starved inverter that produces a delayed inverted signal. The pMOS M1 and nMOS M2 (Figure 2.28) operate as current sources that limit the current available for the inverter formed by M3 and M4. M1 and M2 drain the same current [208]. *Vbias* fixes the bias of the current inverter and, thus, the delay. Then, the *Start* signal and its delayed inverted version are fed into an AND gate, producing a pulse that starts with the *Start* signal and has a duration that is fixed by the delay. This gives rise to *binpulse[0]*, the first pulse in which the analyzed time is divided. The other pulses are obtained in the same way, using *phi[i]* signals instead of *Start*. Thus, *binpulse[1]* is obtained from *phi[0]* and *phi[1]*, which is a delayed version of *phi[0]*, and so on [54].

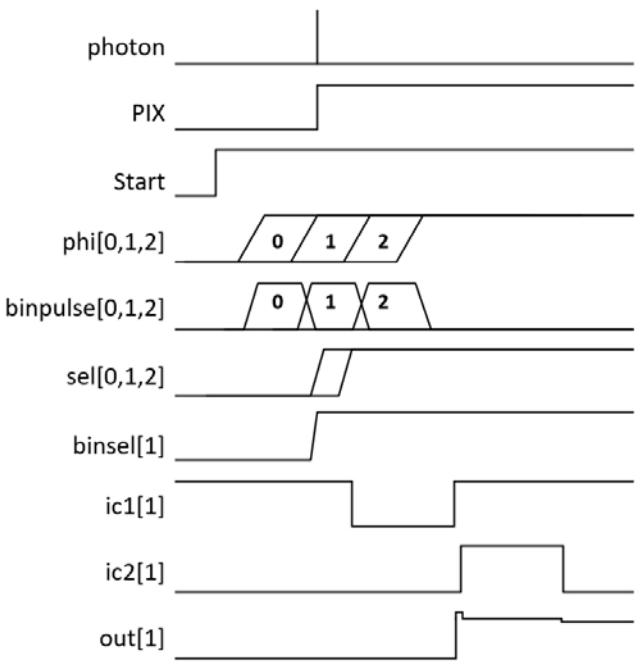

Figure 2.27 Sequence of signals when the *Start* signal is triggered and a photon is detected in the time *bin1* [54].

Each *binpulse[i]* signal and the output of the pixel circuit (*PIX*) are fed into a dynamic NAND gate. The operation of this gate is such that it is pre-charged by M5 to *VDD*, and discharged by M6 and M7 to *GND* only if the *PIX* rising signal edge is within the *binpulse[i]* time window. *Start* acts as the clock in this Pre-charge-Evaluation dynamic gate. This NAND gate provides a selection signal that, after being inverted, indicates that the photon has been detected, *sel[i]*. The output *PIX* is registered. Consequently, from the moment that the photon is detected, all *sel[i]* signals are active for the rest of the measuring period. If, for example, the photon is detected in *binpulse[1]*, like in Figure 2.27, the *sel* vector should be [*GND*, *VDD*, *VDD*]. Afterward, the *sel[i]* signal is fed together with *sel[i-1]* (or *GND* for $I = 0$) into an XOR gate that only activates the output, *binsel[i]*, in the transition from *GND* to *VDD* of the *sel* vector. In other words, if *sel[i-1] = GND* (before *i* the photon is not detected) and *sel[i] = VDD* (the photon was detected at

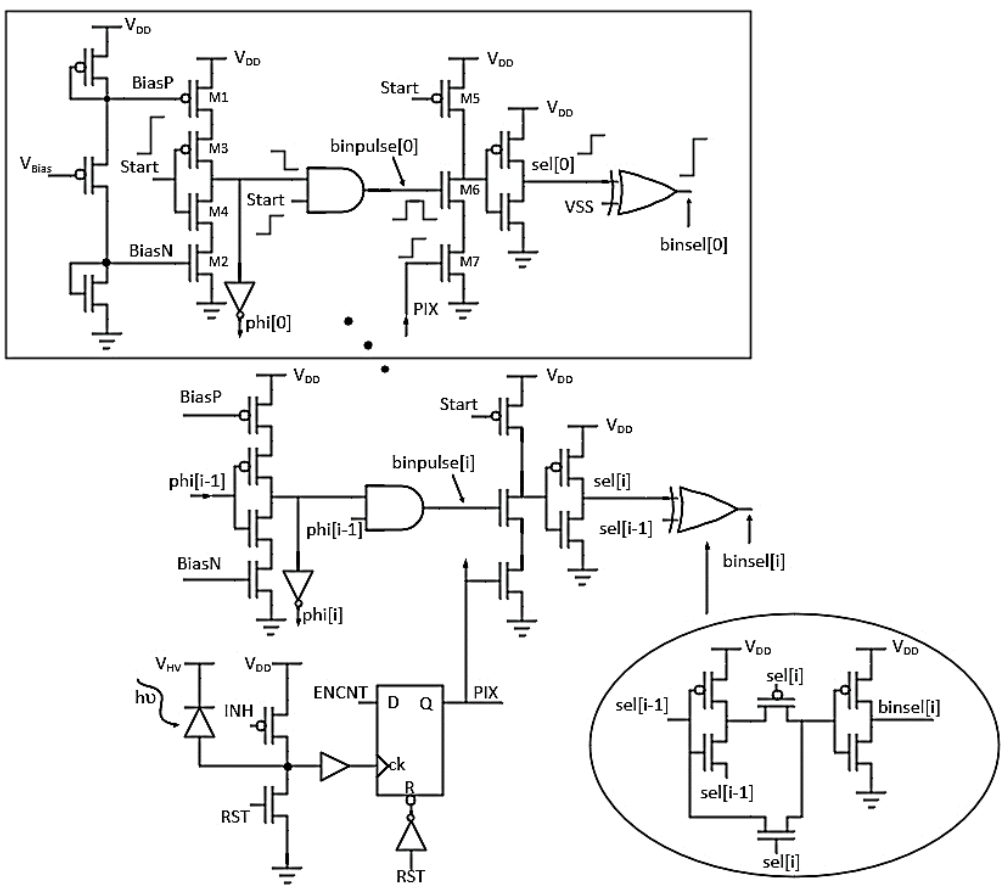

Figure 2.28 Schematic of the circuit for generating and selecting the bins [54].

bin *i*), then only *binsel[i] = VDD*. Thus, in the above example, only *binsel[1]* would be *VDD*. This circuit unequivocally identifies the time bin in which the photon has been detected. The *binsel[i]* signal decides which capacitor will be injected with a fixed amount of charge. Each time window has its own capacitor [54].

Figure 2.29 shows the analog counter circuit. The amount of charge injected is controlled by the width of the pulse in *ic1[i]*, which in turn is obtained from the AND of *binsel[i]* and its delayed version. When the transistor M10 opens, it sources current from *VDD* until it closes. The charge injected is stored in a parasitic capacitor formed by the drain capacitance of M10 and M11, and the source of M12. The transfer to the storage capacitor is controlled by *ic2[i]* [54].

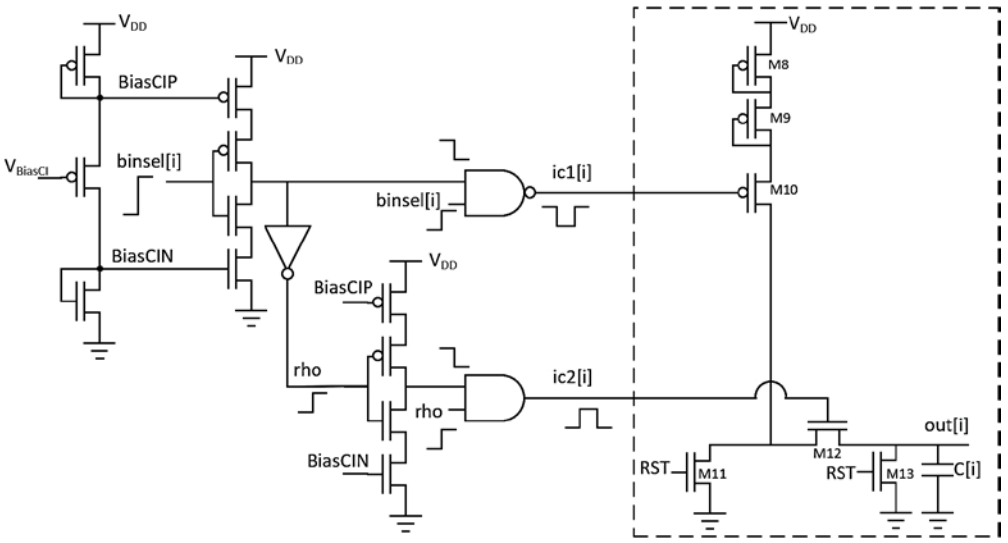

Figure 2.29 Schematic of the analog counter circuit [54].

The pulse widths of *ic1* and *ic2* are programmable with *VbiasCI*. In this way, the charge injected does not depend on the time the photon is detected during a time bin. By contrast, a fixed amount of charge is injected at any time after the arrival of the photon. The transistors M11 and M13, controlled by the *RST* signal, reset the analog counter [54].

2.2.3.4 Circuit Characterization

The chip was connected to an acquisition board developed in our laboratory, which included an ADC (ADS1258IRTCTG4, Texas Instruments, USA) with a 24-bit resolution and a maximum conversion rate of 125 kS/s. A Z-7020 development board was used to collect the measurements and manage the chip. The bias voltages *VBias* and *VBiasCI* were applied directly with external bias sources connected to a computer and programmed with a Python script.

Experimental results of bin widths as a function of *Vbias* are shown in Figure 2.30 for 10 chips. Variations were observed among the chips due to fabrication mismatches. While the dispersion was below 10% when *Vbias* < 750 mV, it could double for larger *Vbias* values, therefore, for application in time-resolved fluorescence measurements, all chips must be accurately characterized and calibrated. According to Figure 2.30, the minimum achievable bin width is 168 ps for *Vbias* = 0 V and 4.9 ns for *Vbias* = 950 mV. Consequently, fluorescence decays from 1.5 ns to up to 44.1 ns can be detected with 9 bins, enabling the decay times of organic and inorganic dyes to be characterized [54].

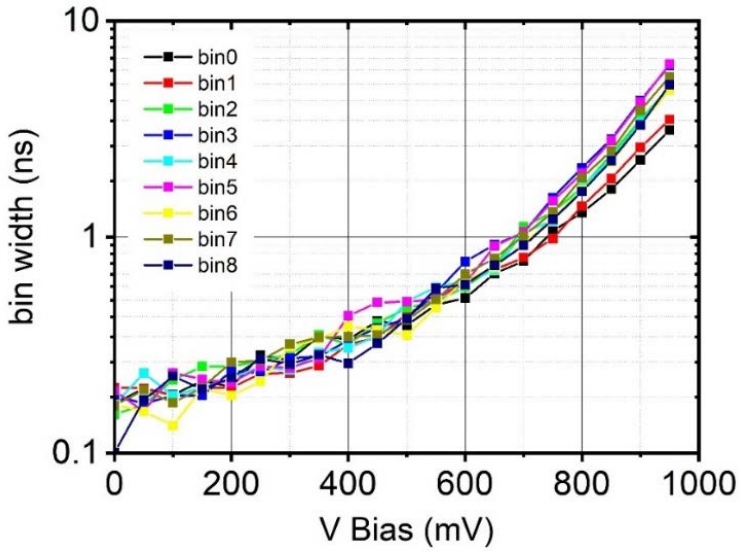

Figure 2.30 Bin widths averaged for 10 chips as a function of *Vbias*. For Vbias ranging from 150 to 750 mV, the maximum deviation of the bin width was always below 10% [54].

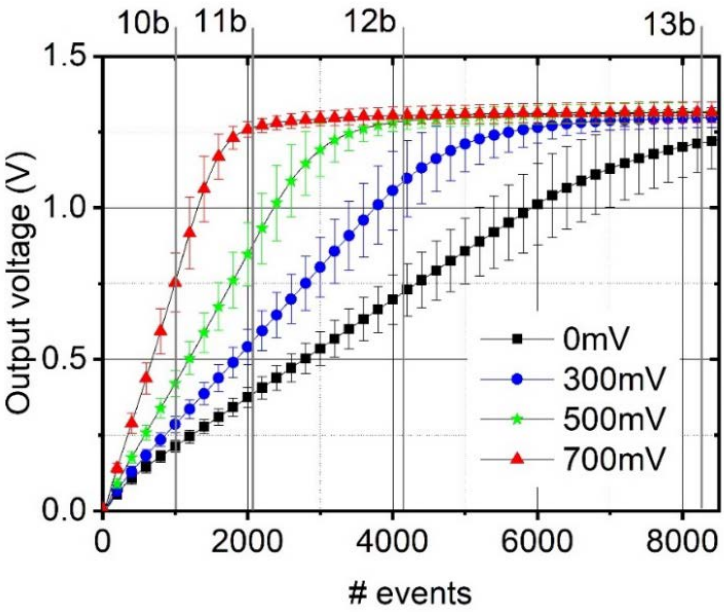

Figure 2.31 Measured output voltage as a function of the number of SPAD events for different VbiasCI values. The error bars show bin-to-bin deviations for 10 different chips [54].

In Figure 2.31, we plotted the output voltage as a function of the number of detected events for different *VbiasCI* values, with *Vbias* fixed at 600 mV. The error bars indicate bin-to-bin variations for 10 different chips. The output was almost linear with the number of pulses detected until saturation. For the capacitance used (C = 160 fF) and the sizes of M1 and M2 in Figure 2.28 (440 nm/180 nm), the injected charges corresponded to 0.76 mV/event for *VbiasCI* = 700 mV, which gave an accuracy of 10 b (1,024 events) for an output voltage of 800 mV. The minimum attainable injection was of 0.16 mV/event for *VbiasCI* = 0 V, producing an accuracy of 13 b for an output voltage of 1.3 V, which is its maximum value due to the analog buffer at the circuit output [54].

The experimental results of bin decay show that the storage bin capacitors had current leakages that discharge the capacitor at a constant rate. These discharge rates were independent of the *VbiasCI* and vary from bin-to-bin due to fabrication mismatches. Figure 2.32 shows the dispersion of bin decay for the five circuits in one chip and per bins (with the outliers in red). The measurements were conducted by forcing 1000 consecutive events in each bin separately and measuring the decomposition rate in an oscilloscope. The time between the conduced events was

100 ns, giving a total measurement time of 100 µs. Variations from −30.4 ± 0.3 mV/ms to −253.3 ± 4.1 mV/ms were observed between the bins of the same circuit (Figure 2.32, circuit 2). In the worst case, where the circuit operates with the maximum bin widths (9 x 4.9 ns) and the afterpulsing is completely avoided (SPAD toff = 200 ns), each measurement takes 245 ns. For the worst bin, it supposes a voltage decay of 62 µV/no-event. Therefore, the variances in the decomposition rate distorted the measurement when long measurement periods are used at low count rates, exacerbating the detection limit in time-resolved fluorescence applications.

The charge is injected after the arrival of the photon. Then, the slower case occurs when the photon is captured in the last moment of the last bin. Consequently, the maximum repetition rate corresponds to 9 times the minimum bin width plus the charge injection time. According to our results, this was roughly 1.68 ns (> 600 Mevents/s) in each pixel [54].

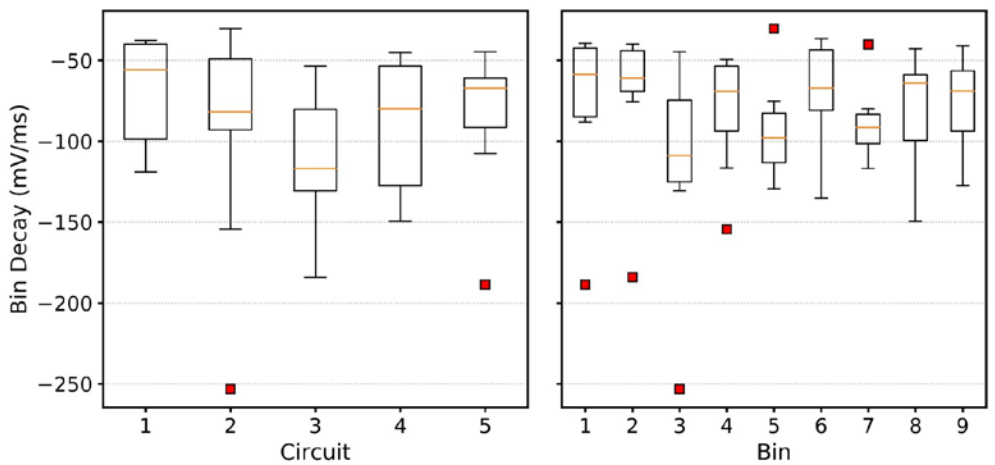

Figure 2.32 Box plots showing the dispersion of the bin decay for the 5 circuits of one chip (left) and by bins of all the circuits (right). The outliers are represented as red squares.

2.3 Summary

In this chapter, two SPAD-based circuits aimed at fluorescence lifetime spectroscopy were presented. The first circuit proposes a primary 1-D array of 10 SPAD pixels with output data serialization capability, controlling the measurement and

processing the data off-chip. In contrast, the second circuit presents a novel and straightforward solution for detecting time-resolved fluorescence, implementing an analog reconstruction of the decay histogram on-chip. The histogramming circuit was integrated in-pixel of a 1-D array of 5 SPAD. Both circuits were integrated into the same sensor chip. Moreover, the layout geometry of both circuits was designed taking into account the packaging and the final device implementation, aimed to perform off-chip contact sensing fluorescence lifetime measurements using a microfluidic cartridge with up to three 100 µm microchannels.

In particular, the design and characterization of the integrated SPAD pixel detector and the analog histogramming circuit on-chip were analyzed. The SPAD pixel used in both implemented circuits presents a good PDP (over 20% at 1.4 V overvoltage) in the visible range, where the majority of fluorophores used in fluorescence-based techniques has its emission peak. However, the DCR of the SPAD detector implemented is quite high, which is a significant limitation operating at low light level conditions, meaning low levels of sample concentration in fluorescence analysis. Table 2.1 shows the main characteristics of the SPAD pixel designed.

Table 2.1 SPAD performance summary.

Specifications @ 25°C and 1.4 V of overvoltage	**Value**	**Units**
Dark count rate (DCR)	$7{\cdot}10^3$	cps
Photodetection probability (PDP)		
400 nm	23	
480 nm	40 (max)	%
600 nm	25	
700 nm	10	
Afterpulsing probability	<0.2	%
Timing jitter*	<80	ps
Active area diameter of each SPAD	8	µm
SPAD bias voltage	13.0	V

*Estimated from similar SPAD found in the literature [192].

For the pixel array with external timing circuit, TDC-based TCSPC technique was implemented in a Z-7020. The implemented TDC is a pure TDL with 49 delay elements with an LSB of 68 ps, and a total measurement range of 426.67 ns, which

is operated at 300MHz. The maximum DNL is 1 LSB. The TDC is entirely configurable and easily scalable. The low resources used by the TDC (Table 2.2), allow to include multiple channels for example or largely increase the maximum measurement range. Moreover, self-calibration structures such as [160, 161, 209, 210] are not required. Instead, the bin-by-bin calibration procedure is implemented in the processing system of the Z-7020 device, that controls all the processes, performing the density test and extracting the calibration factors that later will be applied to the resulting histogram.

Table 2.2 Z-7020 programmable logic resource utilization.

Resource	Used	Total	Percentage used
LUT	1510	53200	2.84
LUT-RAM	92	17400	0.56
FF	1861	106400	1.75
BRAM	75	140	5.35

However, further improvements can be carried on the design to improve its general performance. In particular, ways to reduce the non-linearity and improve the TDC resolution, which is generally limited by the ultra-wide bins. A straight forward solution would be making multiple measurements of the same hit within a single delay chain structure such in [209], to sub-divide the ultra-wide bins in each raw measurement. Alternatively, a more drastic solution would be to migrate to a more sophisticated TDC architecture, such as Vernier TDL [198] or based on high precision oscillators [166].

The analog histogramming circuit consists of an analog pixel that can classify photon arrival times on-chip for the whole decay curve. The circuit divides the period being investigated into 9-time windows and simultaneously measures the output that corresponds to the 9-time bins. Moreover, the time windows can be programmed to fit the lifetimes down to 1.5 ns. This produces a compact and efficient circuit, where the pixel implemented has a maximum resolution of 13 b. The 9 bins are implemented in an area of 150 µm x 50 µm in a 180 nm HV-CMOS process. The total area used by the electronic circuit is 76% of the 150 µm x 50 µm area, demonstrating the area-efficient design of the circuit. Table 2.3 presents the main characteristics of the histogramming circuit. Table 2.4 compares the performance of the histogramming circuit presented with those of the other chips reported in the literature. The circuit presented is currently the only one that

performs an analog evaluation of the whole histogram on-chip. For a rough comparison with digital histogramming circuits, we estimated the area of the circuits presented in [183] and [184] from the pictures they showed. The comparison shows a better performance of analog histogramming circuits in terms of area savings [54].

Table 2.3 Histogramming circuit performance summary [54].

Specifications @ 25°C and 1.4 V of overvoltage	**Value**	**Units**
Area of 1 pixel	150 x 50	μm^2
Percentage of the pixel area covered by the histogramming circuit area	76	%
Measurement range (Vbias 0/950mV)	1.5-44	ns
Minimum resolution per photon (VbiasCI = 0V)	0.16	mV
Maximum resolution per photon (VbiasCI = 700mV)	0.76	mV
Maximum bit resolution	13	b
Maximum rate	$6 \cdot 10^8$	cps
Power consumption per pixel (Vbias = 900mV, VbiasCI = 700mV):		
Bin with event	20	µW
Bin w/o event	10	µW
Pixel (9 bins) with event detected	100	µW

Table 2.4 Comparison of recently developed SPAD sensors for fluorescence lifetime measurement [54].

Ref	[178]	[51]	[58]	[185]	[188]	[182]	[183]	[184]	This work
CMOS process	0.35 µm	0.35 µm	0.35 µm	0.35 µm	0.35 µm	0.35 µm	130 nm	130 nm	0.18 µm
Year published	2008	2009	2008	2013	2015	2009	2015	2017	2018
Size (pixels)	64 x 64	2 0x 20	16 x 4	32 x 32	160 x 120	64 x 1	32 x 32	1024 x 4	5 x 1
Counter on-chip	Digital	Digital	Digital	Analog	Analog & digital	Digital	Digital	Digital	Analog
Circuit considerations	Global TDC on-chip		Global TDC on-chip				-		
Analysis	TG TCSPC FPGA control	TG FPGA control	TG FGPA control	TG External control	TG External control	TG External control	TCSPC Internal control	TCSPC Internal control	TG Internal control
Resolution	n.a.	17 b	9 b	8 b	6.5 b	8 b	16 b	10 b	13 b
Histogramming	Off-chip	Off-chip	Off-chip	Off-chip	Off-chip	Off-chip External windows	On-chip	On-chip	On-chip
Number of histograms/chip	-	-	-	-	-	-	1	32	5
Area per histogram	-	-	-	-	-	-	*1,000k (μm^2)	*700k (μm^2)	5.4k (μm^2)
Number of bins in histogram	-	-	-	-	-	4	33	32	9
Range of histogram	-	-	-	-	-	-	18.85 ns	204 ns	1.5 – 44 ns
Maximum rate	-	-	-	-	-	-	1.7 Gphotons/s	16.5 Gphotons/s	3 Gphotons/s

*Estimated from pictures, not reported.

Chapter 3

Microfluidic Chip

Molecular diagnostic assays generally consist of methods and techniques that detect biomarkers found in the DNA, RNA, or gene products of an organism [211–213]. In fluorescence-based bioassays, the sample preparation usually involves the labeling of the biomarkers with fluorescence dyes [214, 215]. Besides, in point-of-care testing applications, the use of a low volume of reagents to prepare the sample is preferred, as well as a straightforward method to handle and place it over the detection area [74, 216]. With microfluidic technology, it is possible to operate on micro- and nano-scale liquids and particles. Microfluidic systems have been extensively researched and developed during the last two decades owing to the inherent advantages, such as low sample and reagent volume, high capability of integration, parallel analysis, and rapid reaction from small feature sizes [217]. These features have resulted in a wide range of promising laboratory and biotechnological applications such as pathogen detection systems to point-of-care diagnostic devices [216], cell manipulation [218], cell culture [219], cell detection and diagnosis [220], and high-throughput screening [221].

Microfluidic devices are commonly fabricated with polymer materials such as polymethyl methacrylate (PMMA), cyclic-olefin-copolymer (COC) and polydimethylsiloxane (PDMS) due to the simple and low-cost fabrication processes (soft lithography, molding, embossing, and printing) [222]. Among the polymers, PDMS is the most popular material in microfluidic chips for fluorescence bioassays because it is optically transparent, biocompatible, and presents low

autofluorescence [223]. Moreover, PDMS can bond to silicon, glass, and other thermoplastic materials constructing hybrid devices, as well as PDMS itself [224].

This chapter presents a removable microfluidic cartridge to perform off-chip contact sensing by placing the sample straightforward over the SPAD sensor arrays described in Chapter 2. The design and fabrication procedure of microfluidic channels in PDMS bonded with glass are outlined in the following sections. Section 3.1 describes the materials and methods to manufacture the microchannels cartridge in PDMS. Section 3.2 discusses the microchannel design according to the requirements of the integration of the final device. Finally, Section 3.3 presents and characterize the resulting cartridge and the intermediate structures generated during the fabrication process.

3.1 Materials and Methods

The microfluidic cartridge was fabricated in PDMS by soft-lithography method based on rapid prototyping and replica molding [225], using a SU-8 mold fabricated by photolithography [226]. Figure 3.1 shows and schema of the complete process. The fabrication process has been carried out in the facilities of the Physics Faculty of the University of Barcelona, which includes 200 m^2 ISO 7 (10000-Class) Clean room with a 50 m^2 ISO 6 (1000-Class) lithography area.

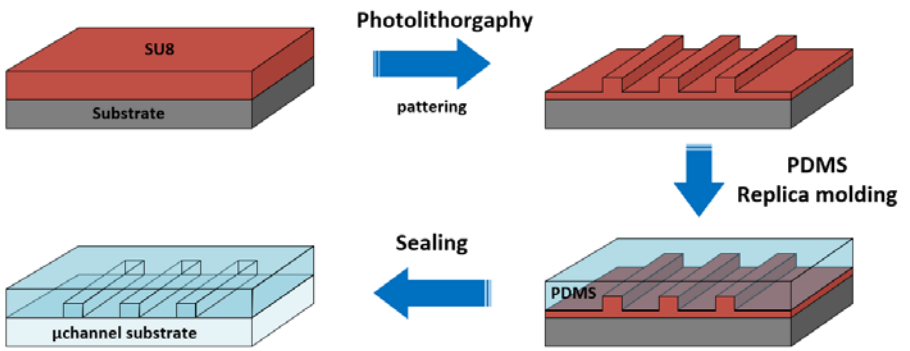

Figure 3.1 Process overview of the PDMS microchannel fabrication by the soft-lithography method.

3.1.1 Materials and Equipment

The materials required to manufacture the microfluidic chip by replica molding technique are:

- SU-8 100 Negative Tone Photoresists (Microchem Company, US)
- Developer mr-Dev 600 (Micro Resist Technologies GmbH, Germany)
- Microscope slide (SLIG-010-050, Labbox LabWare S.L., Spain)
- PDMS (Sylgard® 184 Silicone Elastomer Kit, Dow Corning, US)
- 150 µm thick coverslip (12460S, Thermo Fisher Scientific Inc., US)
- Acetone
- Isopropanol

The equipment used to manufacture the microfluidic chip are:

- Spinner and Hot plate (Delta 6RC, Suss MicroTec AG, Germany)
- Plasma Cleaner (PDC-002, Harrick Plasma, US)
- Digital Ultrasonic Cleaner (CD-4820, Axtor-Lovango, Spain)
- Mask Aligner and UV Exposure (SET Micro Controle MG1410, Suss MicroTec AG, Germany)
- Desiccator with a vacuum pump
- Electronic precision scale (Vicon, Acculab)
- Biopsy punch
- N_2 gun
- Petri dishes
- Plastic cut
- Cutter knife
- Spatula

Free-Hand 10 (CAD software from Macromedia®) was used to design the microchannels structures mask.

3.1.2 SU-8 Mold by Photolithography

The SU-8 100 (Microchem Company, Newton (MA), US) [227] was used to perform the mold of the microchannels structures. SU-8 100 series is intended for thick, thermally and chemically stable structure in micromachining and other

microelectronic applications. The substrate used is a microscope glass slide (SLIG-010-050, Labbox LabWare S.L., Barcelona, Spain). The CAD design of the microfluidic channels structures was printed on flexible slide by a commercial printer with 10 µm of resolution at LEICROM S.L. This slide was used as a mask to transfer the structure of the channels to the SU-8.

The SU-8 mold by the photolithography process, shown in Figure 3.2, consists of six steps: substrate pretreatment, spin coat, soft bake, expose, post-expose bake, develop, and an optional hard-bake. The parameters of each step of the process, spin speed, bake times, and exposure time, depends on the desired thickness. Table 3.1 shows the parameters used to obtain SU-8 structures of 100 µm thickness.

First of all, the substrate must be prepared before receiving the SU-8 photoresist to ensure good bonding between them. The substrate is cleaned from organics residues by an oxygen plasma ashing for 3 min at 30 W. Then, the substrate is sonicated in both acetone and isopropanol alcohol baths for 10 minutes per each solvent. Finally, the substrate is dried with an N_2 gun and heated at 200ºC for 20 min on a hotplate to remove all moisture on the substrate surface.

Once the substrate is ready to receive the SU-8, 1 ml of SU-8 is deposited in the middle of the substrate per each 25 mm of diameter. The SU-8 is spread over the substrate surface using a two-step spin process. The thickness of the SU-8 photoresist layer depends on the rotation speed, the acceleration, and the SU-8 photoresist viscosity [228]. To obtain a thickness of 100 µm, first a spread cycle in which the substrate is spun at 500 rpm for 10 seconds (with an acceleration of 100 rpm/s) is performed, followed by a spin cycle that increases the speed to 3000 rpm (with an acceleration of 300 rpm/s), holding it for 30 seconds.

After the spin deposition of the resist layer, the SU-8 is soft-baked for the densification of the polymer and solvent evaporation using a hotplate. Baking with a controlled temperature ramp and slow cooling down reduces the stress on the SU-8 structure and the adhesion problems caused by the different thermal expansion rates of the SU-8 and the substrate [229]. First, the temperature is increased from room temperature to 65 ° C at 5 ºC/min and held for 10 min at 65 ºC. Then, the temperature is increased to 95 ° C (at 2 ºC/min rate) for 30 min. The hotplate is switched- off, and the SU-8 is allowed to cool down to room temperature (on the hotplate) before exposure to UV light.

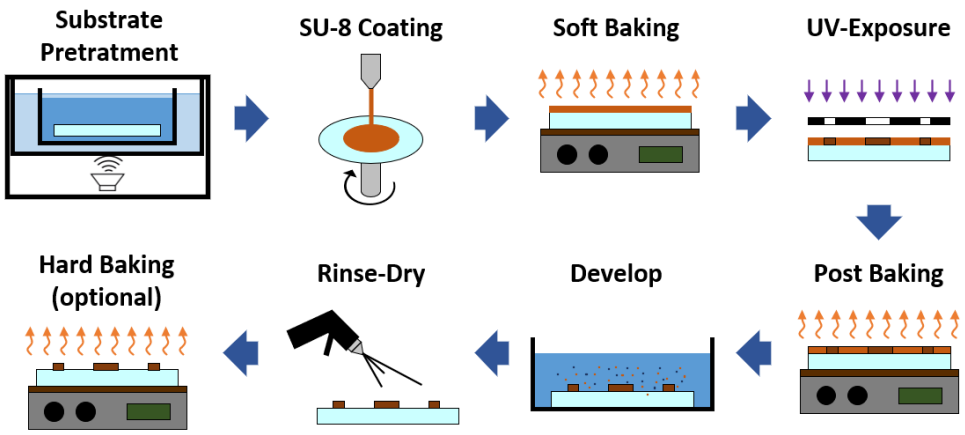

Figure 3.2 SU-8 mold fabrication process.

Table 3.1 SU-8 processing parameters

Parameter		Value	Unit
Target Thickness		100	µm
Spin Profile			
Spread Cycle	speed	500	rpm
	acceleration	100	rpm/s
	time	10	s
Spin Cycle	speed	3000	rpm
	acceleration	300	rpm/s
	time	30	s
Soft Bake			
from 25 ºC to 65ºC	rate	5	ºC/min
	hold time	10	min
from 65 ºC to 95ºC	rate	2	ºC/min
	hold time	30	min
UV-Exposure Time		12	s
Post Bake			
from 25 ºC to 65ºC	rate	5	ºC/min
	hold time	1	min
from 65 ºC to 95ºC	rate	2	ºC/min
	hold time	10	min
Development Time		4-7	min
Hard Bake Time at 150ºC		-	hour

The exposure to UV light initiates the cross-linkage by the activation of the photoactive component in the exposed areas of the photoresist. This activation changes the local properties of the resin which, after post-exposure baking, will

become hard. The exposure time depends on the SU-8 thickness and the power of the UV lamp. In our case, it is 12 seconds.

The aim of the post-exposure bake is to energize the reaction initiated by the UV exposure. As in the soft-bake, the mechanical stress inside SU8 is the most problematic point. Therefore, the same heating and cooling down profiles of the soft-bake are applied to reduce the stress, but changing the hold times to 1 min and 10 min for 65 ºC and 95 ºC respectively.

Finally, the microchannel structures are revealed on the substrate by diluting the non-linked SU-8 with the Developer mr-Dev 600 (Micro Resist Technologies GmbH, Berlin, Germany). The development is performed maintaining a good agitation (e.g., in an ultrasonic bath). The developing times depend on the thickness of the SU8 layer, 5-7 min for a 100 µm thickness. The development ends when no white film appears while rinsing the substrate with isopropanol.

3.1.3 PDMS Soft-Lithography

The Sylgard® 184 Silicone Elastomer Kit (Dow Corning, Midland (MI), US) [230] was used to perform PDMS replication and to obtain the microfluidic chip. PDMS lithography replication, called soft-lithography process, is divided into eigth main steps.

1. Preparation of the mold (optional but quite recommended)
2. Scaling and mixing of the PDMS and the curing agent
3. Degassing to remove bubbles
4. PDMS pouring on the mold
5. PDMS curing (by baking optional)
6. PDMS peeling off the mold
7. PDMS cutting and piercing
8. PDMS bonding to a substrate

Before using the SU-8 mold for the first time, it must be made hydrophobic. If the substrate of the mold is quite hydrophilic, the PDMS will have good affinity to it, strong enough to make the peeling impossible [231]. There are several ways to make the substrate (silicon or glass) hydrophobic, e.g., salinization [232]. In our case, the substrate of the mold is glass, which is not hydrophilic enough to present

this inconvenient, then this step can be skipped. Nevertheless, the mold must always be cleaned before using it, with an N_2 gun to remove dust and particles from the surface.

The cartridge structure was obtained by mixing the PDMS base and the curing agent at a 10:1 ratio (weight/weight). The mix was degassed before pouring into a Petri dish with the microchannel mold inside. The poured volume was controlled to obtain the desired thickness of the PDMS cartridge. If bubbles appear during the pouring, the PDMS was degassed again.

Once the PDMS and the curing agent are mixed, the cross-linkage has begun, but it will take more than 24 hours to get a solid enough to be manipulated. To speed up the curing process, the mold and PDMS can be baked. The temperature and the baking time do not influence the chemical properties of the PDMS but influence the mechanical properties [233]. The more cured, the less soft and sticky and more manageable the PDMS will be. The time and temperature of the baking changes according to the tool used and the mold container. In this work, two curing strategies have been carried out, both with the same results. The first one was to cure the PDMS at room temperature during the first 24 hours. After this time, since the PDMS was still sticky it was baked at 90 ° C for 10 minutes on a hot plate. The second strategy was to bake the PDMS directly at 90 ° C on a hot plate for 90 minutes, reducing the cure time considerably. In both cases, the mold and the PDMS have cooled down at room temperature during 30 min approx.

Next, the cured PDMS (with one or more devices) is cut around the substrate and peeled off. Then each device is cut to its final size. Special attention must be given while cutting the long side of the microchannel. The cut must be done vertically over the guide, to ensure that the first microchannel is at most 300µm from the edge of the chip. During this step, the inlets and outlets holes for each microchannel are made using a biopsy punch.

The resultant PDMS devices are sealed irreversibly with a glass coverslip (12460S from Thermo Fisher Scientific) of 150 µm thickness and 24 mm × 60 mm shape, by exposing them to an air plasma treatment at 30 W for 60 s. The union of both parts is critical since there is just one attempt, and the edge of the coverslip must be coincident with the PDMS edge where the microchannels are located.

3.2 Microfluidic Design

3.2.1 Requirements

The design of the microfluidic chip was oriented to meet the following requirements.

- It does not require an alignment procedure between the microchannels and sensor array.
- It is aimed to avoid the use of focusing systems.
- The width of the microfluidic chip must be at most the width of the packaged sensor chip.
- Low sample volume.
- Compatible with micropumps.
- Easy to handle.

3.2.2 Design Conception

The microfluidic chip was specifically conceived for the pixel array with external timing circuit. The structure and geometry of the microfluidic channels were determined by the geometry of the SPAD sensor chip, the sensor packaging, and the selected substrate to seal the microfluidic channels. Figure 3.3 shows a diagram of the characteristics of the packaged sensor geometry, and the different distances are listed in Table 3.2.

To ensure a homogeneous exposure of the active area of the sensor to the light emitted by the sample, the width of the microchannel must be twice the pitch of pixels. As shown in Figure 3.4, doubling the minimum width ensures that one pixel will have at least 25 μm of the microchannel (i.e., sample) over it in each direction. The aspect ratio of the height and width of the microchannels is 1:1 (100 μm), which gives a square section avoiding problems related to SU-8 high-aspect ratios structures [234]. In addition, these dimensions are sufficient to ensure that there is enough sample flowing within the microchannel.

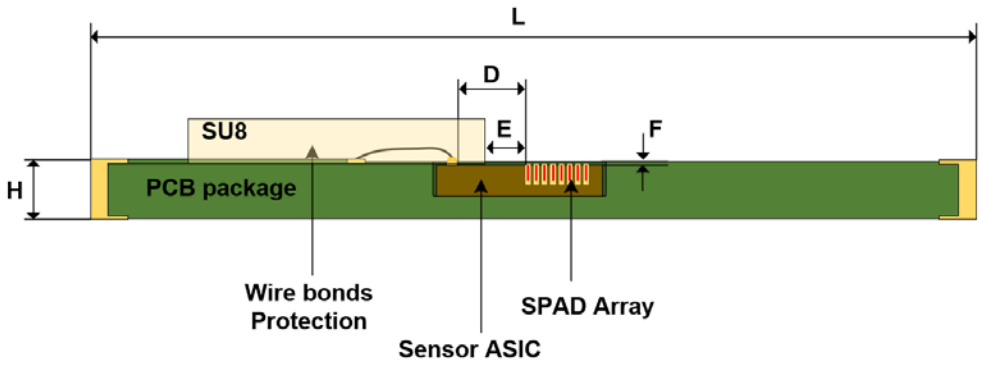

Figure 3.3 Cross-section diagram of the packaged SPAD sensor chip geometry.

Table 3.2 Sensor ASIC Package Characteristics.

Parameter	Value	Unit
Number of SPAD	1 x 10	-
SPAD Pitch (p)	50	µm
D (from contacts to 1st SPAD)	500	µm
E (from wire bonding protection to 1st SPAD)	300-350	µm
F (distance between the surface of ASIC and the surface of the package)	0-100	µm
G (wire bond protection height)	425	µm
Package dimensions (LxWxH)	24x24x0.8	mm

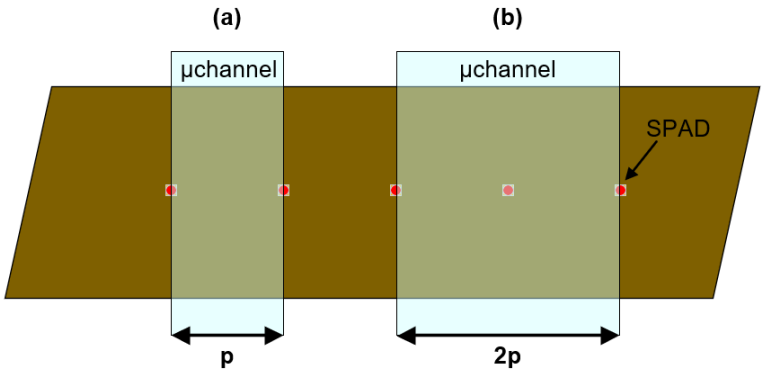

Figure 3.4 Diagram of microchannel overlapped with SPAD array (a) minimum width of 50 µm and (b) doubling the minimum width (100 µm).

The wire bonds protection of the sensor will be used as a physical barrier for the microfluidic chip (Figure 3.5). So, the distance between the edge of wire bonds protection and the first SPAD (E in Figure 3.3) fixes the distribution of the microchannels within the microfluidic chip. In the case of microfluidic chips with a single channel, the channel must be between 300 and 800 µm from the edge of the chip to ensure that it is placed over the SPAD array. For more than one microchannel per chip, the first one must be at most 350 µm from the edge. Once the position of the first microchannel is fixed, the rest is automatically positioned in parallel with a fixed space of 100 µm, maintaining a good aspect ratio for manufacturing [234]. Consequently, the maximum number of microchannels is determined to be 3, because we want all of the microchannels on the sensor array.

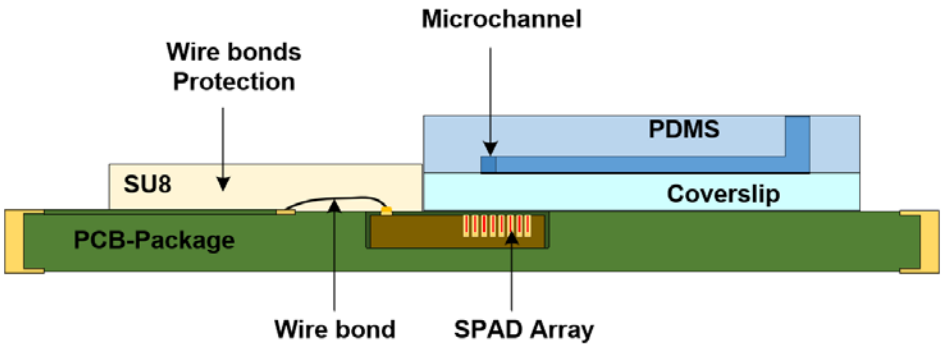

Figure 3.5 Wire bonds protection as a stopper for the microfluidic chip.

Since the introduction and extraction of samples will be done by means of tubes connected to syringe or micropumps, the microchannels must be enlarged at the ends. The widening at the ends allows piercing the inlets and outlets of the microchannel easily.

The thickness of the PDMS cap determines the distance between the excitation light source and the sample. As the system is aimed to avoid the use of focusing systems, the PDMS must be kept thin to ensure that the excitation light source is close enough to the sample, but at the same time thick enough to hold the tubes in the chip. A thickness of 2 millimeters of PDMS presents a good trade-off of both aspects. On the other hand, due to the small active area of the SPAD pixels, the vertical distance between SPAD array and sample (microchannels plane) must be minimized. This critical distance is determined by the substrate used to seal the

PDMS microchannels. The selected substrate was a coverslip of 150 µm thick and 24 x 60mm shape, which puts the sample close to the sensors and fits with the package width size.

Finally, in order to fix the distance between the microfluidic chip edge and the first microchannel, the final design includes a cutting guide of 150µm wide located 300 µm from the first channel.

3.2.3 Final Microfluidic Structures Masks

Following the design guides discussed in the previous section, two different microfluidic structures were designed. The first one presents only one microchannel (M1CH) and the second one integrates three microchannels (M3CH). In Figure 3.6 and Table 3.3, the geometry characteristics of the designed structures are presented.

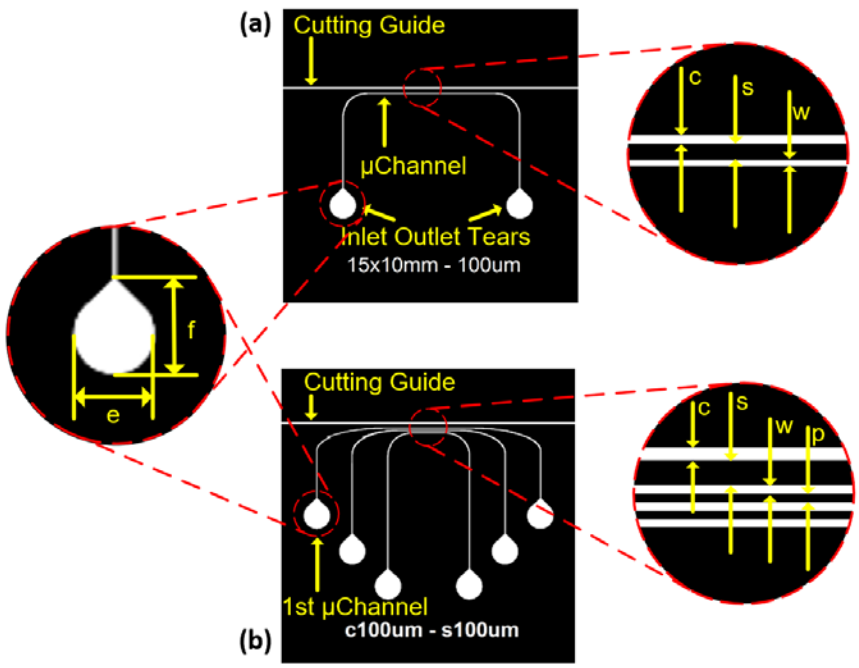

Figure 3.6 Geometry of the one microchannel structure (a) and the three microchannels structure (b).

Table 3.3 Microchannels Characteristics.

Microchannel Parameter	Value	Unit
Number of microchannels	3	-
Pitch (p)	200	µm
Width (w)	100	µm
Height	100	µm
Ending tear width (e)	2.22	mm
Ending tear height (f)	2.62	mm
Distance from 1st microchannel to cutting guide (s)	300	µm
Cutting guide width (c)	150	µm
1st Microchannel Shape (HxW)	18.87 x 5.89	mm
2on Microchannel Shape (HxW)	12.81 x 8.71	mm
3rd Microchannel Shape (HxW)	6.9 x 11.42	mm
Alone Microchannel Shape (HxW)	15 x 10	mm

3.3 Results

The two different microfluidic structures, described in detail in section 3.2 Microfluidic Design, were successfully designed and fabricated using the PDMS lithography replication from the SU-8 mold technique, described in section 3.1. The discussion of the results of each step of the process is in the following subsections.

3.3.1 Microstructures Masks

The CAD designs of the microstructures were transferred into slides by a high-resolution printer at LEICROM S.L., who claims an accuracy of 10 µm. The resulting transparencies (Figure 3.7 a and c) were examined under an optical microscope, in order to measure the microchannels pitch and width, as well as the cutting guide. Figure 3.7 b and d show the results. As can be seen, the designs were well transferred, but they presented a bigger error than we anticipated. Even so, it was small enough to be acceptable.

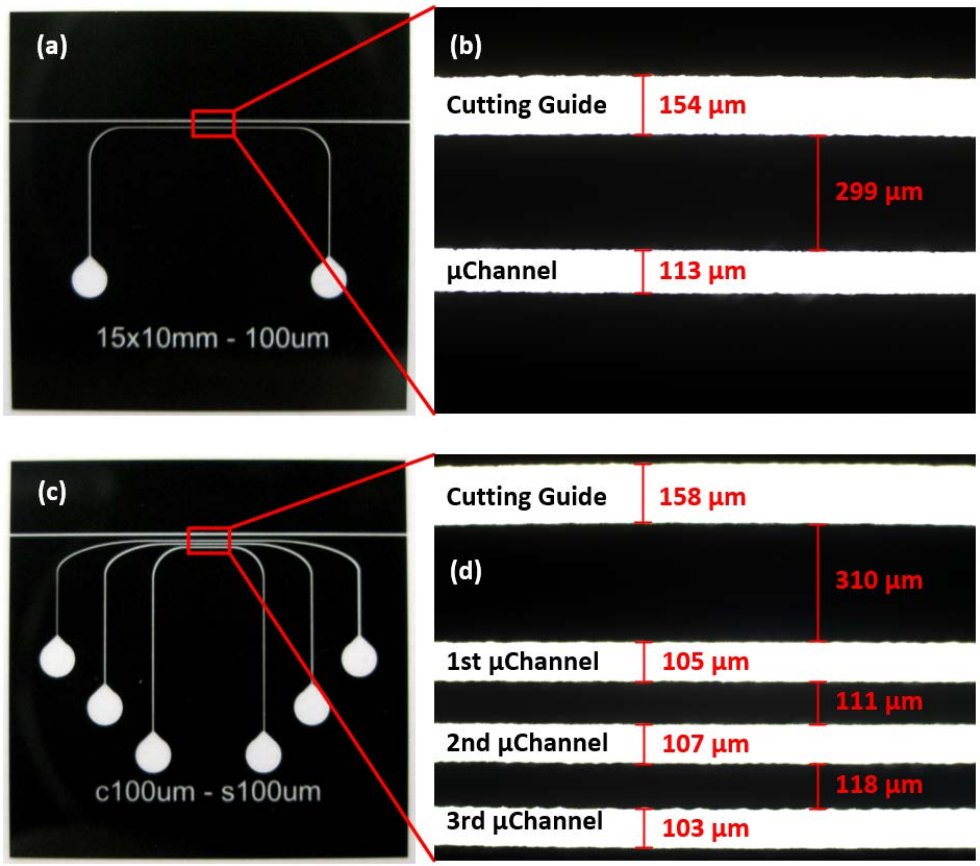

Figure 3.7 Transparency of one microchannel structure (a), Transparency of three microchannels structure (b). Detail of transparency of one microchannel (c). Detail of transparency of three microchannels (d).

3.3.2 SU-8 Mold

The SU-8 mold fabricated onto a microscope glass slide had a well-defined pattern and adhered strongly onto the glass substrate as shown in Figure 3.8 a and c. Examining the microchannels structures under an optical microscope (Figure 3.8 b and d), we observed that microchannels were wider than expected, and the profile of their sidewalls presented a slope (grey areas that limit each microchannel). This was due to an overdose of UV during exposure [235]. The SU-8 structures thickness was measured using a micrometer, obtaining a 111±1 µm thickness. At a spin speed of 3000 rpm, a 100µm structure height should be achieved according to the manufacturer specifications [227]. The reason for this discrepancy was due to the

variances of the SU-8 viscosity, which is temperature-dependent, and the evaporation rate of the SU-8 solvent that makes the resist more viscous [226].

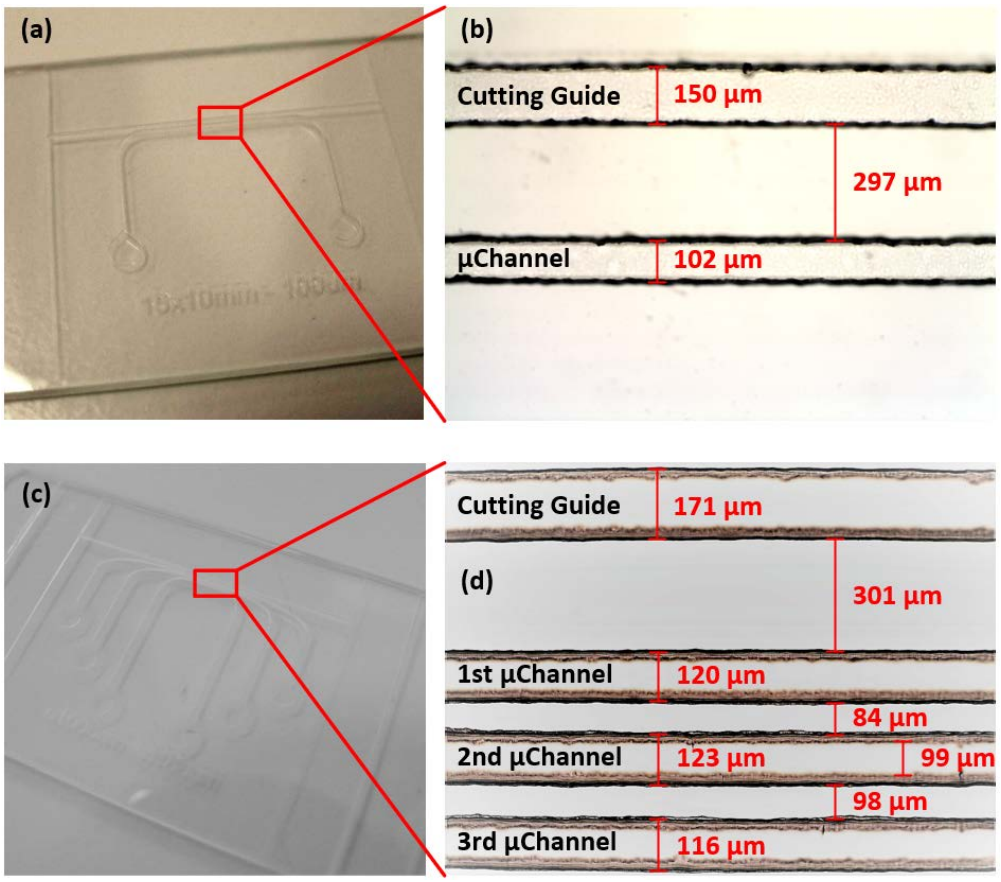

Figure 3.8 SU-8 mold of one microchannel structure (a) and three microchannels structure (b). Detail of SU-8 mold of one microchannel structure (c) and three microchannels structure (d).

3.3.3 PDMS Replica

The PDMS microfluidic chip replicates the SU-8 mold pattern by replica molding technique (see section 3.1). Figure 3.9 shows the obtained PDMS replicas of both designs. The microchannel structures were transferred well to the PDMS, keeping all distances within the acceptable tolerance range. The discrepancies with the measured width on the SU-8 mold were less than 10 microns and could be attributed to the measurement procedure.

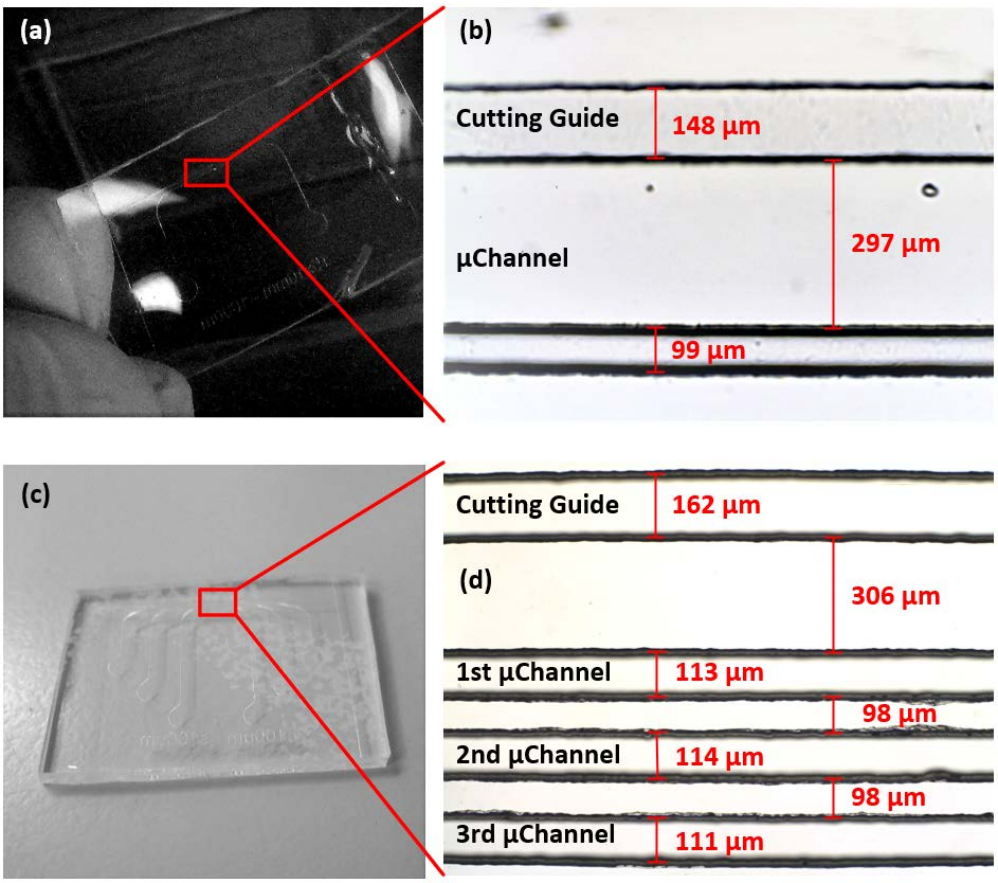

Figure 3.9 One microchannel structure PDMS replica from SU-8 mold (a). Three microchannels structure PDMS replica from SU-8 mold (b). Detail of PDMS replica of one microchannel structure (c). Detail of PDMS microchannels replica of three microchannels structure

3.3.4 PDMS Microfluidic Chip

The critical steps in the manufacturing process were the two irreversible steps made by hand. The first, when the PDMS was cut to its final dimensions, especially when the edge was cut near the microchannels (following the cutting guide). Secondly, during the assembling process between the PDMS and the coverslip, since both edges (from the coverslip and the edge of PDMS near the microchannels) must coincide. For the M1CH cartridge, the bonding and cut process allowed more tolerance because there was only one channel and we had the entire SPAD array to place the microchannel. However, for the M3CH cartridge, the distance

of the first microchannel to the edge of the chip was critical, because all must be over the SPAD array. Figure 3.10 and Table 3.4 shows the resulting microfluidic chips and the final dimensions.

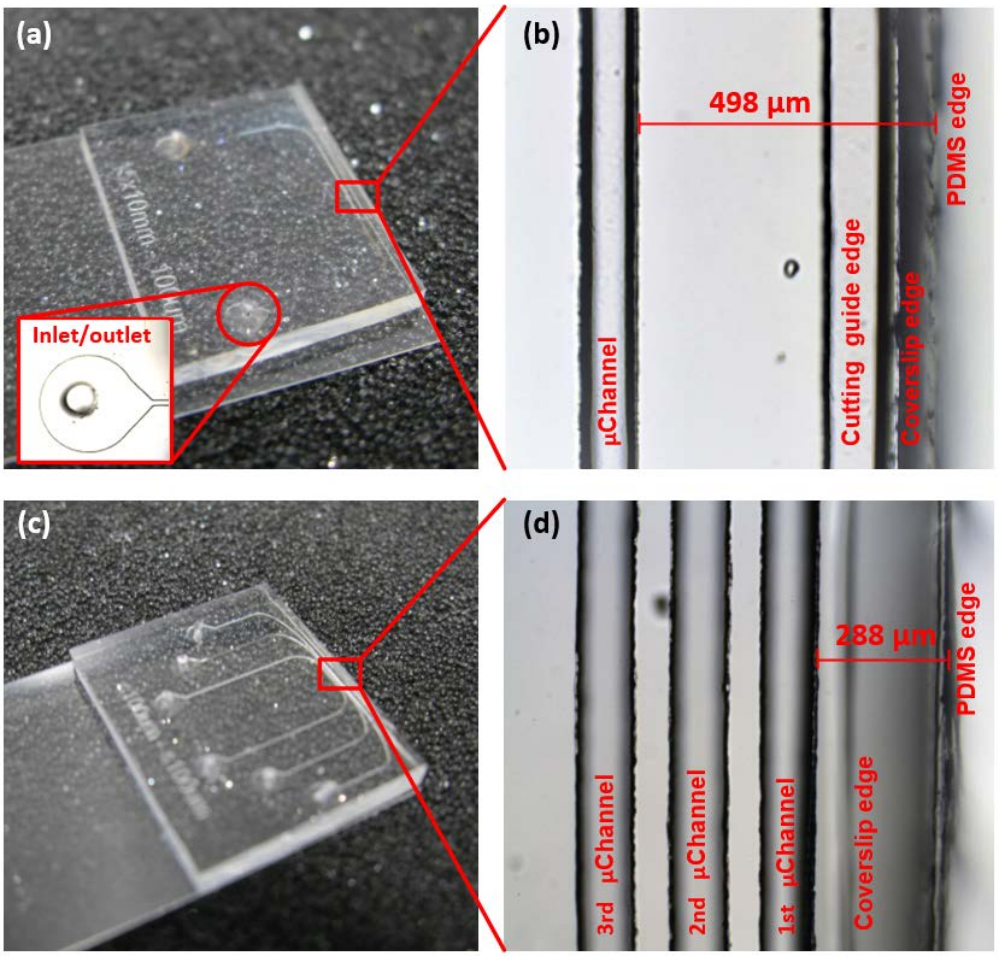

Figure 3.10 The M1CH cartridge (a) and the M3CH cartridge (c). Detail of PDMS and coverslip edges for the M1CH (b) and the M3CH (d) cartridges.

Table 3.4 Final Microfluidic Cartridges Characteristics.

Parameter	Value		Units
Num. µChannels	1 µCh	3 µCh	-
Total thickness	1.87	2.23	mm
Total width	24	24	mm
Total Length	60	60	mm
PDMS Length	15.96	22.89	mm
µCh width	100-115	100-115	µm
µCh height	115	115	µm
µCh pitch	-	200	µm

Figure 3.11 shows a detail of the two final microfluidics cartridges with 1 and 3 independent microchannels over the 10 SPAD pixels sensor array. The channels flowed perpendicular to the SPAD array. The microchannel width guarantees that there would always be one or several SPADs below the microchannels.

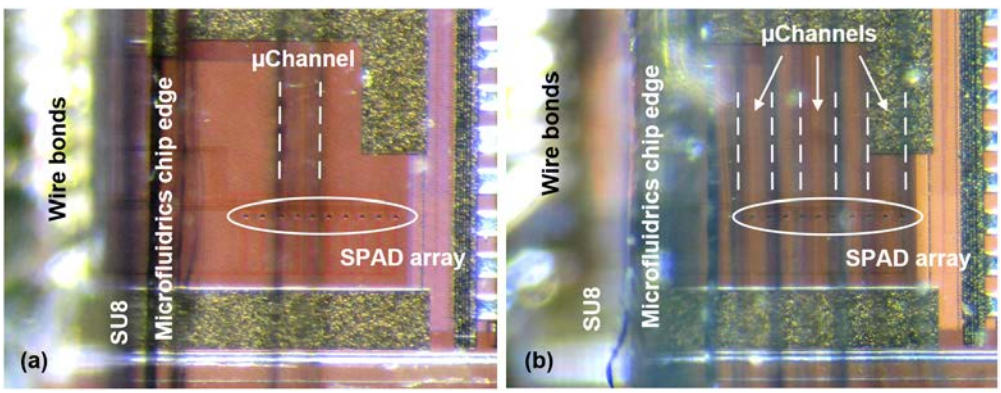

Figure 3.11 The M1CH cartridge (a) and M3CH cartridge (b) over 10 pixels array sensor.

3.4 Summary

Two microfluidics chips (with one and three independent microchannels respectively) were designed and fabricated following a rapid prototyping method. Both microfluidic circuits consisted of a microfluidic structure composed of PDMS (using the Sylgard 184 silicone elastomer kit, Dow-Corning) that was sealed onto the glass. The PDMS cap was build from a mold made with SU-8 photoresist. The resulting PDMS microfluidic structures were approximately 2 mm high and

permanently sealed onto a 150 μm-thick coverslip. The internal design of both chips was well transferred through the different manufacturing stages. The final microchannel structures fulfilled the initial requirements with a thickness of 115 μm and widths between 100 μm and 115 μm due to process variations.

Furthermore, the cutting guide included in the designs was beneficial for cutting the microfluidic chips to their final dimensions, having a success rate of more than 80% when cutting the side of the microchannels. The main sources of error during cut were the contact angle between the blade and the surface of the PDMS, as well as the deformation suffered by the PDMS when exerting pressure to cut it. With an automated control fo the cutting process, the error will be minimized.

In terms of industrialization, the microfluidics applied to lab-on-a-chip for point-of-care applications is considered a disposable product to avoid sample contamination. From this point of view, it is desirable to reduce the cost as much as possible through mass production. Although valuable for rapid prototyping in academic microfluidic applications, the PDMS is not the best candidate for mass production, only 300–1000 units per month according to [236]. Thus, an alternative to PDMS must be found. Other common materials used to manufacture microfluidics are thermoplastics (like PMMA, COP, PS, PM, COC) [237], but they present autofluorescence emission [238] that could distort the fluorescence measurements. The best candidate that we found was a soft thermoplastic elastomer (sTPE), Flexdym, which claims to alleviate PDMS drawbacks in microfluidics (quick prototyping, absorption, and substrate bonding) while keeping the advantages (softness, optical properties, biocompatibility, and gas permeability) [239]. With Flexdym, microchannels of 100 μm width and 1:1 aspect ratio can be performed using a hot embossing machine or straightforward press equipment, making it compatible with rapid manufacturing technology such as injection molding or roll-to-roll.

Chapter 4

Light Source

The excitation light source is another key component of the time-resolved fluorescence instrumentation, being a primary limiting factor in the design of simple instrumentation. Measurement of intensity decays requires a pulsed-light source. Initially, the dominant light sources for TCSPC and fluorescence measurements were flashlamps and picosecond dye lasers [240–242]. With the invention of Titanium-doped sapphire lasers [243], dye lasers were quickly replaced by these which, although still bulky and expensive, are easy to operate. Perhaps the most important development for TCSPC applied to life-science is the introduction of simple solid-state sources as pulsed laser diodes [244–246] and pulsed light-emitting diodes (LEDs) [56, 247, 248]. These devices consume little power, require almost no maintenance, and are easy to operate. Their output can be electronically gated to provide narrow pulses (in the ps-ns range), with repetition rates from a single shot to above 100 MHz. Additionally, the adjustable repetition rate provides an advantage over conventional mode-locked solid-state lasers for noise reduction and precision in the lifetime determination [249]. The advances in LED and laser diode technologies along with miniaturized electronics have enabled TCSPC methods more readily available to a wide range of researchers, thanks to the dramatic reduction in cost and complexity, as well as the instrument footprint.

In this chapter, we discuss the last element of the device, the excitation light source. First, the light source requirements and selection criteria are presented in section 4.1. Finally, in section 4.2, we compare the performance of two driving circuits, pulsing the selected light source.

4.1 Light Source

In order to avoid the use of filters, in addition to the time-gated operation of the SPAD, a light source that can be turned off quickly (before activating the detector) is necessary. The turn off time should be as fast as possible to reduce the time elapsed between the excitation pulse and the observation window, thus minimizing signal loss. As we said above, both LEDs and laser diodes can be driven to obtain pulses of around 1 ns width. Although LEDs are very attractive excitation sources because of their low cost, availability of various wavelengths, stability, long-term use, and straightforward handling. Laser diodes have two key features that make the best candidate for our application: the higher optical output and very narrow emission bandwidth. Higher output power increases the intensity of the fluorescence signal at low concentrations, compensating the signal loss due to the time-gated operation. The narrow emission is interesting to concentrate all the excitation light at the peak of the maximum absorption of the fluorophore. However, their cost is relatively high for the most desired blue range compared to the LEDs.

Finally, the excitation light source selected for our device was a 405 nm laser diode with an output power of 150 mW (L405P150, Thorlabs Inc., US). The excitation wavelength was chosen to be 405 nm, since it provides a close match with the excitation wavelength of many commonly used fluorophores, including the QDs (Quantum Dots) that we will use to validate our device in Chapter 5. Figure 4.1 shows that at 405 nm excitation the Qdot 605 streptavidin conjugate (Q10103MP, Thermo Fisher Scientific Inc., US) absorbs the 40% of the signal.

4.2 Driving Electronics

A wide variety of commercial pulsed LEDs and laser diodes capable of generating pulses as short as 20 ps (FWHM) with repetitions rates up to 100 MHz [250–253] are available. They still have a considerable high price and shape factor that limits the miniaturization of the devices. In the literature, we can find a wide variety of pulse driving circuits for LEDs and laser diodes [254–260]. Although the best option, in terms of miniaturization and performance, is to implement the controller in a monolithic solution such as [58, 257], there are multiple circuits based on off-the-shelf components with outstanding performance, which can be implemented on a small PCB. These circuits commonly use radio frequency (RF) components,

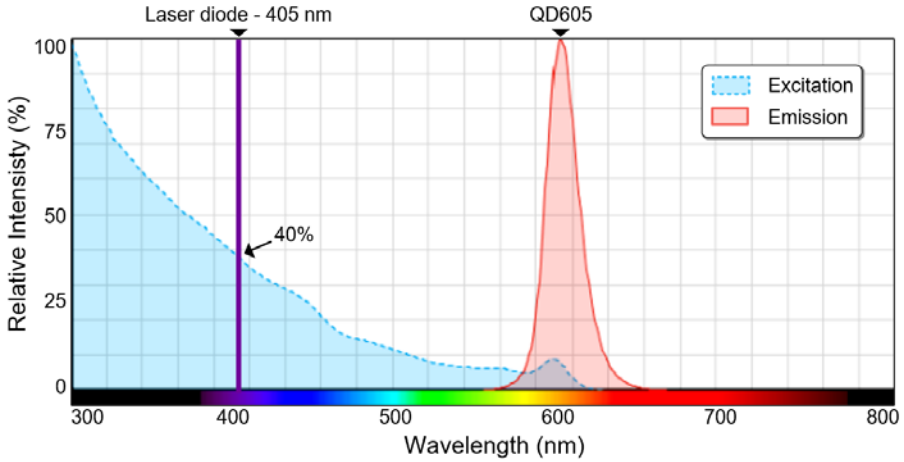

Figure 4.1 Fluorescence specter of the Qdot® 605 Streptavidin Conjugate (Q10103MP, Thermo Fisher Scientific Inc., Waltham (MA), US) [261].

such as avalanche bipolar transistors [55, 262–264], step recovery diodes [259, 265], and bipolar [258, 266] and MOSFET [267] transistors, to generate sharper pulses from a trigger signal.

From the literature, six pulse generator circuits were selected as candidates to driver our laser diode (Table 4.1). The criteria followed was the combination of pulse power, pulse duration, repetition rate, complexity, and the form factor of the entire circuitry, as well as the integrated component to enable miniaturization.

Table 4.1 Pulse generator circuits comparison.

Ref	[55]	[258]	[259]	[260]	[263]	[267]
Optical Power	40 mW peak	355mW peak 1.7mW avg.	tens of mW	1 mW peak 30 µW avg.	20 mW	10 W peak
Pulse FWHM	4 ns	> 60 ps	200 ps	1.9 ns	1.16 ns	100 ps
Repetition rate	< 10 kHz	1 -100 MHz	< 100 MHz	10 kHz -10 MHz	<10 kHz	1 MHz
Complexity	Low	Mid	High	Low	Low	Low
Form factor	Compact	Compact	Mid	Compact	Compact	Compact
Light source	LED	Laser diode	Laser diode	LED	LED	bulk Laser
Wavelength	450 nm	660 nm	420 nm	525 nm	460 nm	870 nm
Based on	Avalanche	RF- BJT	SRD	TTL logic	Avalanche	Power MOSFET

The SDR-based circuit [259] presents an excellent overall performance, but it requires a controlled impedance delay line, limiting the form factor of the PCB. The power MOSFET implementation [267] was discarded due to the high voltage required (> 120V) and the high probability of damaging the device in the long term operation. The TTL logic pulse generator [260] even presenting good repetition rates, its optical power (1 mW) is too low compared with the avalanche [55, 263]. Finally, two different circuits were implemented. The first was based on the avalanche breakdown pulse operation of the bipolar transistors (from now on avalanche driver). The second pulse generator was reported by Uhring et al. in [258] (from now on RF bipolar driver), which is based on standard RF bipolar transistors, presenting an excellent overall performance.

The avalanche driver (Figure 4.2) was implemented using a small signal NPN transistor (2N2369, NXP Semiconductors, Eindhoven, Netherlands). The 2N2369 transistor exhibits avalanching, with performance similar to transistors specified to avalanche at a low price [263, 268]. As the polarization voltage V+ increases, the avalanche generally begins in the range 70-80 volts. Below this voltage, it is required a trigger pulse at the base of the transistor to generate an avalanche. The capacitor C1 serves as storage for the pulse current, and it is charged through the Rbias resistor. This RC time constant sets the maximum repetition rate of the pulses to some kHz. The avalanche transistor creates the pulse by completely discharging the C1. The supply voltage V+ and the capacitor C1 determine the amplitude and the width of the pulse current through the laser diode. This circuit emits a short electric pulse of 1.6 ns FWHM with 10 V peak to peak amplitude at 50 Ω.

The RF bipolar driver is shown in Figure 4.3. At a static operating point, all the transistors are cut-off, and no power is consumed while no trigger signal is applied to the input. When a trigger signal (3.3 V or 5 V) is applied to the circuit input, the transistor Q1 is getting saturated, and then its collector voltage is changing fast from VCC to ground. A rapid voltage ramp is present at the input of the C1−R4 cell. This cell forms a high pass filter with a frequency cut off of $1/\pi RC$ and acts as a differential operator. A negative electrical pulse is obtained at the output of the cell. With regards to the RC constant which is about 500 ps, a narrow nanosecond pulse is generated. Its amplitude depends on the slew rate of the voltage ramp. It is the reason why the saturation of the transistor Q1 must be fast enough,

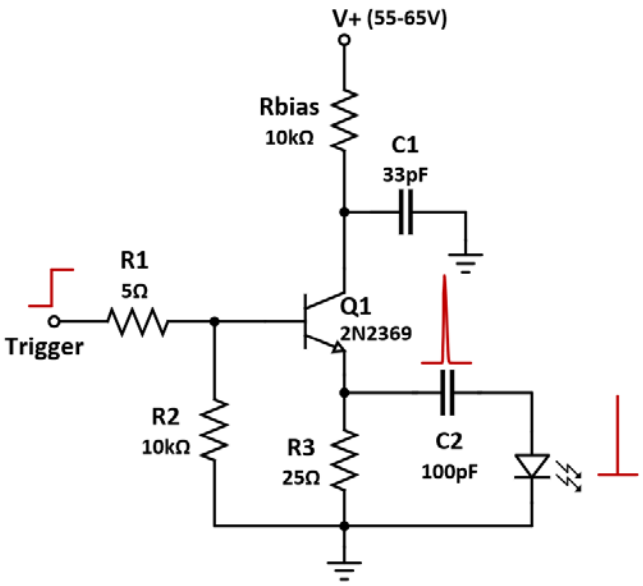

Figure 4.2 Simplified schematic of the avalanche pulse generator.

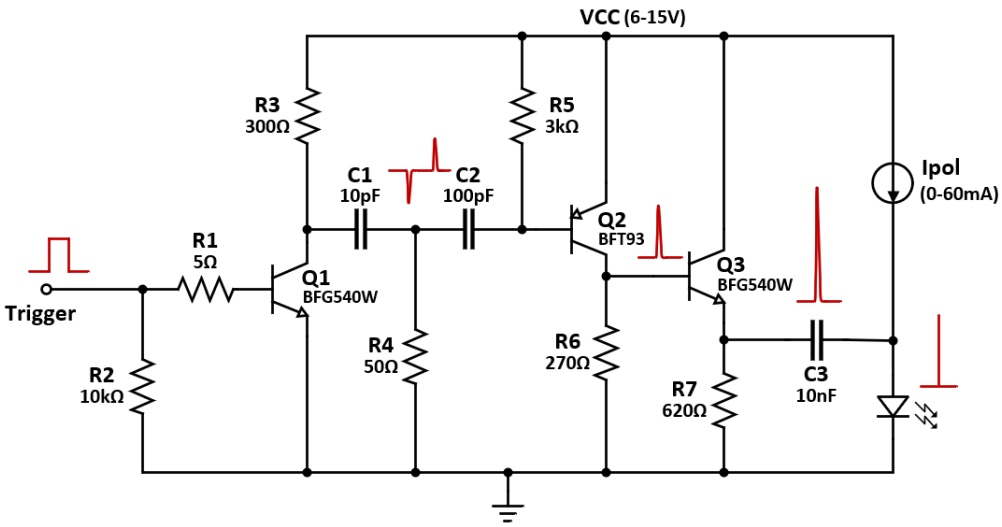

Figure 4.3 Simplified schematic of the RF bipolar driver reported by Uhring et al. in [258].

and the slew rate of the trigger signal must be higher than 1V/ns to ensure a fast switching of Q1. The generated negative pulse is too short for transistor Q2 to be fully saturated, allowing the collector voltage of Q2 to increase and decrease immediately, thus producing a rapid positive pulse. This positive pulse is applied to the input of the buffer amplifier Q3. This last stage allows driving the laser diode directly with the sufficient current (typically about 100 mA). The voltage amplitude of the pulses is adjustable by varying the VCC voltage from 6 to 15 V [258].

Both circuits were implemented on a circular PCB of 25 mm of diameter (Figure 4.4) compatible with cage plate (CP02/M, Thorlabs Inc., Newport (NJ), US) to assemble them in an optical bench. Since the pulse widths generated are in the sub-ns range and the optical peak power requires several tens of milliamperes, special measures were taken to switch such high currents within short time intervals reliably. Some component tweaking was necessary because the intended pulsed laser diode influences the circuit largely.

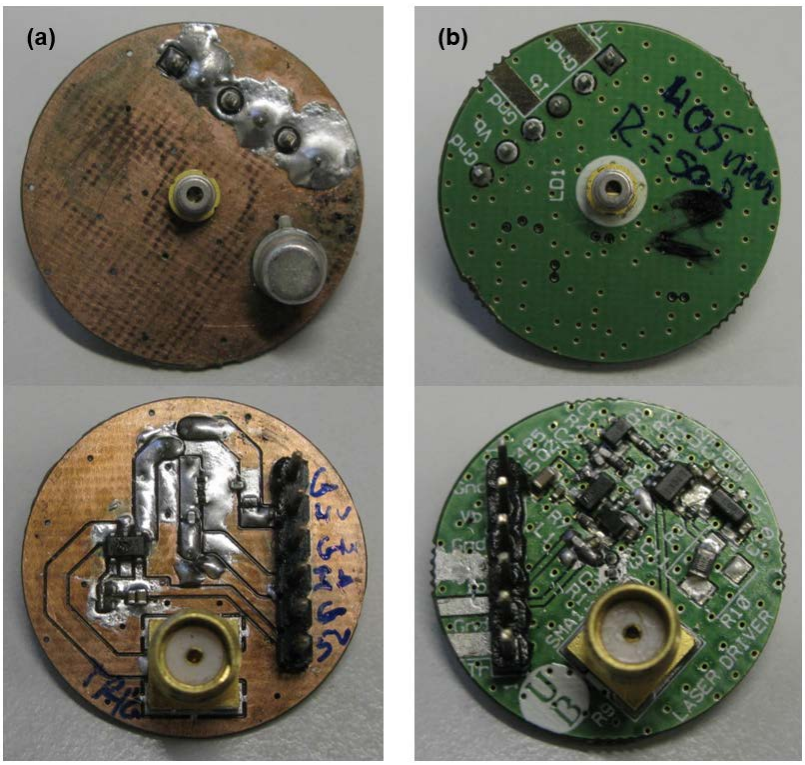

Figure 4.4 Circular PCBs designed (25 mm in diameter) for the laser drivers based on the avalanche transistor (a) and RF bipolar transistors (b).

The electric and optical pulses characterization was performed biasing the circuits at its maximum voltage in order to generate powerful pulses. The avalanche circuit was biased at 65 volts and the RF bipolar at 15 volts. The electric pulse generated at the anode of the laser diodes of both circuits was measured with an oscilloscope (MSO9404A, Agilent, Santa Clara, US) using an active prove (1156A, Agilent, Santa Clara, US). The corresponding optical pulse was captured with an ultrafast InGaAs metal-semiconductor-metal (MSM) photodetector (G4176-01, Hamamatsu Photonics, Hamamatsu, Japan) with 30 ps response time for both rise & fall time and low dark current (100 pA at 25 ºC). The photodiode was biased at 10 V, and its electric output was connected directly to the oscilloscope with a coaxial cable of 50 Ω impedance. The laser diode faced to the photodetector in direct contact (Figure 4.5).

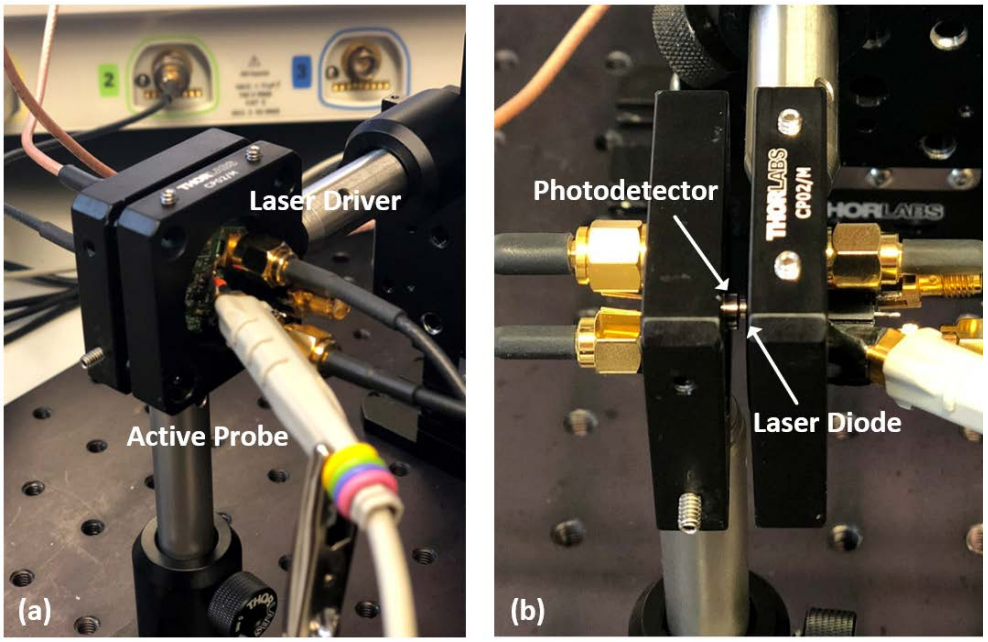

Figure 4.5 Optical setup used to measure the electric and optical pulse generated by both laser driver circuits (a) and detail of laser diode facing the photodetector (b).

4.2.1 Electrical Characterization

Figure 4.6 shows the measured electrical (at the laser diode anode) and optical pulses for both circuits, at operating frequencies of 10 kHz. Although both circuits drive the laser diode with sharp electric pulses, the avalanche driver presented better performance generating a electrical pulses of 12.5 V, ~970 ps at FWHM and a fall time of ~896 ps (time to decrease from 90% to 10% of the signal peak) than the RF bipolar driver, which generated pulses of 7.5 V, 1.25 ns at FWHM and ~1064 ps of fall time.

After the respective peaks, both signals go down (below 0 V), driving the laser diode to reverse bias. In the case of RF bipolar driver, this reverse bias was applied during 4.5 ns with a minimum of -2.7 V at 4 ns. Then the signal increases rapidly generating some oscillations (with an overshoot of 7.3% of the peak) stabilizing after 10 ns from the main peak, which set the maximum repetition rate at 77 MHz. For the avalanche driver, the period of reverse polarization is much longer 80 µs (Figure 4.7) because the recovery follows an exponential function with a time constant driven by the C2 and resistance of the laser diode reverse biased (which is in the MΩ range). The long recovery time limits the repetition rate to 12.5 kHz without degradation of the generated pulses. This slow recovery is not present in circuit 2, because the Ibias injected into the laser node (typically through an inductance of several µH [259, 265]) quickly stabilizes the node, even with 0 mA of Ibias (with the inductance connected to ground, which is our case using a inductance of 5.6nH). Although the minimum voltage reached by the avalanche driver was -3.6 V at 25 ns, which is dangerous for the integrity of the laser diode. However, the laser diode does not run in reverse polarization (below -2V) more than 100 ns.

4.2.2 Optical Characterization

The corresponding optical pulses generated (Figure 4.6) by each circuit present widths of ~122 ps and ~602 ps at FWHM with fall times of ~341 ps and ~836 ps for the avalanche and RF bipolar drivers, respectively. From the captured waveforms, it was observed that pulses present different shapes. The avalanche driver generates a narrow pulse with a wider base, while the RF bipolar driver shows multiple emissions pulse. Also, the optical pulses present a turn-on delay that is governed by the carrier lifetime (in the order of several ns) and the initial bias

current [269]. Further, both optical pulse tails present oscillations. Both effects become more evident while varying the operating frequency (Figure 4.8). In both circuits, at higher frequency operation, the nodes of the circuits cannot be completely charged, which results in less powerful pulses, thus lower current injection. On the other hand, the increase in the injected current stimulates the ringing phenomena produced by step current pulse. These relaxation oscillations result from an interplay between photon number and carrier density with their respective lifetimes τ_{ph} and τ_e. Since for usual laser diodes these lifetimes differ by about three order of magnitude with $\tau_{ph} \ll \tau_e$ a considerable ringing occurs, producing secondary emissions that broaden the primary peak [270].

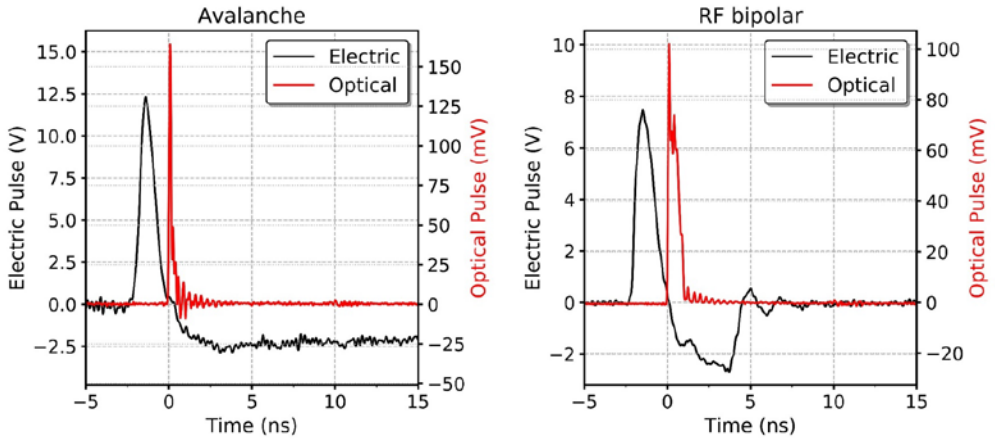

Figure 4.6 Electric and optical pulses waveforms captured with an oscil·loscope for both laser diode driving circuits.

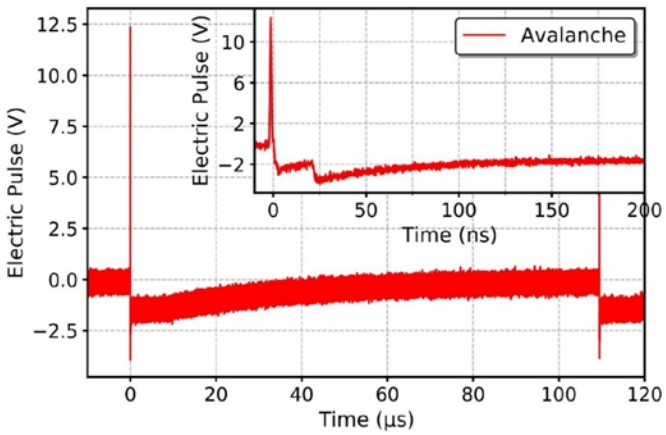

Figure 4.7 Plot of the full recharge period of the avalanche driver with an inset view of the two minimums.

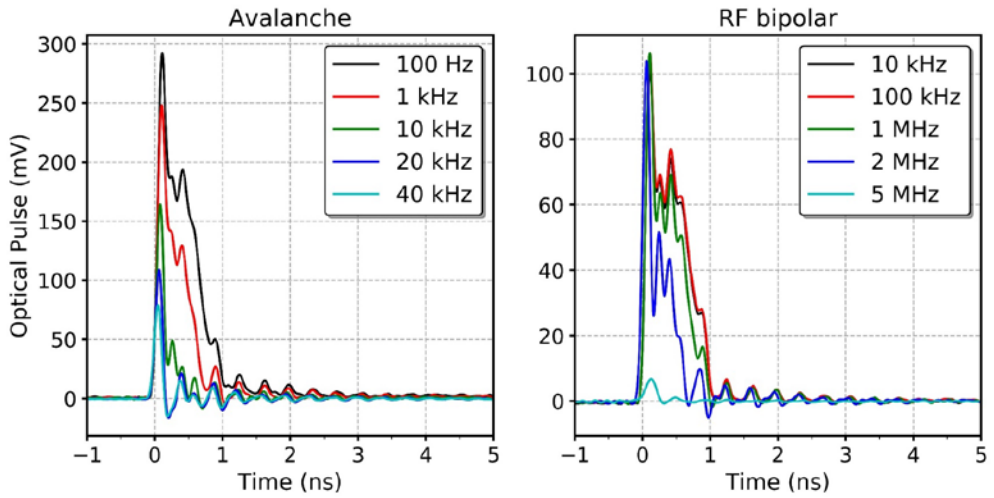

Figure 4.8 Optical pulse shape for different operating frequencies (left) for the avalanche driver and (right) for RF bipolar driver.

Figure 4.9 shows the key parameters in terms of sample excitation for time-resolved fluorescence (intensity peak, fall time, and FWHM) of the optical pulses for different operating frequencies for both circuits.

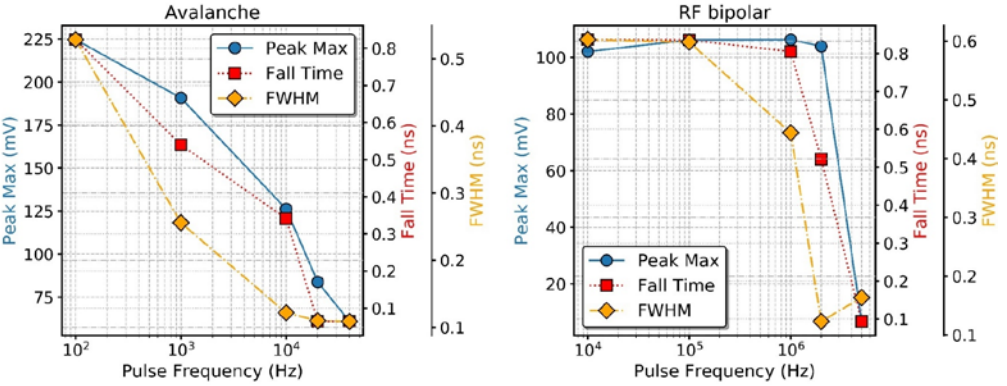

Figure 4.9 Key parameters of the optical pulses for different operating frequencies for (left) avalanche driver and (right) RF bipolar driver.

The two driving circuits are capable of generating sub-nanosecond optical pulses with fall times from ~64 ps to ~824 ps and ~93 ps up to ~836 ps for the avalanche and the RF bipolar drivers, respectively. The avalanche driver is capable of generating more powerful pulses at low frequencies. However, to obtain the results

quickly with sufficient statistics to be able to reconstruct the decay time of the fluorescence, the repetition rate plays an important role. Therefore, a good trade-off between the three parameters could be the operation of the avalanche driver at 10 kHz, because it allows doing 1 million repetitions in less than two minutes with a reasonable optical power in the primary peak compared to the RF bipolar (about 34% more powerful). For the RF bipolar driver, the best operation frequency is 1 MHz, where the optical power is maximized, and the optical pulse presents a width of ~444 ps (FWHM), a falling time of ~800 ps. The FWHM at 2 MHz is very small (~123 ps) compared with lower frequency pulses because the measured with at FWHM corresponds only to the primary peak.

Regarding the tail oscillations, the optical pulse response of the MSM photodetector is convoluted with the optical pulse, according to the manufacturer datasheet [271]. In order to shed some light on the tail issue, we measured the optical pulse using the TCSPC technique. The TCSPC was performed using the pixel array with external timing circuit described in section 2.2.2, with an average resolution of 68 ps. The SPAD pixel used had a DCR of 9.9 kHz. No focusing optics was used to avoid the SPAD saturation. The count rate was kept below 5% of the number of repetitions to ensure a reliable reconstruction of the optical pulse. Figure 4.10 shows the optical setup used in dark environment.

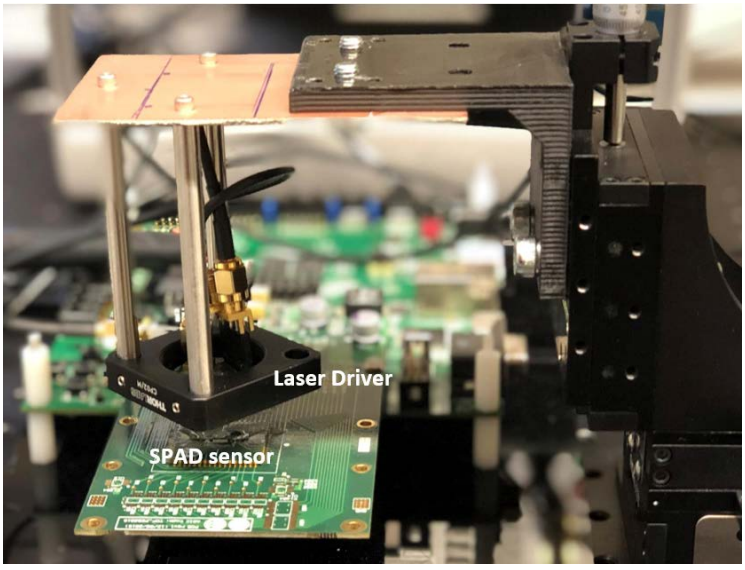

Figure 4.10 Test setup used to measure the optical pulse by means of TCSPC.

Figure 4.11 shows the optical pulse measured with the TCSPC technique together with the pulse measured with the MSM sensor system, for both driving circuits operating at the optimal repetition rate (10 kHz and 1 MHz). The shapes of the pulses measured in both systems are quite similar. As expected, the oscillations of the tail disappear into the measurements performed with the SPAD system, since these were due to the response to the optical pulse of the MSM sensor. Without the oscillations, a knee at the end of the falling edge can be seen. These knees are due to lateral diffusion in laser diodes without or with weak lateral carrier confinement [270]. In the inset representations, the pulse tail is magnified through logarithm representation (for 20 ns), which exhibits an exponential decay at very low intensities as a consequence of the carrier diffusion. This effect limits the minimum concentration that can be detected.

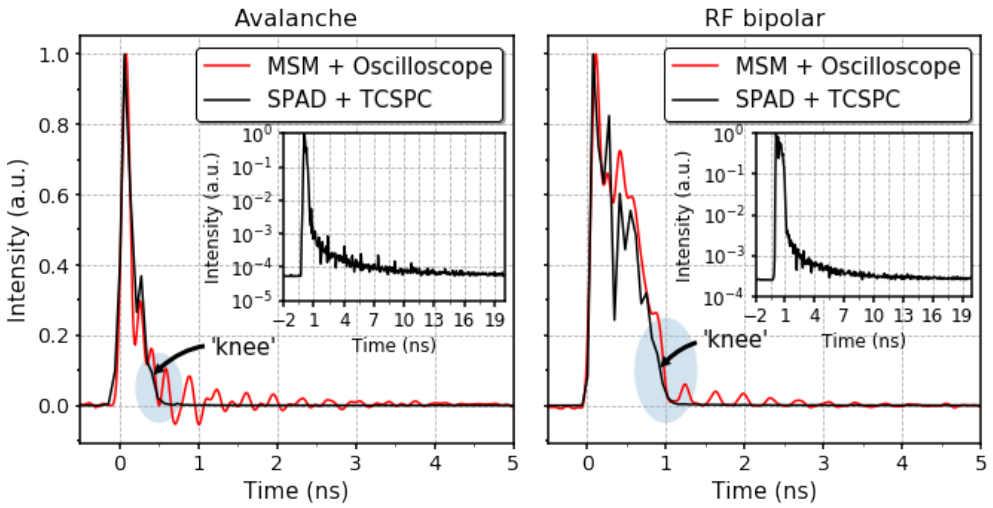

Figure 4.11 Comparison of the optical pulses measured with the MSM photodetector system and the SPAD using the TCSPC technique. The optical pulse generated by the avalanche driver at 10 kHz (left) and the bipolar RF driver at 1 MHz (right). The inset graphs are the logarithmic representation of the SPAD measure showing 20 ns of the pulse tail. The measurements have been normalized for easy comparison.

4.3 Summary

In this chapter, dedicated to the light sources for lifetime fluorescence measurement, we studied two driving circuits that claim the generation of sub-nanosecond light pulses using LED and laser diodes. In our case, the light source selected to

excite the emission of the quantum dot is a 405 nm laser diode (L405P150, Thorlabs Inc., Newton (NJ), US). We implement both circuits to test their performance driving the selected light source. Since the final device is aimed to employ the time gating instead of emission filters (to subtract the excitation light from the observation window), we paid particular attention to the turn-off of the light and how the tail of the optical pulse decays in order to establish the elapsed time between the laser pulse and the observation window.

The two circuits generate optical pulses of ~122 ps and ~444 ps at FWHM (for the avalanche driver and RF bipolar driver respectively) and lower intensity secondary emissions that broaden the primary peaks. We also observed that the tail of the optical pulse is mainly dependent on the laser diode itself. With both circuits exhibiting a similar low-intensity pulse tail of 15 ns. However, the avalanche circuit generates pulses with 34% more optical power in the primary peak, but with lower repetition rates (10 kHz) compared with 1 MHz of the RF bipolar driver. Since both circuits require almost the same time to stop the emission of light, the optical power of the pulse becomes the key factor to excite lower sample concentrations. Therefore, the excitation circuit used will depend on the measurement needs in terms of power and repetition rate.

Chapter 5

Point-of-Care Device for Molecular Diagnosis

The integration of microdevices has enabled the miniaturization of clinical diagnostic methods and measuring equipment for decentralized testing and patient self-testing, named POCT. POCT is important in settings where timing is critical (e.g., emergency triage), where laboratory facilities are nonexistent (e.g., in field assays) and where resources are low (e.g., in developing countries) [73]. In addition, POCT plays a fundamental role in personalized medicine, identifying sets of disease-specific biomarkers to prescribe the most suitable treatment with maximal effectiveness and minimal potential for adverse effects [272].

The desirable features of POC devices, either for human health and environment preservation, can be summarized as a simple test. This simple test should accomplish: (1) quick and reliable response; (2) accuracy within sensitivity/specificity and detection limits needed for the specific application; (3) ease of use, the test should be performed by unskilled people or with low training, and the results should be clear and easy to understand; (4) self-containment, users should only collect the sample and deliver samples into the device minimizing user manipulation; (5) portability and robustness for in-field analysis; (6) low-cost, platform should be affordable for public healthcare systems, as well as for user and patients; (7) ideally with multiplexing capacity, performing more than one analysis simultaneously to enable the full characterization of a biological sample [64].

Clear examples of common use POC devices are the pregnancy test [273] and control of blood glucose concentration [274], but various emerging tools for more complex clinical or home management of diseases are also gradually spreading [275]. In [276] Chin et al. makes a critical review of companies that work developing POC devices for its commercialization, of which many are based on steady-state fluorescence detection. A good example is MBio Diagnostics that developed a fluorescence-based reader to perform multiplexed immunoassays using a single microfluidics cartridge [277–279] as well as environmental assays [280]. However, despite the benefits of the fluorescence lifetime measurement, in terms of multiplexing and background rejection, it has not been commercially exploited in POC devices. Even with the modern technologies and manufacturing techniques, which allows the miniaturization of the instrumentation into completely integrated systems with the potential for volume production.

In this chapter, we report the assembling of two low-cost general propose POC devices based on the different components and techniques outlined in previous chapters. Finally, the performance of both devices is evaluated by simulating a bioassay, measuring the fluorescence lifetime of QDs.

5.1 Materials & Methods

5.1.1 Materials

In Table 5.1, the commercially available elements used to build and test the POC are listed. The SPAD array chip is included. It was custom designed and fabricated with a multi-project wafer in a 0.18 HV-CMOS process. The basic electronic components are not listed for simplicity. The initial investment is high due to the raw materials such as SU-8, PDMS, conductive epoxy, and the FPGA development board. The final cost of the prototype is approximately 990 € that is affordable compared to desktop commercial equipment. The cost of facilities to perform soft-lithography and wire bonding are not included.

Table 5.1 The basic components needed to construct the PoC. The costs for raw materials are divided by the estimated number of devices that can be manufactured with them [53].

Components	Approx. Cost	Cost per Device	Notes
SPAD sensor chip (40 dies fabricated in a multi-project wafer)	7000 €	175 €	
Zedboard Zynq-7000 Development Board from Digilent	422 €	422 €	
3-D printed spacer	30 €	30 €	
Daughter card (includes all electronic parts and components)	110 €	110 €	
Sensor Packaging			
Substrate based on a printed circuit board	66 €	66 €	
Conductive epoxy (CW2400, Chemtronics, Kennesaw, US)	100 €	2 €	
SU-8 100 (Microchem Company, Newton (MA), US)	860 €	8.6 €	1
Laser driver circuit components			
Laser driver circuit DC supply for V+ (includes all electronics parts and components)	96 €	96 €	
Laser diode 405 nm and 150 mW (L405P150, Thorlabs Inc., Newton (NJ), US)	83 €	83 €	
Microfluidics materials			
PDMS (Sylgard 184 kit, Dow Corning, Michigan (MI), US)	170 €	3.4 €	2
Glass coverslip (12460S, Thermo Fisher Scientific Inc., Waltham (MA), US) (1000 units)	55 €	0.055 €	
Fluorophore label			
Qdot® 605 Streptavidin Conjugate (Q10103MP, Thermo Fisher Scientific Inc., Waltham (MA), US)	203 €		
500 ml of saline solution (PBS-PH7.4, Gibco® by life Technologies™, New York, US)	12 €		

1. Around 5 ml are used to encapsulate one SPAD sensor. 2. Around 50 devices can be manufactured with 1.1 kg of PDMS.

5.2 System Integration

Two versions of the POC device were developed. In the first approach, the pixel array with external timing circuit (described in Chapter 2 section 2.2.2) was used to detect the fluorescence emission and reconstruct the decay rate histogram. In the second approach, the pixel array with analog histogramming on-chip (described in Chapter 2 section 2.2.3) was implemented to measure the decay histogram directly.

In both devices, the system was built around the SPAD sensor chip, stacking the microfluidics and the light source over it in a sandwich structure (Figure 5.1). We developed a custom packaging to straightforward stacking the microfluidic cartridge over the SPAD array without any alignment procedure.

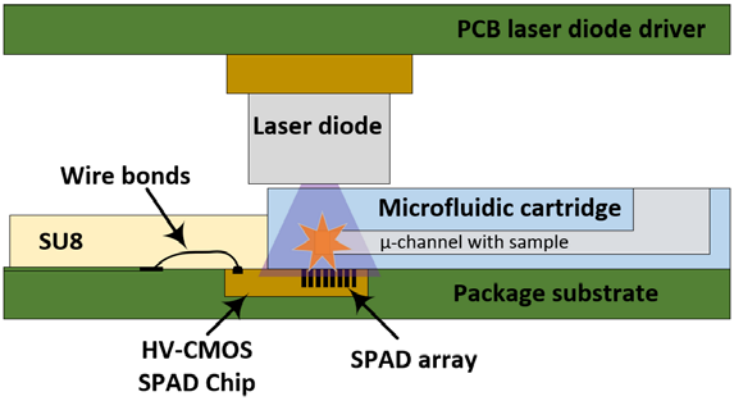

Figure 5.1 Cross-sectional sketch of the stack-up of the POC system. The sample is introduced in one of the microchannels of the microfluidic cartridge, which is directly positioned on top of the SPAD array, where the wire bonds encapsulation with SU-8 prevents it from entering further [53].

The chip was assembled on a dedicated PCB, where it was wire bonded. This packaging PCB had a recess into which the chip could be inserted. The chip was glued with a conductive epoxy (CW2400, Chemtronics, Kennesaw, US) into the recess so that its surface was flat with the PCB, allowing the microfluidic chip to be placed on top of it. SU-8 was used to encapsulate the wire bonds (Figure 5.2.a) as described briefly later in section 5.2.1. The SU-8 encapsulation covered a surface of 4.6 mm × 12 mm and extends 200 µm over the chip from the edge of the pads, leaving a margin of 300 µm to locate microfluidic cartridge. The SU-8 is 450 µm tick, which is enough to act as a barrier for the microfluidic chip (Figure 5.2. b and c). Figure 5.2.d shows in detail the microfluidic chip on top of the microelectronic chip. Figure 5.2.e presents the central part of the microfluidic chip containing 3 microchannels that are on top of the pixel array with analog histogramming on-chip.

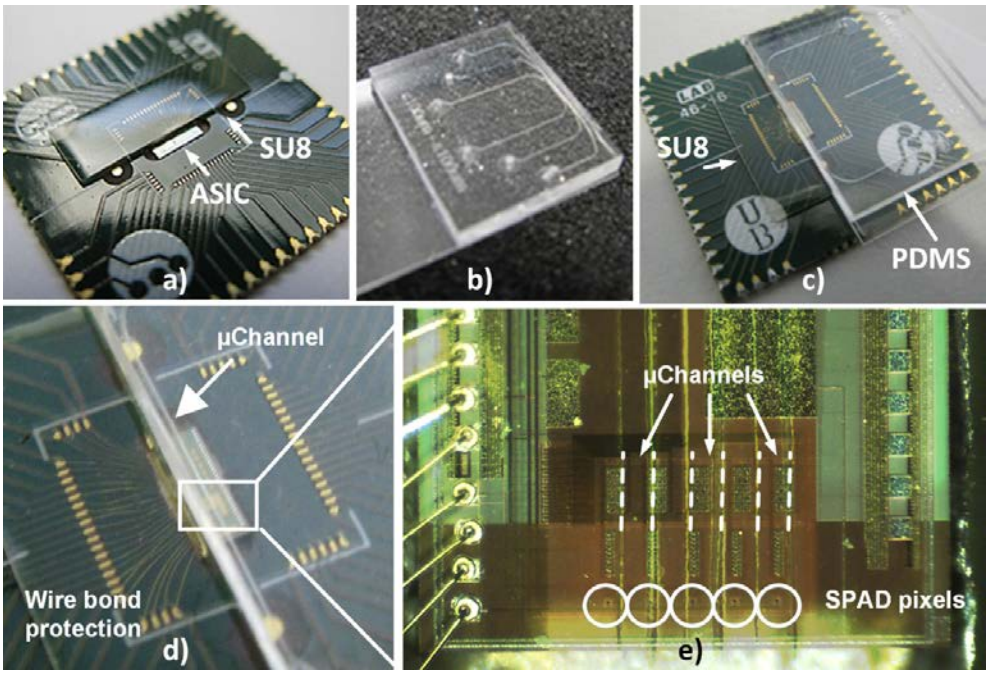

Figure 5.2 (a) PCB showing the recess and the fully encapsulated SPAD sensor array chip using SU-8 to protect the wire-bonds. (b) Microfluidic chip containing 3 microchannels. (c) SU-8 as a barrier for the microfluidic chip located on the PCB with the detector chip. (d) The SPAD sensor array and the microfluidic chip on top. (e) Detailed view of the microfluidic chip on top of the pixel array with analog histogramming on-chip which has a 100 µm of pixels pitch [54].

5.2.1 Sensor Packaging

The combined PCB and chip were subjected to a dehydration bake at 150 °C for 15 min., SU-8 100 (Microchem Company, Newton (MA), US) was spin-coated onto the board at 1000 rpm for 30 s, using a process based on the recommended conditions in the SU-8 datasheet [227]. The soft-bake was performed using temperature ramping from room temperature to 65 °C and holding for 30 min, increasing to 95 °C and maintaining for 90 min and slowly cooling down to 40 °C before exposure. The same scheme was followed for the post-exposures bake but changing the times to 10 and 30 min, respectively. These heating by temperature ramping and slowly cooling down, reduce the stress and any adhesion problems caused by the different thermal expansion rates of the SU-8, the PCB, and the sensor chip [53, 229].

5.3 POC Architecture

The architecture of the POC is compatible with both SPAD-based circuits. The implemented topology provides flexibility during the design and test of each subsystem independently, as well as it allows easy replacement of any part without compromising the rest of the system.

A dedicated PCB daughter card was designed to hold the system stack, which consists of a sandwich structure including the SPAD sensor chip, the microfluidic cartridge and the UV laser diode (Figure 5.3). The packaged SPAD sensor chip was situated on top of the daughter card. The laser diode and its driver were implemented on an auxiliary PCB, connected to the daughter card, and placed over the SPAD sensor chip facing the laser diode against the sensor array. The minimum distance between the laser diode and the SPADs detectors were given by the microfluidic cartridge height (2 mm). A plastic spacer was designed to house the stacked system, setting the distance between the laser diode and the SPAD array at 3 mm. The spacer includes an opening on one side used to insert and guide the custom microfluidic cartridge over the SPAD array. Figure 5.4 shows the complete POC configuration and the designed daughter card with the system stack-up.

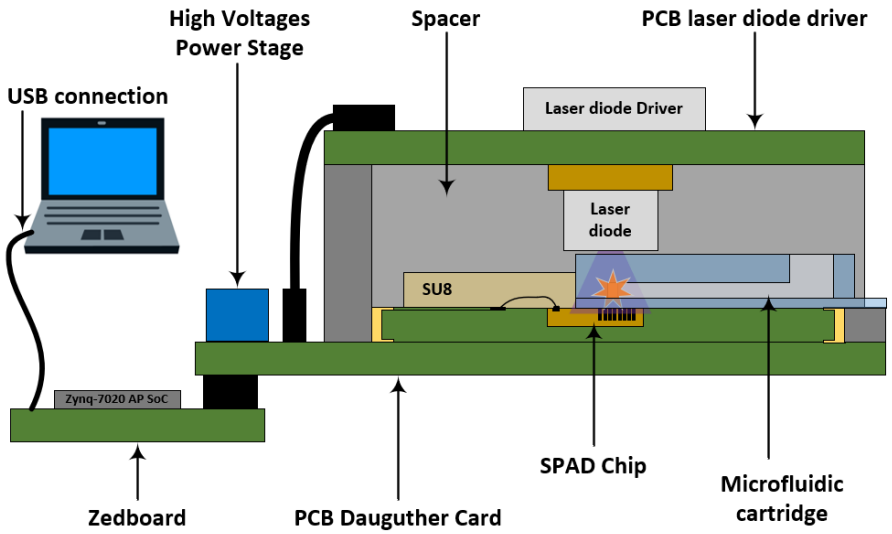

Figure 5.3 Schematic diagram of the complete PoC system with a detailed system stack [53].

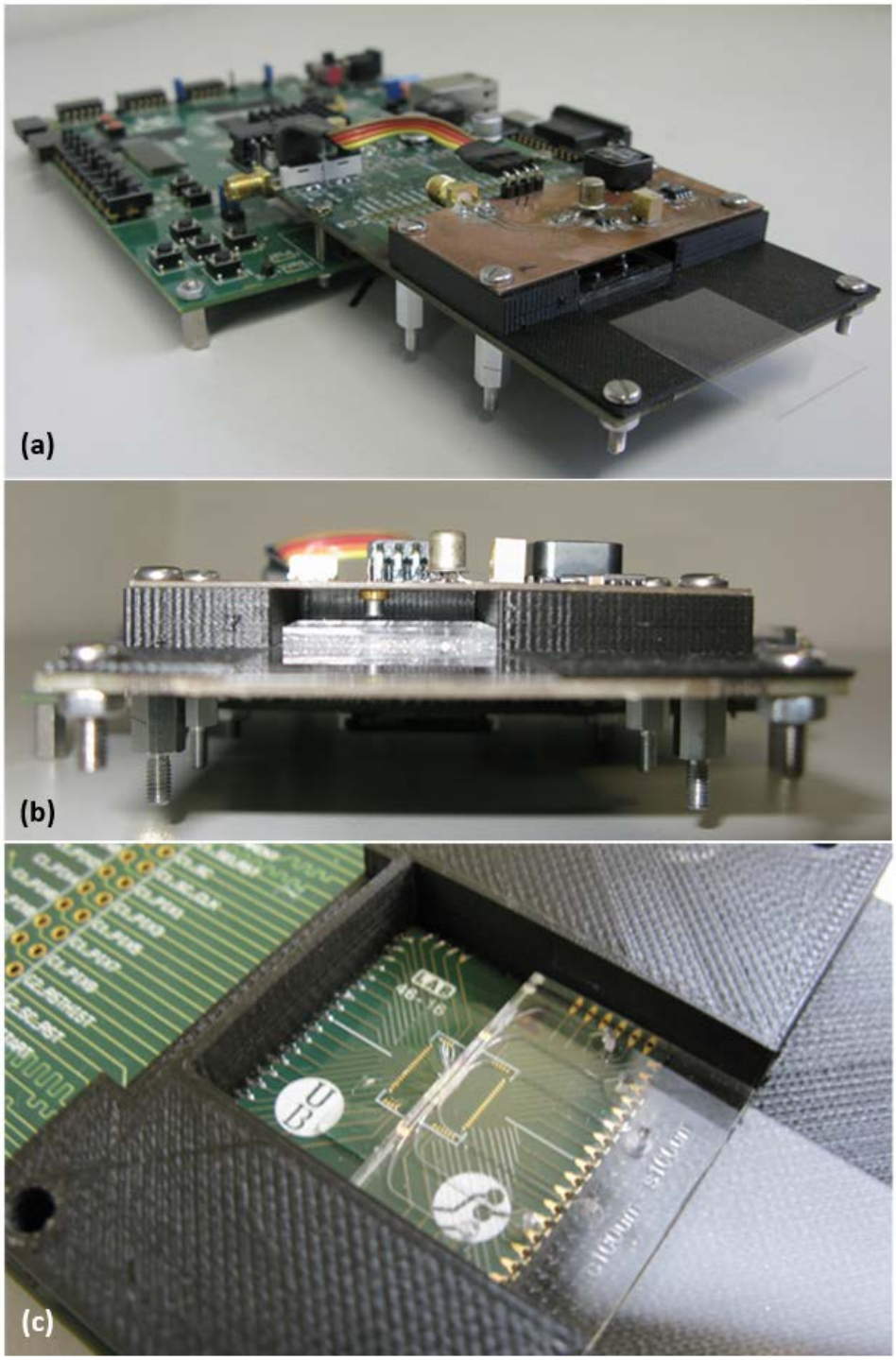

Figure 5.4 (a) Image of the POC device. (b) Side view of the microfluidics in the slot. (c) Detail of microfluidic cartridge guide over the SPADs sensor.

The Z-7020 system controller is mounted on a Zedboard commercial development board connected to the daughter card via FPGA mezzanine card (FMC) connector. This electrical connection includes all the digital signals, as well as the low voltages and ground supplies. The high-voltages bias required by the SPADs sensors and laser diver are generated from the 3.3 V supply of the Zedboard by a power stage implemented on the daughter card. A micropower DC-DC converter (LT1073CS8, Analog Devices, USA) in combination with two low-dropout regulators (LT3062, Analog Devices, USA) generated the high-voltage needed to bias the SPAD (> 11.6 V) and the laser drivers (>50 V). The daughter card also has the ADCs and the programable power stages required by the pixel array with histogramming on-chip circuit.

The Z-7020 receives the measurement configuration parameters, controls data acquisition. For the pixels array without timing electronics, Z-7020 processes the pixel output by performing the TCSPC technique, while for the analog circuit reads the ADCs connected to the analog bins outputs. Finally, the Z-7020 sends the generated histogram to a PC via USB for visualization and removal for life.

5.4 POC Validation as a Fluorescence Lifetime Detectors

The two POC configurations were validated as a detector for time-resolved fluorescence with the setup shown in Figure 5.4. A microfluidic circuit carrying a fluorescent dye was embedded between the excitation laser and the SPAD detector to emulate a biomolecular assay in a POC device. Molecules traditionally used for fluorescence detection are organic. However, they have several drawbacks, such as poor color, susceptibility to photobleaching, and a broad excitation/emission spectrum [281]. In this work, we validated the circuit with photoactivatable Quantum Dots (QDs), i.e., semiconductor nanoparticles that are a promising alternative to organic fluorophores for fluorescence-based biological imaging applications [282] due to their extraordinary photo stabilities, as well as their narrow and more symmetrical emission spectra. Furthermore, QDs have a fluorescence lifetime of 20-50 ns, which is about 10 times longer than those of organic fluorophores (lifetime ~1-5 ns). These longer lifetimes makes them perfect candidates

for systems that use time-gating to subtract the excitation light source form the observation window [54].

The QD used here was the Qdot 605 streptavidin conjugate (Q10103MP, Thermo Fisher Scientific Inc., Waltham (MA), US), which has a maximum fluorescence emission at 605nm (Figure 4.1). Concentrations from 1 µM to 31.25 nM of the QD were prepared by diluting in phosphate-buffered saline (PBS) solution (PBS-PH7.4, Gibco® by life Technologies™, New York, US) and were inserted in different microfluidic cartridge. An effective sample volume of 20 nanoliters (microchannel volume illuminated by the laser spot, based on the laser beam divergence and distance) was excited to obtain each decay curve.

All the experiments were carried out in conditions that ensured sufficiently low numbers of emitted photons to avoid pile-up, i.e., a count rate of less than 20% [12, 149].

5.4.1 POC Based on the Pixel Array with External Timing Circuit

5.4.1.1 System Setup

In order to successfully perform time-resolved fluorescence lifetime analysis, the timing electronics was implemented in the Z-7020 device of the Zedboard. The control unit was modified to control the laser pulse timing through a delay selector module. Figure 5.5 shows the architecture of the final data acquisition implementation, that can be summarized as:

- The Control Unit implements the TCSPC algorithm and controls the rest of the modules to carry out a fluorescence measurement and the histogram reconstruction.
- The TDC is the key module of the system that provides the time resolution.
- The Asynchronous FIFO used to store TDC output and as clock domain crossing (CDC).
- Encoder and Histogrammer, together with memory used to build the time histogram of the measure.

- SPAD driver, generates the SPAD control signals (RST, INH, and ENCNT).
- The Delayer module is used to delay the trigger signal of the SPAD signal generator and the laser trigger signal independently.
- Bare-metal C program on the ARM processor that receives configuration parameters, process results and send them through USB/UART to the PC for data visualization and further analysis.

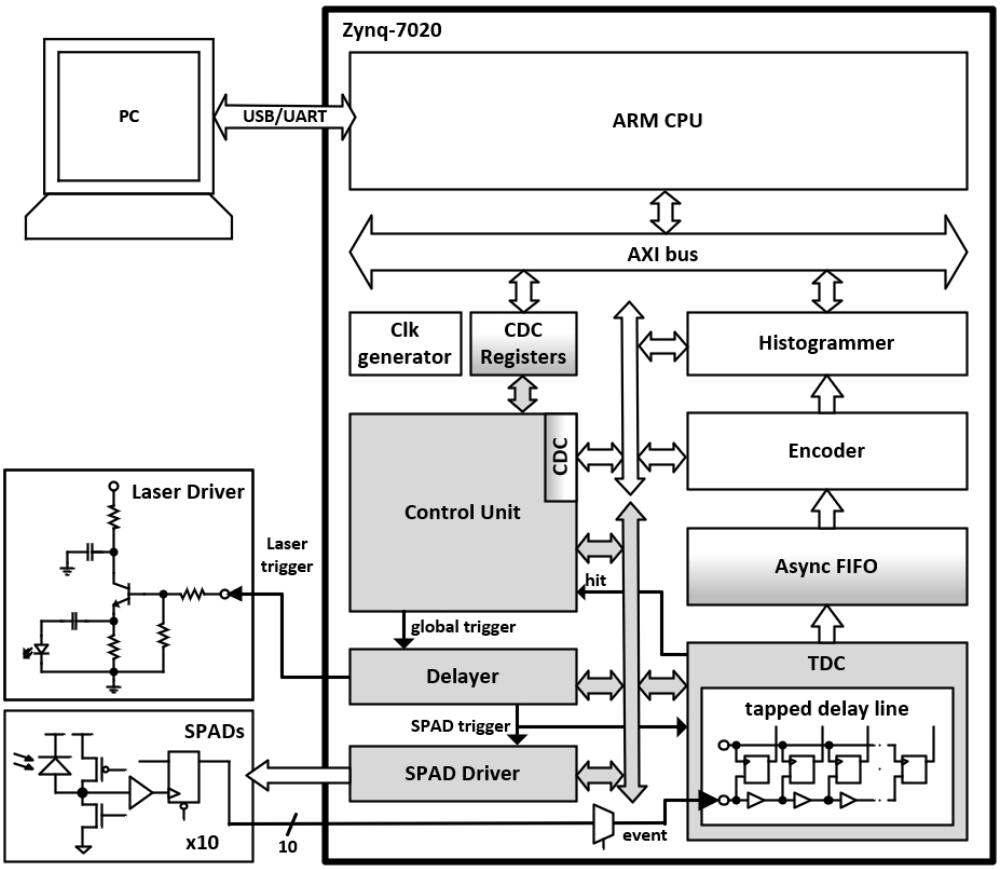

Figure 5.5 Architecture of the TCSPC system used with the pixel array with external timing circuit.

The system is a clock domain crossing based design. The communications with the ARM processor are through a Xilinx standard AXI bus that operates with 100 MHz clock. The TDC and the SPAD driver modules require a higher frequency to limit the delay line length, to generate a short reset for the SPADs sensor.

5.4.1.2 System Performance & Lifetime Estimations

For POC validation, two dilution experiments were performed with concentrations of 1 µM, 500 nM, 250 nM, 125 nM, 62.5 nM, and 31.25 nM were done. 500k excitation cycles were done to obtain each decay curve in less than a minute. The experiments were carried out with the SPAD sensor biased at 1.4 V of overvoltage. The dark count rate profile for the SPAD sensor chip used is shown in Figure 2.14.

A first experiment was done to determine the sensitivity of the system. The microchannel was positioned over the SPAD with lower noise to guarantee the best SNR. The results of the fluorescence decay measurements performed are shown in Figure 5.6. A PBS measurement without quantum dot was used as the IRF. A Savitzky-Golay digital filter [283] was applied to the PBS reference presented in Figure 5.6 for clarity in the representations.

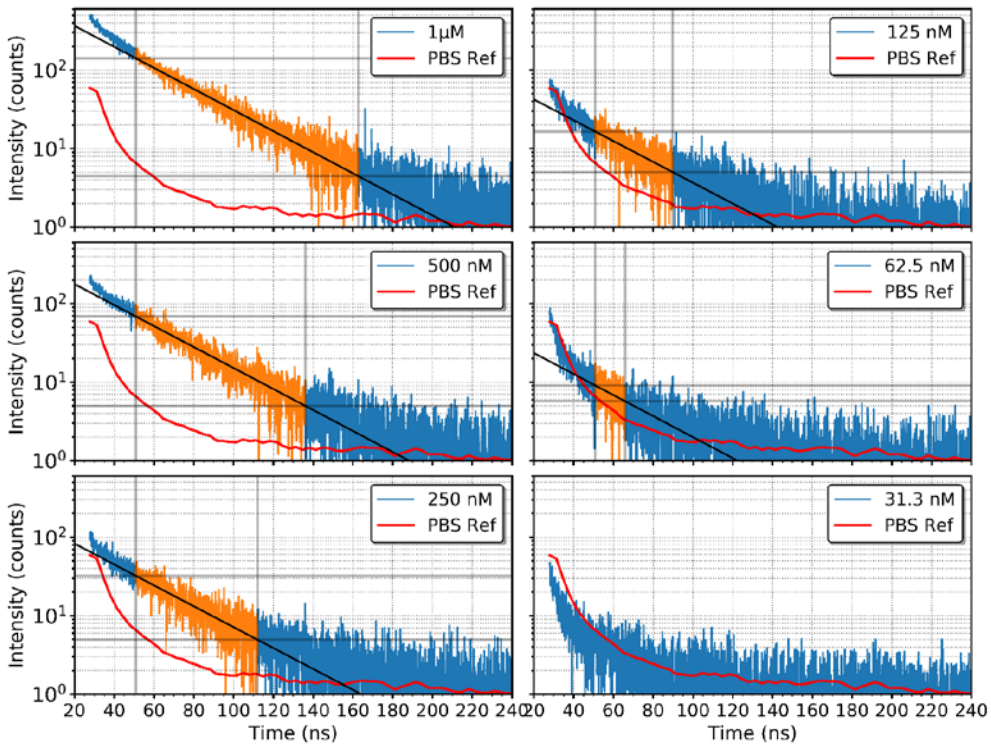

Figure 5.6 Fluorescence decay curves measured using the SPAD located below the microchannel for different concentrations of QDs, together with fitting lines used to determine the lifetimes for each concentration. The adjustment lines are calculated using only the points where the predominant effect is the decay of the QDs (highlighted in orange) [53].

As expected, the fluorescence intensity decreases with fluorophore concentration. For the 31.25 nM concentration, the decay curve is below the PBS reference because of the loses in the transmission path. The combination of the quantum efficiency, the scattered emission of the QDs and the absorption of the emitted photons by the neighbor QDs reduce the light reaching the active area of the SPAD below the reference. The other concentrations follow bi-exponential decay curves above the reference. These curves present three different regions, each one with its decay rate. At the beginning, from 20 to 50 ns, the decay curves present higher decay rates mainly because of the laser pulse tail, clearly visible at the beginning of the PBS curve. From the 50 ns mark, the fluorescence of QDs becomes the predominant effect. In this region (orange highlighted zones), the linear appearance of the logarithmic decay curves indicates that the fluorescence decay can be fitted to a mono-exponential decay, given by equation 1.1. Finally, at the end of the measuring period, the decay rate slows down as it reaches the noise level [53].

To extract the lifetime, we made a linear fit to the logarithmic representation of the intensity decays on the second region of each curve, setting the cut-off point of the fitted data at three times the noise level. The lifetime is then the inverse of the slope of the resulting line. Lifetimes of 32.4, 32.5, 32.6, 32.7, and 32.4 ns with a 500 ps of error were obtained for the QDs concentrations of 1 µM, 500, 250, 125, 62.5 nM, respectively. These lifetime estimations are in agreement with those in the literature, which varies from 30 to 40 ns [284, 285]. With this set of concentrations of QDs, the detection limit for our system is a concentration of 62.5 nM [53].

A second experiment was conducted to study the possibility of using a SPAD pixel regardless of the position of the microchannel, as well as to verify the feasibility of analyzing two or more samples labeled with the same fluorophore simultaneously using a multichannel microfluidic chip. For this purpose, we studied how the detected signal varies with the distance between the SPAD and the microchannel for different concentrations. We placed the microchannel over one of the pixels at the ends (labeled as SPAD0). Then the fluorescence intensity and lifetime detected along the SPAD array are measured, taking advantage that the SPAD pixels are linearly distributed and spaced 50 µm.

Figure 5.7 shows the detected fluorescence intensity by each SPAD for the different concentrations during the period in which the predominant contribution is the

QDs fluorescence, as well as the PBS reference. As expected, the intensity of the signal decreases with the distance between the microchannel and the sensor. The PBS reference measurements present a profile similar to the DCR of the array (Figure 2.14), setting the detection limit along the SPAD sensor array. The intensity level for the 31.25 nM sample was always below the PBS reference, as expected from the previous experiment. The 125 and 62.5 nM concentrations can be detected until the 6th SPAD situated at 300 µm from the sample. Higher concentrations were detected even with the noisiest SPAD of the array, number seven at 350 µm, which has eight times the noise of the best one [53].

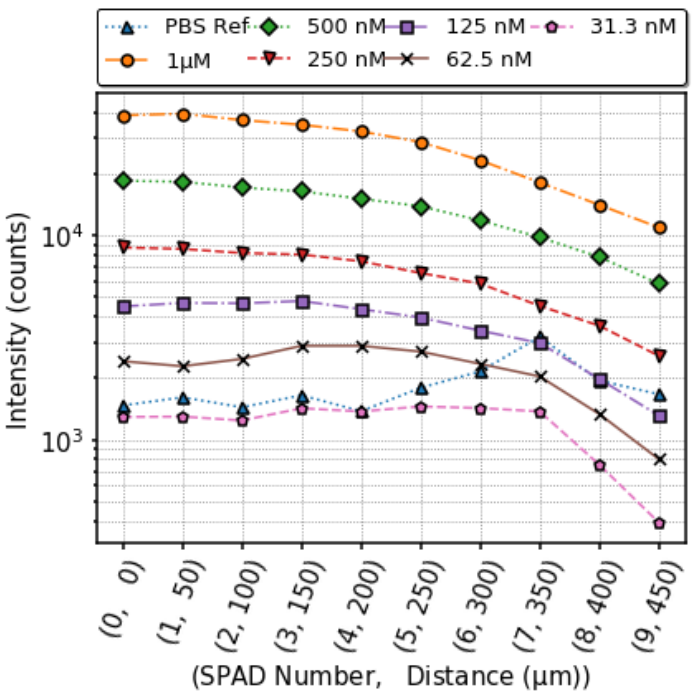

Figure 5.7 Fluorescence intensity measured across the SPAD array within the time slice 50–75 ns, showing how the level detected decreases with the distance [53].

Additionally, we calculated the quantum dot lifetime as done for the previous experiment for each concentration and SPAD along the array. Figure 5.8 shows the extracted lifetimes for the different concentrations. As expected, the lifetimes can be extracted only where the detected signal is over the PBS reference signal. The

extracted lifetimes were consistent with the previous results across the array, with an average lifetime of 32.7 ns with a standard deviation of 0.2 ns [53].

In view of the results, we conclude that the microchannel in this setup can be placed roughly over the SPAD array, with a tolerance of 300 microns. Within this range, it is possible to choose among the SPADs one with sufficient SNR to perform the fluorescence lifetime measurement of concentrations down to 62.5 nM. However, and for the same reason, it is not possible to define SPAD-microchannel pairs to analyze multiple samples labeled with the same fluorophore at the same time using a multichannel microfluidic chip.

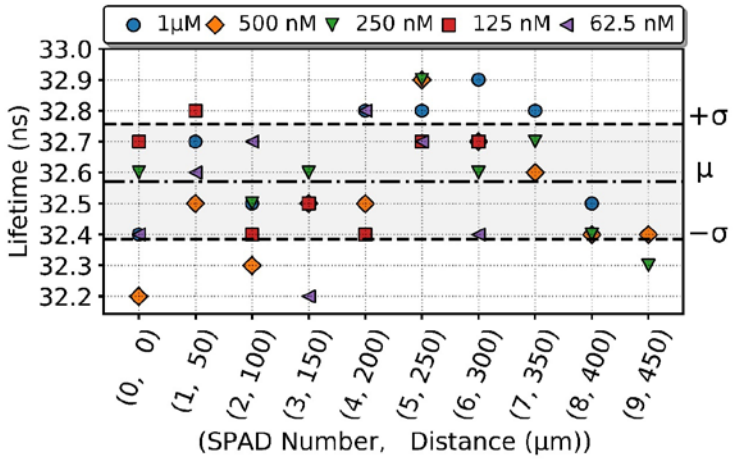

Figure 5.8 Fluorescent lifetimes of QDs extracted along the SPAD array for concentrations of 1 µM, 500, 250, 125, 62.5, and 31.25 nM, with the microchannel placed over the SPAD0. The lifetime estimation error is 500 ps [53].

5.4.2 POC Based on the Pixel Array with Analog Historgamming On-Chip

5.4.2.1 System Setup

In order to perform time-resolved fluorescence with the pixels with the histogramming on-chip circuit, one faster analog-to-digital converter (ADC) per analog channel (AD7274BRMZ, 12 b, 3 Msps) was implemented together with the bias circuits in the daughter card. Vbias and VBiasCI were generated via a serial-

peripheral-interface (SPI) bus with a digital-to-analog converter (DAC, MAX5715AAUD). Acquisitions were performed using the same Zynq-7020 AP SoC FPGA development board.

In this setup, due to the bin decay effects observed during the characterization of the histogramming circuit, the laser driving circuit used was the RF bipolar based because of its higher repetition rate (up to 77 MHz).

Figure 5.9 shows the architecture of the data acquisition system implemented in the Z-7020. The architecture is quite similar to the previous one (Figure 5.5), although the control is more straightforward since the histogram is built on-chip. The timing electronics is replaced by the ADCs controller, which captures the on-chip histogram bins values at the end of the measurement.

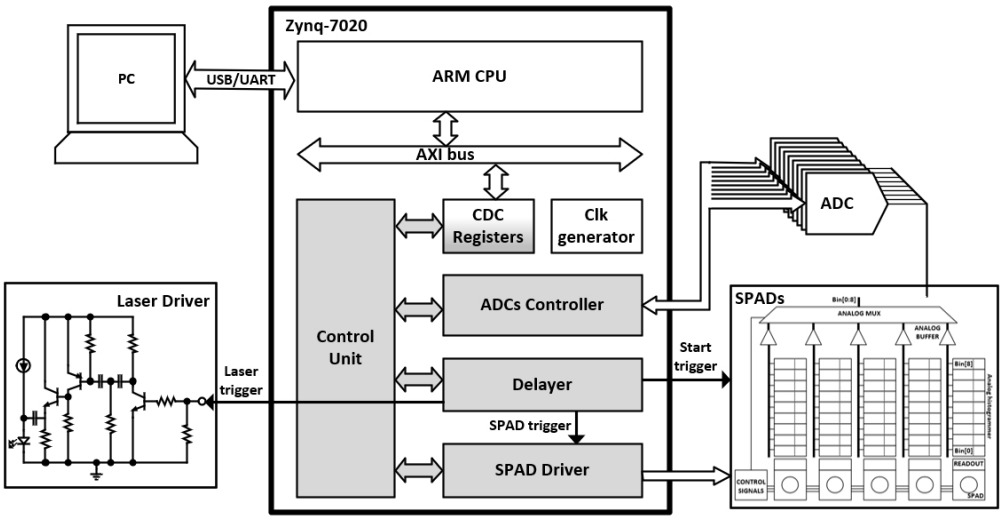

Figure 5.9 Architecture of the data acquisition system implemented to control the operation of the pixel array with analog histogramming on-chip.

5.4.2.2 Lifetime estimation

For the technology validation, 5000 excitation pulses with ton/toff equaling 30/20 ns were generated (total measurement time of 250 µs). Measurements were taken with Vbias = 900 mV, VbiasCI = 700 mV, and overvoltage of 1.4 V. The deviations due to mismatches were compensated off-chip by normalizing each bin voltage to a reference.

Figure 5.10 shows the measurements obtained for the different QD concentrations. For comparison, the TCSPC measurement of 1 µM of the QD is also presented. This measurement was taken with the POC based on the pixel array with external timing circuit. As can be observed, the two measurements for 1 µM of the QD were in perfect agreement. The decay time for all the QD concentrations was always the same, except for the 62.5 nM concentration that was impossible to fit due to a very low signal-to-noise ratio. The lifetime was estimated using the linear least-squares method for *N* bins [10] by,

$$\tau = \frac{N(\sum t_i^2) - (\sum t_i)^2}{N \sum t_i \, lnI_i - (\sum t_i)(lnI_i)} \tag{5.3}$$

where t_i and I_i are the time and intensity, respectively, of bin *I*.

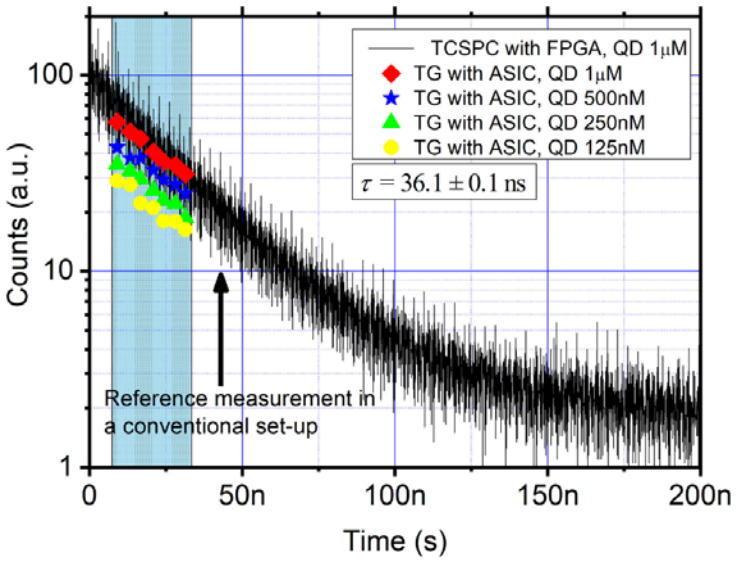

Figure 5.10 Fitting of the lifetimes of the different QD concentrations to a mono-exponential decay curve. The lifetime was ~36 ns. The results are compared with the TCSPC measurement of 1 µM of the QD [54].

By fitting the voltages measured in the different bins, we obtained a lifetime of 36.1 ± 0.1 ns, which was consistent with the previous results (32.7 ns), considering that the method implemented to measure them has losses [54]. Also, both QDs proceeded from different batches. However, the detection limit was higher than that reached with the first device, even using the same SPAD pixel structure. This

was due to the excitation pulses were less powerful (as discussed in Chapter 4) combined with the bin decay effect at low count rates described in Chapter 2.

5.5 Summary

In this chapter, two general-purpose platforms based on time-resolved fluorescence spectroscopy were implemented and validated. The first device integrates a custom 1-D 10 SPAD pixels array sensor and implements a complete TCSPC system in a Zynq-7020 AP SoC (from Xilinx). The system design takes the advantages of a linear array of CMOS SPAD-based detectors with a custom PDMS microfluidic cartridge that works with a coarse easy alignment. Moreover, the device avoids the need optical filters to remove the excitation light by beginning the measurement process after it has faded below the fluorescence, but that limits the fluorophores to those with long lifetimes, such as QDs. The SPAD makes it possible to detect low concentrations of fluorophores thanks to its sensitivity over a wide range of wavelengths [53].

The results show that the system was able to build the histogram of the fluorescence decay and measure the lifetime from very small sample volumes (20 nl) at practical concentration levels (62.5 nM) in a few seconds. Moreover, to the best of our knowledge, the 62.5 nM is the lowest reported concentration from which a low-cost instrument with neither optical lenses nor filters has extracted the fluorescence lifetime [53, 263, 286, 287].

The second version of the device implements a high integrated version of the SPAD pixel, which includes histogramming on-chip capabilities. The decay time of the QD was directly deduced by fitting the on-chip generated histogram to an exponential decay curve. We obtained a decay time of 36.1 ns, which is consistent with the values reported in the literature and with our results obtained using TCSPC. We were able to measure concentrations as low as 125 nM in a volume of 20 nanoliters [54].

The detection limit of both devices was given by the noise of the SPAD and the pulsed light source. It is clear that both implementations would benefit from several design improvements. The noise of the SPAD is relatively easy to overcome, either by cooling the device or by migrating to another technology with quiet

SPAD [135]. The technology migration would also allow increasing the active area of the SPADs improving the SNR even further. Another enhancement would be to use a laser diode with a shorter wavelength, thus increasing the QDs excitation efficiency (see Figure 4.1) at the expenses of the budget. A more reasonable solution would be to integrate a thin film bandpass filter over the CMOS sensor, which helps to reject the pulse tail allowing to reduce the time elapsed between the laser pulse and OW, and thereby increasing the intensity level. Alternatively, we can integrate a dedicated driver in a CMOS standard technology in order to go further in the miniaturization of the whole system such as Rae et al. reported in [57, 58]. Finally, another possibility to improve the detection limit would be to put the sample closer by using a thinner substrate to seal the microfluidic chip, such as a PDMS sealing membrane of 20 microns reported in [288].

Furthermore, the results indicate that the devices are not able to analyze different samples labeled with the same fluorophore simultaneously by means of the multiple-channel microfluidics. One possibility to explore in order to get around this problem would be to use different fluorophores on each channel, each one decaying according to a different lifetime, and fit a multi-exponential decay on the obtained curves [289]. Such an experiment requires fluorophores with long but different lifetimes and is out of the scope of the present work. An alternative to the multi-exponential decay analysis might be multiplexing the sample over time. This method consists in reusing the microchannel with different samples, cleaning it after each measurement. This presents two main drawbacks: the absorption of small molecules such as drugs and proteins on the PDMS surface, which has been identified as a major problem for molecular biology [290, 291], and the automation of the process, which requires the use of micro-pumps, increasing the complexity of the setup [31, 292]. However, our system builds on the advantages of the cheap single-use microfluidic cartridge to offer an elegant and useful solution. The sample can be changed without any alignment procedure, performing the measurement with all the SPADs, and analyzing the decay curve with the best SNR. Moreover, the use of commercial components combined with an ultra-sensitive detector and a removable microfluidic cartridge makes the two POC devices a low-cost system with great versatility, which holds large potential for applications in an analytical laboratory, clinical diagnosis, at the point-of-care, or in a resource-limited environment [53].

Future work should focus on bioassays to validate POC in real applications, detecting different biomarkers labeled with QDs, such as troponin I and troponin T as indicators of myocardial degradation and infarction [293], the procalcitonin in systemic bacterial infections and sepsis [294], or blood biomarkers (including proteins, ribonucleic acids, lipids or metabolites) for stroke diagnosis [295].

Chapter 6

Conclusions

Point-of-care (PoC) devices have become a major trend in the field of biomedical engineering, addressing clinical and environmental needs, such as diagnostics and in-field assays. The development of reliable and self-contained POC devices depends on the integration of the key technologies on an industrial scale, e.g., microelectronics with microfluidics, highly sensitive detection methods and low-cost materials for easy-to-use tools. Within the scope of this thesis, the integration of different techniques and microtechnologies to develop a POC device for medical diagnosis based on the fluorescence lifetime measurement has been presented.

In particular, the binomial consisting of the SPADs-based sensor chip and the microfluidics cartridge has been custom-made, optimizing the off-chip contact sensing, thus eliminating the traditional optical elements of these type of instruments. The high-level of integration achieved and the simplicity of the assembly allow the sample to be positioned directly over the sensor array (at less than 200 μm from the sensor chip surface) without any alignment procedure. In addition, the device implements the time gating technique, dispensing with filters to remove the excitation light from the measurement window. However, this limits the system to use fluorescence labels with long lifetimes such as QDs.

Finally, two versions of the system were implemented with different levels of integration. The first device integrates the 10 SPAD pixels array sensor and implements a complete TCSPC system in a Zynq-7020 AP SoC (from Xilinx) to measure and reconstruct the fluorescence decay profile with an average resolution of 68 ps. Instead, the second device integrates the 5 SPAD pixels with

histogramming on-chip capabilities, where the decay time of the QD was directly deduced by fitting the on-chip generated histogram to an exponential decay curve.

The results show that both systems were able to build the histogram of the fluorescence decay and measure the lifetime from very small sample volumes (20 nl) at practical concentration levels (62.5 nM and 125 nM for the off-chip and on-chip histogramming devices, respectively) in a few seconds. Nevertheless, the detection limit was determined by the noise of the SPAD and the optical pulse tail of the excitation light source, which can be easily improved by putting the sample closer by using a thinner substrate to seal the microfluidic chip, such as a PDMS sealing membrane 20 microns thick. Even with these limitations, the use of commercial components combined with a CMOS SPAD detector and a removable microfluidic cartridge makes the POC a low-cost system with great versatility, which holds large potential for applications in an analytical laboratory, clinical diagnosis, at the point-of-care, or in a resource-limited environment.

The path to the industrialization of this device was explored, involving the need to reduce size and cost. However, the PDMS seems to be the more limiting material for mass production and, after a critical review, a soft thermoplastic elastomer (e.g., Flexdym) appeared as the best alternative to PDMS. Beyond the context of this thesis, work will continue on the biomedical application of the device and the improvement of the detection limit.

Bibliography

[1] S. Deshayes and G. Divita, “Fluorescence technologies for monitoring interactions between biological molecules in vitro,” in *Progress in Molecular Biology and Translational Science*, vol. 113, Elsevier B.V., 2013, pp. 109–143, doi:10.1016/B978-0-12-386932-6.00004-1.

[2] Joseph R. Lakowicz, *Principles of Fluorescence Spectroscopy*, 3rd ed. New York: Springer, 2006, doi:10.1007/978-0-387-46312-4.

[3] R. M. Rich *et al.*, “Elimination of autofluorescence background from fluorescence tissue images by use of time-gated detection and the AzaDiOxaTriAngulenium (ADOTA) fluorophore,” *Anal. Bioanal. Chem.*, vol. 405, no. 6, pp. 2065–2075, 2013, doi:10.1007/s00216-012-6623-1.

[4] M. Grabolle, P. Kapusta, T. Nann, X. Shu, J. Ziegler, and U. Resch-Genger, “Fluorescence Lifetime Multiplexing with Nanocrystals and Organic Labels,” *Anal. Chem.*, vol. 81, no. 18, pp. 7807–7813, Sep. 2009, doi:10.1021/ac900934a.

[5] A. Boreham, R. Brodwolf, K. Walker, R. Haag, and U. Alexiev, “Time-Resolved Fluorescence Spectroscopy and Fluorescence Lifetime Imaging Microscopy for Characterization of Dendritic Polymer Nanoparticles and Applications in Nanomedicine,” *Molecules*, vol. 22, no. 1, p. 17, Dec. 2016, doi:10.3390/molecules22010017.

[6] L. Pires, M. S. Nogueira, S. Pratavieira, L. T. Moriyama, and C. Kurachi, “Time-resolved fluorescence lifetime for cutaneous melanoma detection,” *Biomed. Opt. Express*, vol. 5, no. 9, p. 3080, Sep. 2014.

[7] D. D.-U. Li *et al.*, “Time-Domain Fluorescence Lifetime Imaging Techniques Suitable for Solid-State Imaging Sensor Arrays,” *Sensors*, vol. 12, no. 5, pp. 5650–5669, May 2012, doi:10.3390/s120505650.

[8] L. Marcu, P. M. W. French, and D. S. Elson, *FLUORESCENCE LIFETIME SPECTROSCOPY AND IMAGING:: Principles and Applications in Biomedical Diagnostics*, 1st ed. Boca Raton: CRC Press., 2014, doi:https://doi.org/10.1201/b17018.

[9] T. Salthammer, “Numerical simulation of pile-up distorted time-correlated single photon counting (TCSPC) data,” *J. Fluoresc.*, vol. 2, no. 1, pp. 23–27, Mar. 1992, doi:10.1007/BF00866385.

[10] C. W. Chang, D. Sud, and M. A. Mycek, “Fluorescence Lifetime Imaging

Microscopy," *Methods in Cell Biology*, vol. 81. pp. 495–524, 2007.

[11] R. M. Ballew and J. N. Demas, "An error analysis of the rapid lifetime determination method for the evaluation of single exponential decays," *Anal. Chem.*, vol. 61, no. 1, pp. 30–33, May 2002, doi:10.1021/ac00176a007.

[12] W. Becker, *Advanced Time-Correlated Single Photon Counting Techniques*. Berlin: Springer, 2005, doi:10.1007/3-540-28882-1.

[13] PicoQuant, "MicroTime 100." [Online]. Available: https://www.picoquant.com/products/category/fluorescence-microscopes/microtime-100-upright-time-resolved-fluorescence-microscope. [Accessed: 05-Jul-2018].

[14] HORIBA Scientific, "DeltaPro^{TM}Lifetime System." [Online]. Available: https://www.horiba.com/en_en/products/detail/action/show/Product/deltapro-1584/. [Accessed: 05-Jul-2019].

[15] K.-M. Lei, P.-I. Mak, M.-K. Law, and R. P. Martins, "CMOS biosensors for in vitro diagnosis - transducing mechanisms and applications," *Lab Chip*, vol. 16, no. 19, pp. 3664–3681, 2016, doi:10.1039/c6lc01002d.

[16] E. Charbon, "Single-photon imaging in complementary metal oxide semiconductor processes," *Philos. Trans. R. Soc. A Math. Phys. Eng. Sci.*, vol. 372, no. 2012, p. 20130100, Mar. 2014, doi:10.1098/rsta.2013.0100.

[17] D. Bronzi, F. Villa, S. Tisa, A. Tosi, and F. Zappa, "SPAD Figures of Merit for Photon-Counting, Photon-Timing, and Imaging Applications: A Review," *IEEE Sens. J.*, vol. 16, no. 1, pp. 3–12, Jan. 2016, doi:10.1109/JSEN.2015.2483565.

[18] C. Bruschini, H. Homulle, and E. Charbon, "Ten years of biophotonics single-photon SPAD imager applications: retrospective and outlook," 2017, vol. 10069, p. 100691S, doi:10.1117/12.2256247.

[19] N. A. W. Dutton, L. Parmesan, A. J. Holmes, L. A. Grant, and R. K. Henderson, "320x240 oversampled digital single photon counting image sensor," in *2014 Symposium on VLSI Circuits Digest of Technical Papers*, 2014, pp. 1–2, doi:10.1109/VLSIC.2014.6858428.

[20] M. J. Hsu, S. C. Esener, and H. Finkelstein, "A CMOS STI-Bound Single-Photon Avalanche Diode With 27-ps Timing Resolution and a Reduced Diffusion Tail," *IEEE Electron Device Lett.*, vol. 30, no. 6, pp. 641–643, Jun. 2009, doi:10.1109/LED.2009.2019974.

[21] D. Tyndall *et al.*, "A High-Throughput Time-Resolved Mini-Silicon Photomultiplier With Embedded Fluorescence Lifetime Estimation in 0.13 µm CMOS," *IEEE Trans. Biomed. Circuits Syst.*, vol. 6, no. 6, pp. 562–570, Dec. 2012, doi:10.1109/TBCAS.2012.2222639.

[22] J. Byungchul, C. Peiyan, A. Chevalier, A. Ellington, and A. Hassibi, "A CMOS fluorescent-based biosensor microarray," in *2009 IEEE International Solid-State Circuits Conference - Digest of Technical Papers*, 2009, pp. 436-437,437a, doi:10.1109/ISSCC.2009.4977495.

[23] R. Singh, A. Manickam, and A. Hassibi, "CMOS biochips for hypothesis-driven DNA analysis," in *2014 IEEE Biomedical Circuits and Systems Conference (BioCAS) Proceedings*, 2014, pp. 484–487, doi:10.1109/BioCAS.2014.6981768.

[24] G. Giraud *et al.*, "Fluorescence lifetime biosensing with DNA microarrays and a CMOS-SPAD imager," *Biomed. Opt. Express*, vol. 1, no. 5, p. 1302, Dec. 2010, doi:10.1364/BOE.1.001302.

[25] T. D. Huang *et al.*, "Gene expression analysis with an integrated CMOS microarray by time-resolved fluorescence detection," *Biosens. Bioelectron.*, vol. 26, no. 5, pp. 2660–2665, Jan. 2011, doi:10.1016/J.BIOS.2010.03.001.

[26] N. Guo, K. W. Cheung, H. Wong, and D. Ho, "CMOS Time-Resolved, Contact, and Multispectral Fluorescence Imaging for DNA Molecular Diagnostics," *Sensors*, vol. 14, no. 11, pp. 20602–20619, Oct. 2014, doi:10.3390/s141120602.

[27] H. Norian, R. M. Field, I. Kymissis, and K. L. Shepard, "An integrated CMOS quantitative-polymerase-chain-reaction lab-on-chip for point-of-care diagnostics," *Lab Chip*, vol. 14, no. 20, pp. 4076–4084, 2014, doi:10.1039/c4lc00443d.

[28] M. C. Pierce, S. E. Weigum, J. M. Jaslove, R. Richards-Kortum, and T. S. Tkaczyk, "Optical Systems for Point-of-care Diagnostic Instrumentation: Analysis of Imaging Performance and Cost," *Ann. Biomed. Eng.*, vol. 42, no. 1, pp. 231–240, Jan. 2014, doi:10.1007/s10439-013-0918-z.

[29] A. Forcucci, M. E. Pawlowski, Z. Crannell, I. Pavlova, R. Richards-Kortum, and T. S. Tkaczyk, "All-plastic miniature fluorescence microscope for point-of-care readout of bead-based bioassays," *J. Biomed. Opt.*, vol. 20, no. 10, p. 105010, Oct. 2015, doi:10.1117/1.JBO.20.10.105010.

[30] S. Camou, H. Fujita, and T. Fujii, "PDMS 2D optical lens integrated with microfluidic channels: principle and characterization," *Lab Chip*, vol. 3, no. 1, p. 40, 2003, doi:10.1039/b211280a.

[31] J. M. Emory *et al.*, "Design and development of a field-deployable single-molecule detector (SMD) for the analysis of molecular markers," *Analyst*, vol. 137, no. 1, pp. 87–97, 2012, doi:10.1039/c1an15658f.

[32] J. Seo and L. P. Lee, "Disposable integrated microfluidics with self-aligned planar microlenses," *Sensors Actuators B Chem.*, vol. 99, no. 2–3, pp. 615–

622, May 2004, doi:10.1016/j.snb.2003.11.014.

[33] J. Lim, P. Gruner, M. Konrad, and J.-C. Baret, "Micro-optical lens array for fluorescence detection in droplet-based microfluidics," *Lab Chip*, vol. 13, no. 8, pp. 1472–1475, 2013, doi:10.1039/c3lc41329b.

[34] J.-C. Roulet, R. Völkel, H. P. Herzig, E. Verpoorte, Rooij. Nico F., and R. Dändliker, "Microlens systems for fluorescence detection in chemical microsystems," *Opt. Eng.*, vol. 40, no. 5, p. 814, May 2001, doi:10.1117/1.1359522.

[35] H. Zhu, S. Mavandadi, A. F. Coskun, O. Yaglidere, and A. Ozcan, "Optofluidic Fluorescent Imaging Cytometry on a Cell Phone," *Anal. Chem.*, vol. 83, no. 17, pp. 6641–6647, Sep. 2011, doi:10.1021/ac201587a.

[36] O. Schmidt, M. Bassler, P. Kiesel, C. Knollenberg, and N. Johnson, "Fluorescence spectrometer-on-a-fluidic-chip," *Lab Chip*, vol. 7, no. 5, p. 626, May 2007, doi:10.1039/b618879f.

[37] R. J. Ram and K. Lee, "Optical waveguides for microfluidic integration," in *2009 IEEE LEOS Annual Meeting Conference Proceedings*, 2009, pp. 371–372, doi:10.1109/LEOS.2009.5343106.

[38] B. Kuswandi, Nuriman, J. Huskens, and W. Verboom, "Optical sensing systems for microfluidic devices: A review," *Anal. Chim. Acta*, vol. 601, no. 2, pp. 141–155, Oct. 2007, doi:10.1016/j.aca.2007.08.046.

[39] N. Pires, T. Dong, U. Hanke, and N. Hoivik, "Recent Developments in Optical Detection Technologies in Lab-on-a-Chip Devices for Biosensing Applications," *Sensors*, vol. 14, no. 8, pp. 15458–15479, Aug. 2014, doi:10.3390/s140815458.

[40] H. Yang and M. A. M. Gijs, "Micro-optics for microfluidic analytical applications," *Chem. Soc. Rev.*, vol. 47, no. 4, pp. 1391–1458, Feb. 2018, doi:10.1039/C5CS00649J.

[41] J.-C. Roulet, R. Völkel, H. P. Herzig, E. Verpoorte, N. F. de Rooij, and R. Dändliker, "Performance of an Integrated Microoptical System for Fluorescence Detection in Microfluidic Systems," *Anal. Chem.*, vol. 74, no. 14, pp. 3400–3407, Jul. 2002, doi:10.1021/ac0112465.

[42] S. Moon *et al.*, "Integrating microfluidics and lensless imaging for point-of-care testing," *Biosens. Bioelectron.*, vol. 24, no. 11, pp. 3208–3214, Jul. 2009, doi:10.1016/J.BIOS.2009.03.037.

[43] U. A. Gurkan *et al.*, "Miniaturized lensless imaging systems for cell and microorganism visualization in point-of-care testing," *Biotechnol. J.*, vol. 6, no. 2, pp. 138–149, Feb. 2011, doi:10.1002/biot.201000427.

[44] H. Takehara *et al.*, "On-chip cell analysis platform: Implementation of contact fluorescence microscopy in microfluidic chips," *AIP Adv.*, vol. 7,

no. 9, p. 095213, Sep. 2017, doi:10.1063/1.4986872.

[45] M. L. Adams, M. Enzelberger, S. Quake, and A. Scherer, "Microfluidic integration on detector arrays for absorption and fluorescence micro-spectrometers," *Sensors Actuators A Phys.*, vol. 104, no. 1, pp. 25–31, Mar. 2003, doi:10.1016/S0924-4247(02)00477-6.

[46] D. Ho, M. O. Noor, U. J. Krull, G. Gulak, and R. Genov, "CMOS Spectrally-Multiplexed FRET-on-a-Chip for DNA Analysis," *IEEE Trans. Biomed. Circuits Syst.*, vol. 7, no. 5, pp. 643–654, Oct. 2013, doi:10.1109/TBCAS.2012.2230172.

[47] H. A. McLeod, *Thin-Film Optical Filters*, 3rd ed. London: Institute of Physics, 2001.

[48] W. Li, T. Knoll, A. Sossalla, H. Bueth, and H. Thielecke, "On-chip integrated lensless fluorescence microscopy/spectroscopy module for cell-based sensors," 2011, vol. 7894, p. 78940Q, doi:10.1117/12.875417.

[49] A. F. Coskun, T.-W. Su, and A. Ozcan, "Wide field-of-view lens-free fluorescent imaging on a chip," *Lab Chip*, vol. 10, no. 7, p. 824, Apr. 2010, doi:10.1039/b926561a.

[50] Y. Maruyama and E. Charbon, "An all-digital, time-gated 128X128 spad array for on-chip, filter-less fluorescence detection," in *2011 16th International Solid-State Sensors, Actuators and Microsystems Conference*, 2011, pp. 1180–1183, doi:10.1109/TRANSDUCERS.2011.5969324.

[51] D. Stoppa, D. Mosconi, L. Pancheri, and L. Gonzo, "Single-Photon Avalanche Diode CMOS Sensor for Time-Resolved Fluorescence Measurements," *IEEE Sens. J.*, vol. 9, no. 9, pp. 1084–1090, Sep. 2009, doi:10.1109/JSEN.2009.2025581.

[52] T. D. Huang, S. Sorgenfrei, P. Gong, R. Levicky, and K. L. Shepard, "A 0.18-µm CMOS Array Sensor for Integrated Time-Resolved Fluorescence Detection," *IEEE J. Solid-State Circuits*, vol. 44, no. 5, pp. 1644–1654, May 2009, doi:10.1109/JSSC.2009.2016994.

[53] J. Canals, N. Franch, O. Alonso, A. Vilà, and A. Diéguez, "A Point-of-Care Device for Molecular Diagnosis Based on CMOS SPAD Detectors with Integrated Microfluidics," *Sensors*, vol. 19, no. 3, p. 445, Jan. 2019, doi:10.3390/s19030445.

[54] A. Dieguez, J. Canals, N. Franch, J. Dieguez, O. Alonso, and A. Vila, "A Compact Analog Histogramming SPAD-Based CMOS Chip for Time-Resolved Fluorescence," *IEEE Trans. Biomed. Circuits Syst.*, vol. 13, no. 2, pp. 343–351, Apr. 2019, doi:10.1109/TBCAS.2019.2892825.

[55] T. Araki and H. Misawa, "Light emitting diode-based nanosecond ultraviolet light source for fluorescence lifetime measurements," *Rev. Sci.*

Instrum., vol. 66, no. 12, pp. 5469–5472, Dec. 1995, doi:10.1063/1.1146519.

[56] C. Griffin *et al.*, "Fluorescence excitation and lifetime measurements using GaN/InGaN micro-LED arrays," in *The 17th Annual Meeting of the IEEELasers and Electro-Optics Society, 2004. LEOS 2004.*, 2004, vol. 2, pp. 896–897, doi:10.1109/LEOS.2004.1363531.

[57] B. R. Rae *et al.*, "A Vertically Integrated CMOS Microsystem for Time-Resolved Fluorescence Analysis," *IEEE Trans. Biomed. Circuits Syst.*, vol. 4, no. 6, pp. 437–444, Dec. 2010, doi:10.1109/TBCAS.2010.2077290.

[58] B. R. Rae *et al.*, "CMOS driven micro-pixel LEDs integrated with single photon avalanche diodes for time resolved fluorescence measurements," *J. Phys. D. Appl. Phys.*, vol. 41, no. 9, p. 094011, May 2008, doi:10.1088/0022-3727/41/9/094011.

[59] S. C. Jakeway, A. J. De Mello, and E. L. Russell, "Miniaturized total analysis systems for biological analysis," *Fresenius' Journal of Analytical Chemistry*, vol. 366, no. 6–7. pp. 525–539, 2000.

[60] R. C. McGlennen, "Miniaturization Technologies for Molecular Diagnostics," *Clin. Chem.*, vol. 47, no. 3, p. 393, Mar. 2001.

[61] A. J. Gawron, R. S. Martin, and S. M. Lunte, "Microchip electrophoretic separation systems for biomedical and pharmaceutical analysis," *European Journal of Pharmaceutical Sciences*, vol. 14, no. 1. pp. 1–12, 2001.

[62] U. Bilitewski, M. Genrich, S. Kadow, and G. Mersal, "Biochemical analysis with microfluidic systems," *Analytical and Bioanalytical Chemistry*, vol. 377, no. 3. pp. 556–569, Oct-2003.

[63] C. D. Chin, S. Y. Chin, T. Laksanasopin, and S. K. Sia, "Low-Cost Microdevices for Point-of-Care Testing," in *Point-of-Care Diagnostics on a Chip*, D. Issadore and R. M. Westervelt, Eds. Berlin, Heidelberg: Springer, 2013, doi:https://doi.org/10.1007/978-3-642-29268-2_1.

[64] E. Primiceri *et al.*, "Key Enabling Technologies for Point-of-Care Diagnostics," *Sensors*, vol. 18, no. 11, p. 3607, Oct. 2018, doi:10.3390/s18113607.

[65] H. Nakazato, H. Kawaguchi, A. Iwabuchi, and K. Hane, "Integrated fluorescent analysis system with monolithic GaN light emitting diode on Si platform," in *2012 IEEE 25th International Conference on Micro Electro Mechanical Systems (MEMS)*, 2012, pp. 842–845, doi:10.1109/MEMSYS.2012.6170317.

[66] L. Wei, Y. Tian, W. Yan, K. Cheung, and D. Ho, "Liquid-core waveguide TCSPC sensor for high-accuracy fluorescence lifetime analysis," *Anal. Bioanal. Chem.*, vol. 411, no. 16, pp. 3641–3652, Jun. 2019, doi:10.1007/s00216-019-01847-6.

[67] R. M. Field, S. Realov, and K. L. Shepard, "A 100 fps, time-correlated single-photon-counting-based fluorescence-lifetime imager in 130 nm CMOS," *IEEE J. Solid-State Circuits*, vol. 49, no. 4, pp. 867–880, 2014, doi:10.1109/JSSC.2013.2293777.

[68] A. G. Crevillén, M. Hervás, M. A. López, M. C. González, and A. Escarpa, "Real sample analysis on microfluidic devices," *Talanta*, vol. 74, no. 3. Elsevier, pp. 342–357, 15-Dec-2007.

[69] B. Della Ventura *et al.*, "Biosensor for Point-of-Care Analysis of Immunoglobulins in Urine by Metal Enhanced Fluorescence from Gold Nanoparticles," *ACS Appl. Mater. Interfaces*, vol. 11, no. 4, pp. 3753–3762, Jan. 2019, doi:10.1021/acsami.8b20501.

[70] W. S. Mielczarek, E. A. Obaje, T. T. Bachmann, and M. Kersaudy-Kerhoas, "Microfluidic blood plasma separation for medical diagnostics: Is it worth it?," *Lab Chip*, vol. 16, no. 18, pp. 3441–3448, 2016, doi:10.1039/c6lc00833j.

[71] C. Dincer, R. Bruch, A. Kling, P. S. Dittrich, and G. A. Urban, "Multiplexed Point-of-Care Testing – xPOCT," *Trends in Biotechnology*, vol. 35, no. 8. Elsevier Ltd, pp. 728–742, 01-Aug-2017.

[72] A. M. Foudeh, T. Fatanat Didar, T. Veres, and M. Tabrizian, "Microfluidic designs and techniques using lab-on-a-chip devices for pathogen detection for point-of-care diagnostics," *Lab on a Chip*, vol. 12, no. 18. Royal Society of Chemistry, pp. 3249–3266, 21-Sep-2012.

[73] P. Yager, G. J. Domingo, and J. Gerdes, "Point-of-Care Diagnostics for Global Health," 2008, doi:10.1146/annurev.bioeng.10.061807.160524.

[74] D. Issadore and R. M. Westervelt, Eds., *Point-of-Care Diagnostics on a Chip*. Berlin, Heidelberg: Springer, 2013, doi:10.1007/978-3-642-29268-2.

[75] C. D. Chin, V. Linder, and S. K. Sia, "Lab-on-a-chip devices for global health: Past studies and future opportunities," *Lab on a Chip*, vol. 7, no. 1. Royal Society of Chemistry, pp. 41–57, 2007.

[76] P. B. Luppa and R. Junker, *Point-of-care testing: Principles and clinical applications*. Springer Berlin Heidelberg, 2018, doi:10.1007/978-3-662-54497-6.

[77] P. Floriano, *Microchip-Based Assay Systems*, vol. 385. 2007, doi:10.1007/978-1-59745-426-1.

[78] K. Baryeh, S. Takalkar, M. Lund, and G. Liu, "Introduction to medical biosensors for point of care applications," in *Medical Biosensors for Point of Care (POC) Applications*, Elsevier Inc., 2017, pp. 3–25, doi:10.1016/B978-0-08-100072-4.00001-0.

[79] M. Azhar and D. Dendukuri, “Microfluidic platforms for point of care (POC) medical diagnostics,” in *Medical Biosensors for Point of Care (POC) Applications*, Elsevier Inc., 2017, pp. 255–273, doi:10.1016/B978-0-08-100072-4.00011-3.

[80] T. R. Kozel and A. R. Burnham-Marusich, “Point-of-care testing for infectious diseases: Past, present, and future,” *Journal of Clinical Microbiology*, vol. 55, no. 8. American Society for Microbiology, pp. 2313–2320, 01-Aug-2017.

[81] P. B. Luppa, A. Bietenbeck, C. Beaudoin, and A. Giannetti, “Clinically relevant analytical techniques, organizational concepts for application and future perspectives of point-of-care testing,” *Biotechnology Advances*, vol. 34, no. 3. Elsevier Inc., pp. 139–160, 01-May-2016.

[82] R. Banerjee and A. Jaiswal, “Recent advances in nanoparticle-based lateral flow immunoassay as a point-of-care diagnostic tool for infectious agents and diseases,” *Analyst*, vol. 143, no. 9. Royal Society of Chemistry, pp. 1970–1996, 07-May-2018.

[83] K. Mitsakakis, V. D’Acremont, S. Hin, F. von Stetten, and R. Zengerle, “Diagnostic tools for tackling febrile illness and enhancing patient management,” *Microelectron. Eng.*, vol. 201, pp. 26–59, Dec. 2018, doi:10.1016/j.mee.2018.10.001.

[84] B. Hayes, C. Murphy, A. Crawley, and R. O’Kennedy, “Developments in Point-of-Care Diagnostic Technology for Cancer Detection,” *Diagnostics*, vol. 8, no. 2, p. 39, Jun. 2018, doi:10.3390/diagnostics8020039.

[85] P. B. Luppa, C. Müller, A. Schlichtiger, and H. Schlebusch, “Point-of-care testing (POCT): Current techniques and future perspectives,” *TrAC - Trends in Analytical Chemistry*, vol. 30, no. 6. pp. 887–898, Jun-2011.

[86] A. H. Khan, S. Shakeel, K. Hooda, K. Siddiqui, and L. Jafri, “Best Practices in the Implementation of a Point of Care Testing Program: Experience From a Tertiary Care Hospital in a Developing Country,” *EJIFCC*, vol. 30, no. 3, pp. 288–302, Oct. 2019.

[87] C. P. Price and A. St John, “The value proposition for point-of-care testing in healthcare: HbA1c for monitoring in diabetes management as an exemplar,” *Scand. J. Clin. Lab. Invest.*, vol. 79, no. 5, pp. 298–304, Jul. 2019, doi:10.1080/00365513.2019.1614211.

[88] F. L. Kiechle and R. I. Main, “Blood Glucose: Measurement in the Point-of-Care Setting,” *Lab. Med.*, vol. 31, no. 5, pp. 276–282, May 2000, doi:10.1309/4BF1-ET6T-WFE3-M7XA.

[89] “i-STAT System | Abbott Point of Care.” [Online]. Available: https://www.pointofcare.abbott/int/en/offerings/istat. [Accessed: 08-Dec-2019].

[90] M. Shibasaki, T. Ibuki, and Y. Tanaka, "A portable blood analyzer that uses on-line data management to deliver higher-quality patient information," *J. Anesth.*, vol. 24, no. 4, pp. 643–645, Aug. 2010, doi:10.1007/s00540-010-0933-2.

[91] Stat-Dx, "DiagCORE Analyzer (Modular syndromic testing system)." [Online]. Available: https://www.stat-dx.com/solutions/diagcore-analyzer/. [Accessed: 08-Dec-2019].

[92] M. Parcina, R. Jozić, P. Ciorba, R. Schmithausen, I. Hannet, and J. Pareja, "Evaluation of the performance of direct nasopharyngeal swabs for acute respiratory syndrome molecular diagnostics by the highly multiplex STAT-Dx Respiratory System," in *28th European Congress of Clinical Microbiology and Infectious Diseases*, 2018.

[93] G. Lisby, I. Hannet, J. Pareja, and U. V. Schneider, "Evaluation of the performance of direct stool and rectal swabs for molecular diagnostics of infective gastroenteritis by the highly multiplexed Stat-Dx gastrointestinal system," in *28th European Congress of Clinical Microbiology and Infectious Diseases*, 2018.

[94] T. M. H. Lee and I. M. Hsing, "DNA-based bioanalytical microsystems for handheld device applications," *Analytica Chimica Acta*, vol. 556, no. 1. pp. 26–37, 18-Jan-2006.

[95] L. Chen, A. Manz, and P. J. R. Day, "Total nucleic acid analysis integrated on microfluidic devices," *Lab on a Chip*, vol. 7, no. 11. Royal Society of Chemistry, pp. 1413–1423, 2007.

[96] I. A. Darwish, "Immunoassay Methods and their Applications in Pharmaceutical Analysis: Basic Methodology and Recent Advances.," *Int. J. Biomed. Sci.*, vol. 2, no. 3, pp. 217–35, Sep. 2006.

[97] O. Pashchenko, T. Shelby, T. Banerjee, and S. Santra, "A Comparison of Optical, Electrochemical, Magnetic, and Colorimetric Point-of-Care Biosensors for Infectious Disease Diagnosis," *ACS Infectious Diseases*, vol. 4, no. 8. American Chemical Society, pp. 1162–1178, 10-Aug-2018.

[98] S. Nayak, N. R. Blumenfeld, T. Laksanasopin, and S. K. Sia, "Point-of-Care Diagnostics: Recent Developments in a Connected Age," *Anal. Chem.*, vol. 89, no. 1, pp. 102–123, Jan. 2017, doi:10.1021/acs.analchem.6b04630.

[99] C. Dincer, "Electrochemical microfluidic multiplexed biosensor platform for point-of-care testing," University of Freiburg, 2016doi:10.6094/UNIFR/11053.

[100] D. Quesada-González and A. Merkoçi, "Nanoparticle-based lateral flow biosensors," *Biosensors and Bioelectronics*, vol. 73. Elsevier Ltd, pp. 47–63, 05-Nov-2015.

[101] K. M. Koczula and A. Gallotta, “Lateral flow assays,” *Essays Biochem.*, vol. 60, no. 1, pp. 111–120, Jun. 2016, doi:10.1042/EBC20150012.

[102] J. Ansell, “Point-of-care patient self-monitoring of oral vitamin K antagonist therapy,” in *Journal of Thrombosis and Thrombolysis*, 2013, vol. 35, no. 3, pp. 339–341, doi:10.1007/s11239-013-0878-z.

[103] A. Niemz, T. M. Ferguson, and D. S. Boyle, “Point-of-care nucleic acid testing for infectious diseases,” *Trends in Biotechnology*, vol. 29, no. 5. pp. 240–250, May-2011.

[104] S. C. Andras, M. R. Davey, J. B. Power, and E. C. Cocking, “Strategies for signal amplification in nucleic acid detection,” *Applied Biochemistry and Biotechnology - Part B Molecular Biotechnology*, vol. 19, no. 1. pp. 29–44, 2001.

[105] P. Craw and W. Balachandran, “Isothermal nucleic acid amplification technologies for point-of-care diagnostics: A critical review,” *Lab on a Chip*, vol. 12, no. 14. Royal Society of Chemistry, pp. 2469–2486, 21-Jul-2012.

[106] S. M. Sze and K. N. Kwok, *Physics of semiconductor devices*, 3rd ed. Hoboken, New Jersey: John Wiley & Sons, Inc., 2006, doi:10.1002/0470068329.

[107] A. Rochas *et al.*, “Single photon detector fabricated in a complementary metal–oxide–semiconductor high-voltage technology,” *Rev. Sci. Instrum.*, vol. 74, no. 7, pp. 3263–3270, Jul. 2003, doi:10.1063/1.1584083.

[108] M.-J. Lee, H. Rucker, and W.-Y. Choi, “Effects of Guard-Ring Structures on the Performance of Silicon Avalanche Photodetectors Fabricated With Standard CMOS Technology,” *IEEE Electron Device Lett.*, vol. 33, no. 1, pp. 80–82, Jan. 2012, doi:10.1109/LED.2011.2172390.

[109] C. Niclass, A. Rochas, P.-A. Besse, and E. Charbon, “Toward a 3-D Camera Based on Single Photon Avalanche Diodes,” *IEEE J. Sel. Top. Quantum Electron.*, vol. 10, no. 4, pp. 796–802, Jul. 2004, doi:10.1109/JSTQE.2004.833886.

[110] I. Nissinen *et al.*, “A sub-ns time-gated CMOS single photon avalanche diode detector for Raman spectroscopy,” in *2011 Proceedings of the European Solid-State Device Research Conference (ESSDERC)*, 2011, pp. 375–378, doi:10.1109/ESSDERC.2011.6044156.

[111] C. Niclass, M. Soga, H. Matsubara, S. Kato, and M. Kagami, “A 100-m Range 10-Frame/s 340x96-Pixel Time-of-Flight Depth Sensor in 0.18µm CMOS,” *IEEE J. Solid-State Circuits*, vol. 48, no. 2, pp. 559–572, Feb. 2013, doi:10.1109/JSSC.2012.2227607.

[112] L. Pancheri and D. Stoppa, “Low-noise single Photon Avalanche Diodes in 0.15 µm CMOS technology,” in *2011 Proceedings of the European*

Solid-State Device Research Conference (ESSDERC), 2011, pp. 179–182, doi:10.1109/ESSDERC.2011.6044205.

[113] D. Stoppa, L. Pancheri, M. Scandiuzzo, L. Gonzo, G.-F. Dalla Betta, and A. Simoni, "A CMOS 3-D Imager Based on Single Photon Avalanche Diode," *IEEE Trans. Circuits Syst. I Regul. Pap.*, vol. 54, no. 1, pp. 4–12, Jan. 2007, doi:10.1109/TCSI.2006.888679.

[114] S. Tisa, F. Zappa, and I. Labanca, "On-chip detection and counting of single-photons," in *IEEE InternationalElectron Devices Meeting, 2005. IEDM Technical Digest.*, pp. 815–818, doi:10.1109/IEDM.2005.1609480.

[115] C. Niclass, A. Rochas, P.-A. Besse, and E. Charbon, "Design and characterization of a CMOS 3-D image sensor based on single photon avalanche diodes," *IEEE J. Solid-State Circuits*, vol. 40, no. 9, pp. 1847–1854, Sep. 2005, doi:10.1109/JSSC.2005.848173.

[116] S. Cova, M. Ghioni, A. Lacaita, C. Samori, and F. Zappa, "Avalanche photodiodes and quenching circuits for single-photon detection," *Appl. Opt.*, vol. 35, no. 12, p. 1956, Apr. 1996, doi:10.1364/AO.35.001956.

[117] S. Tisa, F. Zappa, A. Tosi, and S. Cova, "Electronics for single photon avalanche diode arrays," *Sensors Actuators A Phys.*, vol. 140, no. 1, pp. 113–122, Oct. 2007, doi:10.1016/J.SNA.2007.06.022.

[118] F. Zappa, M. Ghioni, S. Cova, C. Samori, and A. C. Giudice, "An integrated active-quenching circuit for single-photon avalanche diodes," *IEEE Trans. Instrum. Meas.*, vol. 49, no. 6, pp. 1167–1175, 2000, doi:10.1109/19.893251.

[119] A. Gallivanoni, I. Rech, and M. Ghioni, "Progress in Quenching Circuits for Single Photon Avalanche Diodes," *IEEE Trans. Nucl. Sci.*, Dec. 2010, doi:10.1109/TNS.2010.2074213.

[120] S. Deng and A. P. Morrison, "Active quench and reset integrated circuit with novel hold-off time control logic for Geiger-mode avalanche photodiodes," *Opt. Lett.*, vol. 37, no. 18, p. 3876, Sep. 2012, doi:10.1364/OL.37.003876.

[121] F. Zappa, A. Lotito, A. C. Giudice, S. Cova, and M. Ghioni, "Monolithic active-quenching and active-reset circuit for single-photon avalanche detectors," *IEEE J. Solid-State Circuits*, vol. 38, no. 7, pp. 1298–1301, Jul. 2003, doi:10.1109/JSSC.2003.813291.

[122] C. Hu, M. Liu, and J. C. Campbell, "Improved passive quenching with active reset circuit," 2009, vol. 7320, p. 73200W, doi:10.1117/12.818313.

[123] C. Hu, M. Liu, X. Zheng, and J. C. Campbell, "Dynamic Range of Passive Quenching Active Reset Circuit for Single Photon Avalanche Diodes," *IEEE J. Quantum Electron.*, vol. 46, no. 1, pp. 35–39, Jan. 2010, doi:10.1109/JQE.2009.2024086.

[124] I. Berdalovic, Z. Osrecki, F. Segmanovic, D. Grubisic, T. Knezevic, and T. Suligoj, "Design of passive-quenching active-reset circuit with adjustable hold-off time for single-photon avalanche diodes," in *2016 39th International Convention on Information and Communication Technology, Electronics and Microelectronics (MIPRO)*, 2016, pp. 34–39, doi:10.1109/MIPRO.2016.7522106.

[125] Y. Maruyama, J. Blacksberg, and E. Charbon, "A time-resolved 128x128 SPAD camera for laser Raman spectroscopy," 2012, vol. 8374, p. 83740N, doi:10.1117/12.920597.

[126] H. Zimmermann, "Silicon Technologies and Integrated Photodetectors," in *Integrated Silicon Optoelectronics*, Springer, Berlin, Heidelberg, 2009, pp. 29–153, doi:10.1007/978-3-642-01521-2_3.

[127] D. A. Ramirez, M. M. Hayat, and M. A. Itzler, "Dependence of the performance of single photon avalanche diodes on the multiplication region width," *IEEE J. Quantum Electron.*, vol. 44, no. 12, pp. 1188–1195, 2008, doi:10.1109/JQE.2008.2003140.

[128] C. Niclass, M. Gersbach, R. Henderson, L. Grant, and E. Charbon, "A Single Photon Avalanche Diode Implemented in 130-nm CMOS Technology," *IEEE J. Sel. Top. Quantum Electron.*, vol. 13, no. 4, pp. 863–869, 2007, doi:10.1109/JSTQE.2007.903854.

[129] N. Faramarzpour, M. J. Deen, S. Shirani, and Q. Fang, "Fully integrated single photon avalanche diode detector in standard CMOS 0.18-μm technology," *IEEE Trans. Electron Devices*, 2008, doi:10.1109/TED.2007.914839.

[130] M. Ghioni, A. Gulinatti, I. Rech, F. Zappa, and S. Cova, "Progress in silicon single-photon avalanche diodes," *IEEE J. Sel. Top. Quantum Electron.*, vol. 13, no. 4, pp. 852–862, 2007, doi:10.1109/JSTQE.2007.902088.

[131] E. Vilella, O. Alonso, A. Montiel, and A. Diéguez, "Characterization of temperature effects on single-photon avalanche diodes fabricated in a HV-CMOS conventional technology," in *2013 Symposium on Design, Test, Integration and Packaging of MEMS/MOEMS.*, 2013.

[132] M. Gersbach *et al.*, "A low-noise single-photon detector implemented in a 130 nm CMOS imaging process," *Solid. State. Electron.*, vol. 53, no. 7, pp. 803–808, Jul. 2009, doi:10.1016/J.SSE.2009.02.014.

[133] J. A. Richardson, L. A. Grant, and R. K. Henderson, "Low Dark Count Single-Photon Avalanche Diode Structure Compatible With Standard Nanometer Scale CMOS Technology," *IEEE Photonics Technol. Lett.*, vol. 21, no. 14, pp. 1020–1022, Jul. 2009, doi:10.1109/LPT.2009.2022059.

[134] R. K. Henderson, J. Richardson, and L. A. Gran, "Reduction of band-to-

band tunneling in deep-submicron CMOS single photon avalanche photodiodes," in *International Image Sensor Workshop*, 2009.

[135] E. Vilella, O. Alonso, A. Montiel, A. Vilà, and A. Diéguez, "A low-noise time-gated single-photon detector in a HV-CMOS technology for triggered imaging," *Sensors Actuators A Phys.*, vol. 201, pp. 342–351, 2013, doi:10.1016/j.sna.2013.08.006.

[136] W. J. Kindt and H. W. Van Zeijl, "Modelling and fabrication of Geiger mode avalanche photodiodes," *IEEE Trans. Nucl. Sci.*, vol. 45, no. 3, pp. 715–719, Jun. 1998, doi:10.1109/23.682621.

[137] S. Cova, A. Lacaita, and G. Ripamonti, "Trapping phenomena in avalanche photodiodes on nanosecond scale," *IEEE Electron Device Lett.*, vol. 12, no. 12, pp. 685–687, Dec. 1991, doi:10.1109/55.116955.

[138] A. Eisele *et al.*, "185 MHz Count Rate, 139 dB Dynamic Range Single-Photon Avalanche Diode with Active Quenching Circuit in 130 nm CMOS Technology," in *International Image Sensor Workshop*, 2011.

[139] D. Bronzi, S. Tisa, F. Villa, S. Bellisai, A. Tosi, and F. Zappa, "Fast Sensing and Quenching of CMOS SPADs for Minimal Afterpulsing Effects," *IEEE Photonics Technol. Lett.*, vol. 25, no. 8, pp. 776–779, Apr. 2013, doi:10.1109/LPT.2013.2251621.

[140] M. W. Fishburn, "Fundamentals of CMOS Single-Photon Avalanche Diodes," Delft University of Technology, 2012doi:10.4233/UUID:7ED6E57D-404E-4372-8053-6B0B5C7FA0FE.

[141] E. Sciacca *et al.*, "Arrays of Geiger Mode Avalanche Photodiodes," *IEEE PHOTONICS Technol. Lett.*, vol. 18, no. 15, pp. 1633–1635, 2006, doi:10.1109/LPT.2006.879576.

[142] A. Ficorella *et al.*, "Crosstalk mapping in CMOS SPAD arrays," in *2016 46th European Solid-State Device Research Conference (ESSDERC)*, 2016, pp. 101–104, doi:10.1109/ESSDERC.2016.7599598.

[143] A. Rochas, "Single Photon Avalanche Diodes in CMOS Technology," École Polytechnique Fédérale De Lausanne, 2003doi:10.5075/epfl-thesis-2814.

[144] C. Veerappan and E. Charbon, "A Substrate Isolated CMOS SPAD Enabling Wide Spectral Response and Low Electrical Crosstalk," *IEEE J. Sel. Top. Quantum Electron.*, vol. 20, no. 6, pp. 299–305, Nov. 2014, doi:10.1109/JSTQE.2014.2318436.

[145] C. Veerappan and E. Charbon, "A Low Dark Count p-i-n Diode Based SPAD in CMOS Technology," *IEEE Trans. Electron Devices*, vol. 63, no. 1, pp. 65–71, Jan. 2016, doi:10.1109/TED.2015.2475355.

[146] J. R. Meijlink *et al.*, "First measurement of scintillation photon arrival

statistics using a high-granularity solid-state photosensor enabling time-stamping of up to 20,480 single photons," in *IEEE Nuclear Science Symposium Conference Record*, 2011, pp. 2254–2257, doi:10.1109/NSSMIC.2011.6152491.

[147] M. Assanelli, A. Ingargiola, I. Rech, A. Gulinatti, and M. Ghioni, "Photon-Timing Jitter Dependence on Injection Position in Single-Photon Avalanche Diodes," *IEEE J. Quantum Electron.*, vol. 47, no. 2, pp. 151–159, Feb. 2011, doi:10.1109/JQE.2010.2068038.

[148] D. Bronzi, F. Villa, S. Bellisai, S. Tisa, G. Ripamonti, and A. Tosi, "Figures of merit for CMOS SPADs and arrays," 2013, vol. 8773, p. 877304, doi:10.1117/12.2017357.

[149] J. Arlt, D. Tyndall, B. R. Rae, D. D.-U. Li, J. A. Richardson, and R. K. Henderson, "A study of pile-up in integrated time-correlated single photon counting systems," *Rev. Sci. Instrum.*, vol. 84, no. 10, p. 103105, Oct. 2013, doi:10.1063/1.4824196.

[150] S. Isbaner *et al.*, "Dead-time correction of fluorescence lifetime measurements and fluorescence lifetime imaging," *Opt. Express*, vol. 24, no. 9, p. 9429, May 2016, doi:10.1364/OE.24.009429.

[151] J. Requejo-Isidro *et al.*, "High-speed wide-field time-gated endoscopic fluorescence-lifetime imaging," *Opt. Lett.*, vol. 29, no. 19, p. 2249, Oct. 2004, doi:10.1364/ol.29.002249.

[152] V. Y. Soloviev *et al.*, "Fluorescence lifetime imaging by using time-gated data acquisition," *Appl. Opt.*, vol. 46, no. 30, pp. 7384–7391, Oct. 2007, doi:10.1364/AO.46.007384.

[153] M. Rashdan, "Multi-step and high-resolution vernier-based TDC architecture," in *Proceedings of the International Conference on Microelectronics, ICM*, 2018, vol. 2017-December, pp. 1–4, doi:10.1109/ICM.2017.8268819.

[154] M. Crotti, I. Rech, and M. Ghioni, "Note: Fully integrated time-to-amplitude converter in Si–Ge technology," *Rev. Sci. Instrum.*, vol. 81, no. 10, p. 106103, Oct. 2010, doi:10.1063/1.3481162.

[155] P. Kapusta, M. Wahl, and R. Erdmann, *Advanced Photon Counting: Applications, Methods, Instrumentation*. Springer International Publishing, 2015, doi:10.1007/978-3-319-15636-1.

[156] D. Tamborini, D. Portaluppi, F. Villa, and F. Zappa, "Eight-Channel 21 ps Precision 10 µs Range Time-to-Digital Converter Module," *IEEE Trans. Instrum. Meas.*, vol. 65, no. 2, pp. 423–430, Feb. 2016, doi:10.1109/TIM.2015.2485378.

[157] S. Henzler, *Time-to-Digital Converters*, 1st ed. New York: Springer, 2010, doi:10.1007/978-90-481-8628-0.

[158] G. W. Roberts and M. Ali-Bakhshian, “A Brief Introduction to Time-to-Digital and Digital-to-Time Converters,” *IEEE Trans. Circuits Syst. II Express Briefs*, vol. 57, no. 3, pp. 153–157, Mar. 2010, doi:10.1109/TCSII.2010.2043382.

[159] J. Kalisz, “Review of methods for time interval measurements with picosecond resolution,” *Metrologia*, vol. 41, no. 1, p. 17, Feb. 2004, doi:10.1088/0026-1394/41/1/004.

[160] J. Wang, S. Liu, Q. Shen, H. Li, and Q. An, “A Fully Fledged TDC Implemented in Field-Programmable Gate Arrays,” *IEEE Trans. Nucl. Sci.*, vol. 57, no. 2, pp. 446–450, Apr. 2010, doi:10.1109/TNS.2009.2037958.

[161] C. Favi and E. Charbon, “A 17ps time-to-digital converter implemented in 65nm FPGA technology,” in *FPGA ’09 Proceedings of the ACM/SIGDA international symposium on Field programmable gate arrays*, 2009, pp. 113–120, doi:10.1145/1508128.1508145.

[162] A. M. Amiri, A. Khouas, and M. Boukadoum, “Pseudorandom Stimuli Generation for Testing Time-to-Digital Converters on an FPGA,” *IEEE Trans. Instrum. Meas.*, vol. 58, no. 7, pp. 2209–2215, Jul. 2009, doi:10.1109/TIM.2009.2013670.

[163] A. M. Amiri, A. Khouas, and M. Boukadoum, “On the Timing Uncertainty in Delay-Line-based Time Measurement Applications Targeting FPGAs,” in *2007 IEEE International Symposium on Circuits and Systems*, 2007, pp. 3772–3775, doi:10.1109/ISCAS.2007.378782.

[164] B. I. Abdulrazzaq, I. Abdul Halin, S. Kawahito, R. M. Sidek, S. Shafie, and N. A. M. Yunus, “A review on high-resolution CMOS delay lines: towards sub-picosecond jitter performance,” *Springerplus*, vol. 5, no. 1, p. 434, Dec. 2016, doi:10.1186/s40064-016-2090-z.

[165] R. Salomon and R. Joost, “BOUNCE: A New High-Resolution Time-Interval Measurement Architecture,” *IEEE Embed. Syst. Lett.*, vol. 1, no. 2, pp. 56–59, Aug. 2009, doi:10.1109/LES.2009.2034711.

[166] M.-A. Daigneault and J.-P. David, “Towards 5ps resolution TDC on a dynamically reconfigurable FPGA,” in *Proceedings of the 18th Annual ACM/SIGDA International Symposium on Field Programmable Gate Arrays*, 2010, pp. 283–283, doi:10.1145/1723112.1723161.

[167] P. Hong, H. Xu, and J. Jin, “High resolution TDC and high linearity DTC for all-digital spur calibration,” in *2018 IEEE MTT-S International Wireless Symposium (IWS)*, 2018, pp. 1–3, doi:10.1109/IEEE-IWS.2018.8400823.

[168] M. Lee, M. E. Heidari, and A. A. Abidi, “A Low-Noise Wideband Digital Phase-Locked Loop Based on a Coarse–Fine Time-to-Digital Converter With Subpicosecond Resolution,” *IEEE J. Solid-State Circuits*, vol. 44, no.

10, pp. 2808–2816, Oct. 2009, doi:10.1109/JSSC.2009.2028753.

[169] Y.-H. Seo, J.-S. Kim, H.-J. Park, and J.-Y. Sim, "A 0.63ps resolution, 11b pipeline TDC in 0.13µm CMOS," in *2011 Symposium on VLSI Circuits - Digest of Technical Papers*, 2011, pp. 152–153.

[170] B. Markovic, D. Tamborini, F. Villa, S. Tisa, A. Tosi, and F. Zappa, "10 ps resolution, 160 ns full scale range and less than 1.5% differential non-linearity time-to-digital converter module for high performance timing measurements," *Rev. Sci. Instrum.*, vol. 83, no. 7, p. 074703, Jul. 2012, doi:10.1063/1.4733705.

[171] J. M. Pavia, M. Scandini, S. Lindner, M. Wolf, and E. Charbon, "A 1 X 400 Backside-Illuminated SPAD Sensor with 49.7 ps Resolution, 30 pJ/Sample TDCs Fabricated in 3D CMOS Technology for Near-Infrared Optical Tomography," *IEEE J. Solid-State Circuits*, 2015, doi:10.1109/JSSC.2015.2467170.

[172] A. S. Yousif and J. W. Haslett, "A Fine Resolution TDC Architecture for Next Generation PET Imaging," *IEEE Trans. Nucl. Sci.*, vol. 54, no. 5, pp. 1574–1582, Oct. 2007, doi:10.1109/TNS.2007.903183.

[173] S. Henzler, S. Koeppe, W. Kamp, H. Mulatz, and D. Schmitt-Landsiedel, "90nm 4.7ps-Resolution 0.7-LSB Single-Shot Precision and 19pJ-per-Shot Local Passive Interpolation Time-to-Digital Converter with On-Chip Characterization," in *2008 IEEE International Solid-State Circuits Conference - Digest of Technical Papers*, 2008, pp. 548–635, doi:10.1109/ISSCC.2008.4523300.

[174] M. Wahl *et al.*, "Integrated multichannel photon timing instrument with very short dead time and high throughput," *Rev. Sci. Instrum.*, vol. 84, no. 4, p. 043102, Apr. 2013, doi:10.1063/1.4795828.

[175] P. Chen, Y.-Y. Hsiao, Y.-S. Chung, W. X. Tsai, and J.-M. Lin, "A 2.5-ps Bin Size and 6.7-ps Resolution FPGA Time-to-Digital Converter Based on Delay Wrapping and Averaging," *IEEE Trans. Very Large Scale Integr. Syst.*, vol. 25, no. 1, pp. 114–124, Jan. 2017, doi:10.1109/TVLSI.2016.2569626.

[176] B. R. Rae *et al.*, "A CMOS Time-Resolved Fluorescence Lifetime Analysis Micro-System," *Sensors*, vol. 9, no. 11, pp. 9255–9274, Nov. 2009, doi:10.3390/s91109255.

[177] F. Villa *et al.*, "SPAD Smart Pixel for Time-of-Flight and Time-Correlated Single-Photon Counting Measurements," *IEEE Photonics J.*, vol. 4, no. 3, pp. 795–804, Jun. 2012, doi:10.1109/JPHOT.2012.2198459.

[178] D. E. Schwartz, E. Charbon, and K. L. Shepard, "A Single-Photon Avalanche Diode Array for Fluorescence Lifetime Imaging Microscopy," *IEEE J. Solid-State Circuits*, vol. 43, no. 11, pp. 2546–2557, Nov. 2008,

doi:10.1109/JSSC.2008.2005818.

[179] C. Veerappan *et al.*, "A 160x128 single-photon image sensor with on-pixel 55ps 10b time-to-digital converter," *Dig. Tech. Pap. - IEEE Int. Solid-State Circuits Conf.*, pp. 312–313, Feb. 2011, doi:10.1109/ISSCC.2011.5746333.

[180] I. Antolovic *et al.*, "Photon-Counting Arrays for Time-Resolved Imaging," *Sensors*, vol. 16, no. 7, p. 1005, Jun. 2016, doi:10.3390/s16071005.

[181] A. C. Ulku *et al.*, "A 512 × 512 SPAD Image Sensor With Integrated Gating for Widefield FLIM," *IEEE J. Sel. Top. Quantum Electron.*, vol. 25, no. 1, pp. 1–12, Jan. 2019, doi:10.1109/JSTQE.2018.2867439.

[182] L. Pancheri and D. Stoppa, "A SPAD-based pixel linear array for high-speed time-gated fluorescence lifetime imaging," in *2009 Proceedings of ESSCIRC*, 2009, pp. 428–431, doi:10.1109/ESSCIRC.2009.5325948.

[183] N. A. W. Dutton *et al.*, "A time-correlated single-photon-counting sensor with 14GS/S histogramming time-to-digital converter," in *2015 IEEE International Solid-State Circuits Conference - (ISSCC) Digest of Technical Papers*, 2015, pp. 1–3, doi:10.1109/ISSCC.2015.7062997.

[184] A. T. Erdogan, R. Walker, N. Finlayson, N. Krstajic, G. O. S. Williams, and R. K. Henderson, "A 16.5 giga events/s 1024 × 8 SPAD line sensor with per-pixel zoomable 50ps-6.4ns/bin histogramming TDC," in *2017 Symposium on VLSI Circuits*, 2017, pp. C292–C293, doi:10.23919/VLSIC.2017.8008513.

[185] L. Pancheri, N. Massari, and D. Stoppa, "SPAD Image Sensor With Analog Counting Pixel for Time-Resolved Fluorescence Detection," *IEEE Trans. Electron Devices*, vol. 60, no. 10, pp. 3442–3449, Oct. 2013, doi:10.1109/TED.2013.2276752.

[186] N. A. W. Dutton *et al.*, "Single Photon Counting Performance and Noise Analysis of CMOS SPAD-Based Image Sensors," *Sensors*, vol. 16, no. 7, p. 1122, Jul. 2016, doi:10.3390/s16071122.

[187] M. Perenzoni, L. Pancheri, D. Stoppa, M. Perenzoni, L. Pancheri, and D. Stoppa, "Compact SPAD-Based Pixel Architectures for Time-Resolved Image Sensors," *Sensors*, vol. 16, no. 5, p. 745, May 2016, doi:10.3390/s16050745.

[188] M. Perenzoni, N. Massari, D. Perenzoni, L. Gasparini, and D. Stoppa, "A 160x120 Pixel Analog-Counting Single-Photon Imager With Time-Gating and Self-Referenced Column-Parallel A/D Conversion for Fluorescence Lifetime Imaging," *IEEE J. Solid-State Circuits*, vol. 51, no. 1, pp. 155–167, Jan. 2016, doi:10.1109/JSSC.2015.2482497.

[189] S. Tisa, F. Guerrieri, and F. Zappa, "Variable-load quenching circuit for single-photon avalanche diodes," *Opt. Express*, vol. 16, no. 3, p. 2232, Feb.

2008, doi:10.1364/OE.16.002232.

[190] E. Vilella, A. Comerma, O. Alonso, D. Gascon, and A. Diéguez, "Gated Geiger mode avalanche photodiode pixels with integrated readout electronics for low noise photon detection," *Nucl. Instruments Methods Phys. Res. Sect. A Accel. Spectrometers, Detect. Assoc. Equip.*, vol. 695, pp. 218–221, Dec. 2012, doi:10.1016/j.nima.2011.12.026.

[191] C. Accarino *et al.*, "Low Noise and High Photodetection Probability SPAD in 180 nm Standard CMOS Technology," in *2018 IEEE International Symposium on Circuits and Systems (ISCAS)*, 2018, pp. 1–4, doi:10.1109/ISCAS.2018.8351173.

[192] I. Malass, W. Uhring, J.-P. Le Normand, N. Dumas, and F. Dadouche, "Evaluation of size influence on performance figures of a single photon avalanche diode fabricated in a 180 nm standard CMOS technology," *Analog Integr. Circuits Signal Process.*, vol. 89, no. 1, pp. 69–76, Oct. 2016, doi:10.1007/s10470-016-0763-8.

[193] G. Humer, M. Peev, C. Schaeff, S. Ramelow, M. Stipčević, and R. Ursin, "A Simple and Robust Method for Estimating Afterpulsing in Single Photon Detectors," *J. Light. Technol.*, vol. 33, no. 14, pp. 3098–3107, Jul. 2015, doi:10.1109/JLT.2015.2428053.

[194] Y. Zhang, P. Huang, and R. Zhu, "Upgrading of Integration of Time to Digit Converter on a Single FPGA," in *Proc. 15th Int. Laser Ranging Workshop*, 2006.

[195] J. Song, Q. An, and S. Liu, "A high-resolution time-to-digital converter implemented in field-programmable-gate-arrays," *IEEE Trans. Nucl. Sci.*, vol. 53, no. 1, pp. 236–241, 2006, doi:10.1109/TNS.2006.869820.

[196] A. Aloisio, P. Branchini, R. Cicalese, R. Giordano, V. Izzo, and S. Loffredo, "FPGA implementation of a high-resolution time-to-digital converter," in *2007 IEEE Nuclear Science Symposium Conference Record*, 2007, pp. 504–507, doi:10.1109/NSSMIC.2007.4436379.

[197] N. Minas, D. Kinniment, K. Heron, and G. Russell, "A high resolution flash time-to-digital converter taking into account process variability," in *Proceedings - International Symposium on Asynchronous Circuits and Systems*, 2007, pp. 163–174, doi:10.1109/async.2007.7.

[198] S. S. Junnarkar, P. O'Connor, and R. R. Fontaine, "FPGA based self calibrating 40 picosecond resolution, wide range time to digital converter," in *IEEE Nuclear Science Symposium Conference Record*, 2008, pp. 3434–3439, doi:10.1109/NSSMIC.2008.4775078.

[199] L. Zhao, X. Hu, S. Liu, J. Wang, and Q. An, "A 16-channel 15 ps TDC implemented in a 65 nm FPGA," in *2012 18th IEEE-NPSS Real Time Conference*, 2012, pp. 1–5, doi:10.1109/RTC.2012.6418164.

[200] J. Wu, “On-chip processing for the wave union TDC implemented in FPGA,” in *2009 16th IEEE-NPSS Real Time Conference - Conference Record*, 2009, pp. 279–282, doi:10.1109/RTC.2009.5322002.

[201] J. Wu, S. Hansen, and Z. shi, “ADC and TDC implemented using FPGA,” in *2007 IEEE Nuclear Science Symposium Conference Record*, 2007, pp. 281–286.

[202] Xilinx Inc, “7 Series FPGAs Configurable Logic Block User Guide (UG474),” 2016.

[203] J. Wu, “Several Key Issues on Implementing Delay Line Based TDCs Using FPGAs,” *IEEE Trans. Nucl. Sci.*, vol. 57, no. 3, pp. 1543–1548, Jun. 2010, doi:10.1109/TNS.2010.2045901.

[204] Q. Shen *et al.*, “A fast improved fat tree encoder for wave union TDC in an FPGA,” *Chinese Phys. C*, vol. 37, no. 10, p. 106102, Oct. 2013, doi:10.1088/1674-1137/37/10/106102.

[205] M. Fishburn, L. H. Menninga, C. Favi, and E. Charbon, “A 19.6 ps, FPGA-Based TDC With Multiple Channels for Open Source Applications,” *IEEE Trans. Nucl. Sci.*, vol. 60, no. 3, pp. 2203–2208, Jun. 2013, doi:10.1109/TNS.2013.2241789.

[206] C. J. Grauw and H. C. Gerritsen, “Multiple Time-Gate Module for Fluorescence Lifetime Imaging,” *Appl. Spectrosc.*, vol. 55, no. 6, pp. 670–678, Jun. 2001, doi:10.1366/0003702011952587.

[207] K. K. Sharman, A. Periasamy, H. Ashworth, and J. N. Demas, “Error Analysis of the Rapid Lifetime Determination Method for Double-Exponential Decays and New Windowing Schemes,” *Anal. Chem.*, vol. 71, no. 5, pp. 947–952, Jan. 1999, doi:10.1021/ac981050d.

[208] K. M. Ring and S. Krishnan, “Long-term jitter reduction through supply noise compensation,” in *2008 IEEE International Symposium on Circuits and Systems*, 2008, pp. 2382–2385, doi:10.1109/ISCAS.2008.4541934.

[209] J. Wu and Z. Shi, “The 10-ps wave union TDC: Improving FPGA TDC resolution beyond its cell delay,” in *IEEE Nuclear Science Symposium Conference Record*, 2008, pp. 3440–3446, doi:10.1109/NSSMIC.2008.4775079.

[210] R. Pelka, J. Kalisz, and R. Szplet, “Nonlinearity correction of the integrated time-to-digital converter with direct coding,” *IEEE Trans. Instrum. Meas.*, vol. 46, no. 2, pp. 449–453, Apr. 1997, doi:10.1109/19.571882.

[211] Biomarkers Definitions Working Group, “Biomarkers and surrogate endpoints: Preferred definitions and conceptual framework,” *Clin. Pharmacol. Ther.*, vol. 69, no. 3, pp. 89–95, Mar. 2001, doi:10.1067/mcp.2001.113989.

[212] B. Biswas, “Clinical Performance Evaluation of Molecular Diagnostic Tests,” in *Journal of Molecular Diagnostics*, 2016, vol. 18, no. 6, pp. 803–812, doi:10.1016/j.jmoldx.2016.06.008.

[213] B. L. Wickes and N. P. Wiederhold, “Molecular diagnostics in medical mycology,” *Nature Communications*, vol. 9, no. 1. Nature Publishing Group, 01-Dec-2018.

[214] C. Hempen and U. Karst, “Labeling strategies for bioassays,” *Analytical and Bioanalytical Chemistry*, vol. 384, no. 3. pp. 572–583, Feb-2006.

[215] K. Nishi, S.-I. Isobe, Y. Zhu, and R. Kiyama, “Fluorescence-Based Bioassays for the Detection and Evaluation of Food Materials,” *Sensors*, vol. 15, no. 10, pp. 25831–25867, Oct. 2015, doi:10.3390/s151025831.

[216] W. Jung *et al.*, “Point-of-care testing (POCT) diagnostic systems using microfluidic lab-on-a-chip technologies,” *Microelectron. Eng.*, vol. 132, pp. 46–57, Jan. 2014, doi:10.1016/j.mee.2014.09.024.

[217] P. Abgrall and A.-M. Gué, “Lab-on-chip technologies: making a microfluidic network and coupling it into a complete microsystem—a review,” *J. Micromechanics Microengineering*, vol. 17, no. 5, pp. R15–R49, May 2007, doi:10.1088/0960-1317/17/5/R01.

[218] T. Luo *et al.*, “Microfluidic Single-Cell Manipulation and Analysis: Methods and Applications,” *Micromachines*, vol. 10, no. 2, p. 104, Feb. 2019, doi:10.3390/mi10020104.

[219] S. Halldorssona, E. Lucumic, R. Gómez-Sjöbergb, and R. M. T. Fleming, “Advantages and challenges of microfluidic cell culture in polydimethylsiloxane devices,” *Biosens. Bioelectron.*, vol. 63, pp. 218–231, Jan. 2015, doi:10.1016/J.BIOS.2014.07.029.

[220] J. Chen, J. Li, and Y. Sun, “Microfluidic approaches for cancer cell detection, characterization, and separation,” *Lab Chip*, vol. 12, no. 10, p. 1753, Apr. 2012, doi:10.1039/c2lc21273k.

[221] J. Léonard *et al.*, “High-throughput time-correlated single photon counting,” *Lab Chip*, vol. 14, no. 22, pp. 4338–4343, 2014, doi:10.1039/c4lc00780h.

[222] H. Becker and C. Gärtner, “Polymer microfabrication technologies for microfluidic systems,” *Anal. Bioanal. Chem.*, vol. 390, no. 1, pp. 89–111, 2008, doi:10.1007/s00216-007-1692-2.

[223] A. Piruska *et al.*, “The autofluorescence of plastic materials and chips measured under laser irradiation,” *Lab Chip*, vol. 5, no. 12, p. 1348, Nov. 2005, doi:10.1039/b508288a.

[224] V. Sunkara, D.-K. Park, H. Hwang, R. Chantiwas, S. A. Soper, and Y.-K. Cho, “Simple room temperature bonding of thermoplastics and

poly(dimethylsiloxane),” *Lab Chip*, vol. 11, no. 5, pp. 962–965, Mar. 2011, doi:10.1039/C0LC00272K.

[225] D. C. Duffy, J. C. McDonald, O. J. A. Schueller, and G. M. Whitesides, “Rapid prototyping of microfluidic systems in poly(dimethylsiloxane),” *Anal. Chem.*, vol. 70, no. 23, pp. 4974–4984, 1998, doi:10.1021/ac980656z.

[226] M. K. Sushanta and S. (Editors) Chakraborty, *Microfluidics and Nanofluidics Handbook: Fabrication, Implementation, and Applications*, 1st ed. New York: CRC Press, 2012.

[227] MicroChem Corp., “Nano (TM) SU-8 Negative Tone Photoresist formulation 50-100 Data Sheet,” *MicroChem Corp.* [Online]. Available: http://www.microchem.com/pdf/SU8_50-100.pdf. [Accessed: 25-Jun-2019].

[228] V. Pinto, P. Sousa, V. Cardoso, and G. Minas, “Optimized SU-8 Processing for Low-Cost Microstructures Fabrication without Cleanroom Facilities,” *Micromachines*, vol. 5, no. 3, pp. 738–755, Sep. 2014, doi:10.3390/mi5030738.

[229] E. H. Conradie and D. F. Moore, “SU-8 thick photoresist processing as a functional material for MEMS applications,” *J. Micromechanics Microengineering*, vol. 12, no. 4, pp. 368–374, 2002.

[230] Dow Corning, “SYLGARD™ 184 Silicone Elastomer Kit.” [Online]. Available: https://consumer.dow.com/en-us/pdp.sylgard-184-silicone-elastomer-kit.01064291z.html?tab=overview&id=01064291z. [Accessed: 25-Jun-2019].

[231] Elveflow, “PDMS SOFTLITHOGRAPHY,” 2016. [Online]. Available: http://www.elveflow.com/microfluidic-tutorials/soft-lithography-reviews-and-tutorials/introduction-in-soft-lithography/pdms-softlithography-replication/. [Accessed: 15-Jun-2019].

[232] J. Zhu, Y. Tian, and X. Liu, “Rapid fabrication of super-hydrophobic surfaces of silicon wafers with excellent anisotropic wetting,” *Microsyst. Technol.*, vol. 25, no. 1, pp. 237–243, Jan. 2019, doi:10.1007/s00542-018-3955-6.

[233] I. D. Johnston, D. K. McCluskey, C. K. L. Tan, and M. C. Tracey, “Mechanical characterization of bulk Sylgard 184 for microfluidics and microengineering,” *J. Micromechanics Microengineering*, vol. 24, no. 3, p. 035017, Mar. 2014, doi:10.1088/0960-1317/24/3/035017.

[234] A. del Campo and C. Greiner, “SU-8: a photoresist for high-aspect-ratio and 3D submicron lithography,” *J. Micromechanics Microengineering*, vol. 17, no. 6, pp. R81–R95, Jun. 2007, doi:10.1088/0960-1317/17/6/R01.

[235] J. Zhang, M. B. Chan-Park, and S. R. Conner, “Effect of exposure dose on

the replication fidelity and profile of very high aspect ratio microchannels in SU-8," *Lab Chip*, vol. 4, no. 6, pp. 646–653, 2004, doi:10.1039/b403304c.

[236] C.-W. Tsao, "Polymer Microfluidics: Simple, Low-Cost Fabrication Process Bridging Academic Lab Research to Commercialized Production," *Micromachines*, vol. 7, no. 12, p. 225, Dec. 2016, doi:10.3390/mi7120225.

[237] L. Mou and X. Jiang, "Materials for Microfluidic Immunoassays: A Review," *Adv. Healthc. Mater.*, vol. 6, no. 15, p. 1601403, Aug. 2017, doi:10.1002/adhm.201601403.

[238] E. W. K. Young, E. Berthier, and D. J. Beebe, "Assessment of Enhanced Autofluorescence and Impact on Cell Microscopy for Microfabricated Thermoplastic Devices," *Anal. Chem.*, vol. 85, no. 1, pp. 44–49, Jan. 2013, doi:10.1021/ac3034773.

[239] J. Lachaux *et al.*, "Thermoplastic elastomer with advanced hydrophilization and bonding performances for rapid (30 s) and easy molding of microfluidic devices," *Lab Chip*, vol. 17, no. 15, pp. 2581–2594, Jul. 2017, doi:10.1039/C7LC00488E.

[240] T. Binkert, H. P. Tschanz, and P. E. Zinsli, "The measurement of fluorescence decay curves with the single-photon counting method and the evaluation of rate parameters," *J. Lumin.*, vol. 5, no. 3, pp. 187–217, 1972, doi:10.1016/0022-2313(72)90041-5.

[241] R. Z. Bachrach, "A photon counting apparatus for kinetic and spectral measurements," *Rev. Sci. Instrum.*, vol. 43, no. 5, pp. 734–737, 1972, doi:10.1063/1.1685743.

[242] C. Lewis, W. R. Ware, L. J. Doemeny, and T. L. Nemzek, "The measurement of short-lived fluorescence decay using the single photon counting method," *Rev. Sci. Instrum.*, vol. 44, no. 2, pp. 107–114, 1973, doi:10.1063/1.1686062.

[243] P. F. Moulton, "Spectroscopic and laser characteristics of Ti:Al_2O_3," *J. Opt. Soc. Am. B*, vol. 3, no. 1, p. 125, Jan. 1986, doi:10.1364/josab.3.000125.

[244] H. Schneckenburger, M. Wagner, P. Weber, W. S. L. Strauss, and R. Sailer, "Autofluorescence Lifetime Imaging of Cultivated Cells Using a UV Picosecond Laser Diode," *J. Fluoresc.*, vol. 14, no. 5, pp. 649–654, Sep. 2004, doi:10.1023/B:JOFL.0000039351.09916.cc.

[245] M. Kress *et al.*, "Time-resolved microspectrofluorometry and fluorescence lifetime imaging of photosensitizers using picosecond pulsed diode lasers in laser scanning microscopes," *J. Biomed. Opt.*, vol. 8, no. 1, p. 26, Jan. 2003, doi:10.1117/1.1528595.

[246] A. G. Ryder, S. Power, T. J. Glynn, and J. J. Morrison, "Time-domain

measurement of fluorescence lifetime variation with pH," in *Proc. SPIE Biomarkers and Biological Spectral Imaging*, 2001, vol. 4259, pp. 102–109, doi:10.1117/12.432487.

[247] C. D. Mcguinness, K. Sagoo, D. Mcloskey, and D. J. S. Birch, "A new sub-nanosecond LED at 280 nm: application to protein fluorescence," *Meas. Sci. Technol. Meas. Sci. Technol*, vol. 15, no. 15, pp. 19–22, Nov. 2004, doi:10.1088/0957-0233/15/11/L02.

[248] G. T. Kennedy *et al.*, "Fluorescence lifetime imaging using light emitting diodes," *J. Phys. D. Appl. Phys.*, vol. 41, no. 9, p. 094012, 2008, doi:10.1088/0022-3727/41/9/094012.

[249] D. S. Elson *et al.*, "Fluorescence lifetime system for microscopy and multiwell plate imaging with a blue picosecond diode laser," *Opt. Lett.*, vol. 27, no. 16, p. 1409, Aug. 2002, doi:10.1364/OL.27.001409.

[250] NKT photonics, Cologne, and Gemany, "PULSED DIODE LASERS." [Online]. Available: https://www.nktphotonics.com/lasers-fibers/product-category/pulsed-diode-lasers/. [Accessed: 20-Jun-2019].

[251] Edinburgh Instruments Ltd., Livingston, and UK, "Picosecond Pulsed Diode Sources." [Online]. Available: https://www.edinst.com/types/picosecond-pulsed-diode-sources/. [Accessed: 20-Jun-2019].

[252] Pico Quant GmbH, Berlin, and Germany, "Picosecond Pulsed Sources." [Online]. Available: https://www.picoquant.com/products/category/pulsed-lasers-and-leds. [Accessed: 20-Jun-2019].

[253] Scientific - HORIBA Ltd., kyoto, and Japan, "TCSPC Components." [Online]. Available: http://www.horiba.com/us/en/scientific/products/fluorescence-spectroscopy/lifetime/tcspc-components/. [Accessed: 20-Jun-2019].

[254] W. K. McFarlane, "An inexpensive nanosecond light pulser for use in photomultiplier system testing," *Rev. Sci. Instrum.*, vol. 45, no. 2, pp. 286–289, Feb. 1974, doi:10.1063/1.1686606.

[255] R. J. Baker and M. D. Pocha, "Nanosecond switching using power MOSFETs," *Rev. Sci. Instrum.*, vol. 61, no. 8, pp. 2211–2213, 1990, doi:10.1063/1.1141391.

[256] P. H. Binh, V. D. Trong, P. Renucci, and X. Marie, "Improving OOK modulation rate of visible led by peaking and carrier sweep-out effects using {n} -Schottky diodes-capacitance circuit," *J. Light. Technol.*, vol. 31, no. 12, pp. 2578–2583, 2013, doi:10.1109/JLT.2013.2271452.

[257] J. Nissinen and J. Kostamovaara, "A High Repetition Rate CMOS Driver for High-Energy Sub-ns Laser Pulse Generation in SPAD-Based Time-of-

Flight Range Finding," *IEEE Sens. J.*, vol. 16, no. 6, pp. 1628–1633, 2016, doi:10.1109/JSEN.2015.2503774.

[258] W. Uhring, C.-V. Zint, and J. Bartringer, "A low-cost high-repetition-rate picosecond laser diode pulse generator," *Proc. SPIE 5452, Semicond. Lasers Laser Dyn. 583*, vol. 5452, no. SEPTEMBER, pp. 583–590, 2004, doi:10.1117/12.545038.

[259] P. H. Binh, T. Vo, P. Renucci, and X. Marie, "100 ps Optical pulse generator using laser diodes for visible light communication applications," *Microw. Opt. Technol. Lett.*, vol. 56, no. 1, pp. 185–187, 2014, doi:10.1002/mop.28074.

[260] W. J. O'Hagan, M. Mckenna, D. C. Sherrington, O. J. Rolinski, and D. J. S. Birch, "MHz LED source for nanosecond fluorescence sensing," *Meas. Sci. Technol.*, vol. 13, no. 1, pp. 84–91, 2002, doi:10.1088/0957-0233/13/1/311.

[261] ThermoFisher Scientific, "Fluorescence SpectraViewer." [Online]. Available: https://bit.ly/2PgApWG. [Accessed: 20-Jun-2019].

[262] Zhiyuan Huang, Qi Fu, Peizhe Chen, Hongchun Yang, and Xiaolin Yang, "High power pulse generator based on avalanche transistor Marx circuit," in *2014 IEEE International Conference on Communiction Problem-solving*, 2014, pp. 315–317, doi:10.1109/ICCPS.2014.7062282.

[263] M. Sulkes and Z. Sulkes, "Measurement of luminescence decays: High performance at low cost," *Am. J. Phys.*, vol. 79, no. 11, p. 1104, 2011, doi:10.1119/1.3620415.

[264] N. Chadderton, W. Is, and A. Avalanche, "(AN-8) The ZTX415 Avalanche Mode Transistor," 1996.

[265] P. Protiva, J. Mrkvica, and J. Macháč, "Sub-nanosecond pulse generator for through-the-wall radar application," in *2nd European Microwave Technology Conference (EuMC)*, 2009, no. September, pp. 1904–1907, doi:10.1109/EUMC.2009.5295935.

[266] V. N. Rai, M. Shukla, R. K. Khardekar, and H. C. Pant, "A picosecond optical pulse generator to calibrate the optical streak camera," *Rev. Sci. Instrum.*, vol. 66, no. 5, pp. 3125–3130, 1995, doi:10.1063/1.1146499.

[267] L. Hallman, J. Huikari, and J. Kostamovaara, "A high-speed/power laser transmitter for single photon imaging applications," in *Proceedings of IEEE Sensors*, 2014, vol. 2014-Decem, no. December, pp. 1157–1160, doi:10.1109/ICSENS.2014.6985213.

[268] M. I. Gallant, "Pulse Circuits for Infrared LEDs and Visible Diode Lasers," 2008. [Online]. Available: http://www.jensign.com/opto/ledlaserdrivers/. [Accessed: 20-Jun-2019].

[269] K. Konnerth and C. Lanza, “Delay between current pulse and light emission of a gallium arsenide injection laser,” *Appl. Phys. Lett.*, vol. 4, no. 7, pp. 120–121, 1964, doi:10.1063/1.1753990.

[270] K. Petermann, “Intensity-Modulation Characteristics of Laser Diodes,” in *Laser Diode Modulation and Noise*, Springer, Dordrecht, 1988, pp. 78–114, doi:10.1007/978-94-009-2907-4_4.

[271] P. K. K. Hamamatsu, “ULTRAFAST MSM PHOTODETECTORS G4176 SERIES (GaAs),” 2003. [Online]. Available: http://pdf.datasheetcatalog.com/datasheet/hamamatsu/G7096-01.pdf. [Accessed: 28-Dec-2019].

[272] X. Yu, N. Schneiderhan-Marra, and T. O. Joos, “Protein microarrays for personalized medicine,” *Clinical Chemistry*, vol. 56, no. 3. pp. 376–387, 01-Mar-2010.

[273] SPD Swiss Precision Diagnostics GmbH, “Pregnancy Tests: Digital Tests, Sticks and Kits - Clearblue.” [Online]. Available: https://www.clearblue.com/pregnancy-tests. [Accessed: 22-Dec-2019].

[274] Abbott, “FreeStyle - Blood Glucose Monitoring Systems, Lancing Device, Lancets.” [Online]. Available: https://www.myfreestyle.com/. [Accessed: 22-Dec-2019].

[275] P. Wang and L. J. Kricka, “Current and Emerging Trends in Point-of-Care Technology and Strategies for Clinical Validation and Implementation,” 2018, doi:10.1373/clinchem.2018.287052.

[276] C. D. Chin, V. Linder, and S. K. Sia, “Commercialization of microfluidic point-of-care diagnostic devices,” *Lab on a Chip*, vol. 12, no. 12. Royal Society of Chemistry, pp. 2118–2134, 21-Jun-2012.

[277] D. T. Nieuwlandt, P. Papst, and M. J. Lochhead, “Multiplexed Host Response Biomarker Analysis on a Rapid, Quantitative Point-of-Care Platform.” AACC, 2018.

[278] T. Broger *et al.*, “Diagnostic Performance of Tuberculosis-Specific IgG Antibody Profiles in Patients with Presumptive Tuberculosis from Two Continents,” *Clin. Infect. Dis.*, vol. 64, no. 7, pp. 947–955, Apr. 2017, doi:10.1093/cid/cix023.

[279] M. Givens *et al.*, “Near patient CD4 count in a hospitalized HIV patient population,” *Cytom. Part B Clin. Cytom.*, vol. 92, no. 6, pp. 451–455, Nov. 2017, doi:10.1002/cyto.b.21248.

[280] S. R. Bickman *et al.*, “An Innovative Portable Biosensor System for the Rapid Detection of Freshwater Cyanobacterial Algal Bloom Toxins,” *Environ. Sci. Technol.*, p. acs.est.8b02769, Sep. 2018, doi:10.1021/acs.est.8b02769.

[281] K. N. Han, C. A. Li, and G. H. Seong, “Microfluidic Chips for Immunoassays,” *Annu. Rev. Anal. Chem.*, vol. 6, no. 1, pp. 119–141, Jun. 2013, doi:10.1146/annurev-anchem-062012-092616.

[282] U. Resch-Genger, M. Grabolle, S. Cavaliere-Jaricot, R. Nitschke, and T. Nann, “Quantum dots versus organic dyes as fluorescent labels,” 2008, doi:10.1038/NMEtH.1248.

[283] A. Savitzky and M. J. E. Golay, “Smoothing and Differentiation of Data by Simplified Least Squares Procedures.,” *Anal. Chem.*, vol. 36, no. 8, pp. 1627–1639, Jul. 1964, doi:10.1021/ac60214a047.

[284] A. K. Gaigalas, P. Derose, L. Wang, and Y.-Z. Zhang, “Optical Properties of CdSe/ZnS Nanocrystals,” vol. 119, 2014, doi:10.6028/jres.119.026.

[285] H. ZANG, Z. XU, and M. COTLET, “CORE-SIZE DEPENDENT PHOTOLUMINESCENCE BLINKING OF ISOLATED QUANTUM DOT-FULLERENE HYBRIDS,” *Biophys. Rev. Lett.*, vol. 08, no. 03n04, pp. 255–264, Dec. 2013, doi:10.1142/S1793048013500094.

[286] C. D. Salthouse, R. Weissleder, and U. Mahmood, “Development of a time domain fluorimeter for fluorescent lifetime multiplexing analysis.,” *IEEE Trans. Biomed. Circuits Syst.*, vol. 2, no. 3, pp. 204–11, Sep. 2008, doi:10.1109/TBCAS.2008.2003195.

[287] H. Wang, Y. Qi, T. J. Mountziaris, and C. D. Salthouse, “A portable time-domain LED fluorimeter for nanosecond fluorescence lifetime measurements,” *Rev. Sci. Instrum.*, vol. 85, no. 5, 2014, doi:10.1063/1.4873330.

[288] E. P. Dupont *et al.*, “Fluorescent magnetic bead and cell differentiation/counting using a CMOS SPAD matrix,” *Sensors Actuators, B Chem.*, vol. 174, pp. 609–615, 2012, doi:10.1016/j.snb.2012.06.049.

[289] M. Y. Berezin and S. Achilefu, “Fluorescence Lifetime Measurements and Biological Imaging,” *Chem. Rev.*, vol. 110, no. 5, pp. 2641–2684, May 2010, doi:10.1021/cr900343z.

[290] B. J. Van Meer *et al.*, “Small molecule absorption by PDMS in the context of drug response bioassays,” *Biochem. Biophys. Res. Commun.*, vol. 482, no. 2, pp. 323–328, Jan. 2017, doi:10.1016/j.bbrc.2016.11.062.

[291] A. Gokaltun, M. L. Yarmush, A. Asatekin, and O. B. Usta, “Recent advances in nonbiofouling PDMS surface modification strategies applicable to microfluidic technology,” *TECHNOLOGY*, vol. 05, no. 01, pp. 1–12, Mar. 2017, doi:10.1142/S2339547817300013.

[292] O. Kwon, K. Lee, and D. Lee, “An automated point-of-care instrument for molecular testing,” in *2015 15th International Conference on Control, Automation and Systems (ICCAS)*, 2015, pp. 1275–1278, doi:10.1109/ICCAS.2015.7364832.

[293] K. C. Park, D. C. Gaze, P. O. Collinson, and M. S. Marber, “Cardiac troponins: from myocardial infarction to chronic disease,” *Cardiovasc. Res.*, vol. 113, no. 14, pp. 1708–1718, Dec. 2017, doi:10.1093/cvr/cvx183.

[294] K. L. Becker, R. Snider, and E. S. Nylen, “Procalcitonin in sepsis and systemic inflammation: a harmful biomarker and a therapeutic target,” *Br. J. Pharmacol.*, vol. 159, no. 2, pp. 253–264, Jan. 2010, doi:10.1111/j.1476-5381.2009.00433.x.

[295] J. Kamtchum-Tatuene and G. C. Jickling, “Blood Biomarkers for Stroke Diagnosis and Management,” *NeuroMolecular Medicine*. Humana Press Inc., 01-Dec-2019.

Resum

Durant els darrers dos segles, el descobriment i la comprensió del principi de fluorescència han proporcionat nous mitjans per caracteritzar els processos físics, biològics i químics de manera no invasiva. L'espectroscòpia de fluorescència s'ha convertit en un dels mètodes més potents i àmpliament aplicats en les ciències de la vida, des de la investigació fonamental fins a les aplicacions clíniques gracies a la seva alta sensibilitat i robusta selectivitat a través d'un etiquetat específic de mostres biològiques. En particular, l'anàlisi del decaïment de la fluorescència (FLS de l'anglès, Fluorescence Lifetime Spectroscopy) també conegut com fluorescència resolta en el temps, es especialment útil a l'hora distingir les molècules d'interès d'interferències tals com la fluorescència del propi medi, i per diferenciar entre fluoròfors amb el mateix espectre d'emissió però diferents temps de vida. Encara més, l'anàlisi del decaïment de la fluorescència ens permet conèixer l'entorn immediat de la molècules, atès que molts esdeveniments macromoleculars es produeixen en la mateixa escala de temps.

Tradicionalment, l'anàlisi molecular es realitza en laboratoris equipats amb instruments de sobretaula, on tècnics especialitzats són els responsables de la realitzar de les proves. Normalment es recullen les mostres on es troba el pacient i s'envien al laboratori per analitzar-les, trigant diverses hores a completar una única prova i donar els resultats als pacients o metges. Aquest paradigma ha anat canviant en les darreres dècades, a mesura que la tecnologia de biosensor ha esdevingut tan precisa com els instruments de sobretaula, proporcionant resultats en períodes molt més curts de temps i miniaturitzant la instrumentació, traslladant les proves de diagnòstic paulatinament fora del laboratori central i cap a llocs més propers al punt d'atenció (POC, de l'anglès Point Of Care) de manera rendible.

Tot i els avantatges inherents de l'espectroscòpia de fluorescència resolta en el temps en la diagnosi molecular, no ha estat fins la darrera dècada que s'han començat a desenvolupar dispositius POC basats en la detecció de fluorescència. Això és degut al gran repte que suposa desenvolupar dispositius basats en

espectroscòpica de fluorescència portàtils d'alt rendiment i de baix cost a escala industrial.

Les dues principals limitacions tecnològiques a l'hora de miniaturitzar instrumentació per realitzar FLS les trobem tant en l'àmbit de l'electrònic com en l'òptic. En primer lloc, l'alta resolució temporal (de l'ordre de picosegons) necessària per poder mesurar el temps de vida de la fluorescència (típicament en l'escala del nanosegon 1-100 ns), requereix d'una electrònica complexa de processat i condicionament de senyal, així com per generar polsos òptics potents i de curta durada (per sota del nanosegon). En segon lloc, en els grans instruments s'empren complexos sistemes òptics amb lents i filtres per tal d'evitar que la llum del pols d'excitació arribi al detector. Tanmateix, utilitzant tècniques i tecnologies de fabricació modernes, aquesta instrumentació es pot miniaturitzar i integrar per complet, atorgant-li un gran potencial per la producció en massa i utilitat omnipresent.

Així doncs, aquesta tesi s'emmarca en l'objectiu de desenvolupar un sistema compacte de baix cost per la diagnosi basada en l'espectroscòpia de fluorescència resolta en el temps, que serveixi com a plataforma de propòsit general per a la detecció òptica de diversos biomarcadors, amb l'objectiu de construir el pont entre el laboratori i el punt d'atenció pels bioassajos basats en l'anàlisi de la fluorescència.

En particular, el sistema integrarà una matriu unidimensional de detectors capaços de detectar un sol fotó (SPAD, de l'anglés Single-Photon Avalanch Diode) amb un cartutx microfluídic intercanviable emprat per inserir la mostra, i un díode làser UV polsat de baix cost com a font d'excitació (Figura 1). Mitjançant el disseny orientat a la detecció per contacte del conjunt format pel sensor i la microfluídica, juntament amb l'operació temporitzada dels sensors, s'evita l'ús de lents i filtres. L'empaquetat a mida del xip sensor permet posicionar el cartutx microfluídic directament sobre la matriu de sensors sense cap procediment d'alineament.

DISSENY I CARACTERITZACIÓ DEL XIP SENSOR

El xip de sensors SPAD es va implementar en un procés estàndard de 0,18 μm HV-CMOS. El xip de 3,6 mm × 1,4 mm (Figura 2), conté dos circuits de matrius

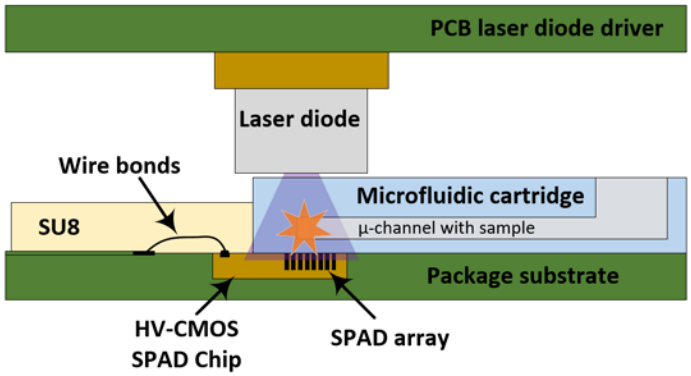

Figura 1 Esbós transversal del sistema de mesura per contacte proposat. La mostra s'introdueix en un dels microcanals del cartutx microfluídic, que es col·loca directament a la part superior de la matriu SPAD. L'encapsulat de les connexions permet posicionar la mostra d'una manera senzilla, tot evitat que la microfluídica es passi de llarg [53].

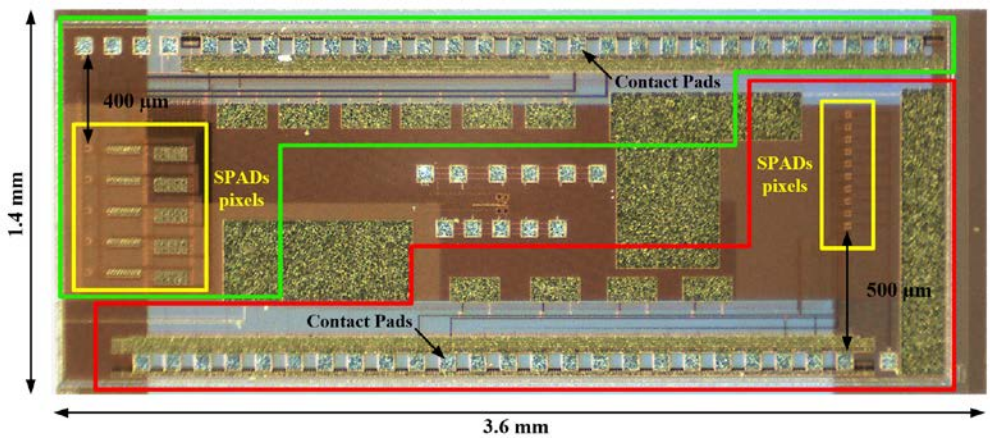

Figura 2 Fotografia de l'ASIC amb els dos circuits implementats. En vermell la matriu de 10 pixels SPAD sense circuit processat. En verd i en oposició, la matriu de 5 píxels SPAD amb clasificació del temps d'arriabada en el matix pixel. Els dos circuits tenen el primer pixel situat a 500 µm i 400 µm del límit dels contactes.

de SPAD-píxels amb diferents nivells d'integracions, destinats a mesurar la velocitat de decaïment de fluorescència de diversos fluoròfors. El primer (ressaltat en vermell) consisteix en una matriu 1-D de 10 SPAD-píxels sense cap electrònica de processament, mesurant el temps d'arribada de fotons i reconstruint l'histograma fora de xip. En canvi, el segon circuit (Figura 2, ressaltat en verd) presenta una solució nova i senzilla per detectar la fluorescència resolta en el temps, implementant una reconstrucció analògica de l'histograma de decadència en el mateix píxel. Aquest processat analògic s'ha integrat en una matriu 5 SPAD-píxels.

En ambdós circuits s'ha utilitzat el mateix SPAD-píxel operat en mode *time-gated* (Figura 3). El píxel dissenyat presenta un bona PDP (de l'anglès, PhotoDetection Probability), més del 20% a una sobretensió d'1.4 V en el rang visible (Figura 4.a), on la majoria de fluoròfors utilitzats en tècniques basades en fluorescència tenen el seu pic d'emissió. No obstant això, el soroll (DCR, de l'anglès Dark Count Rate) del detector SPAD implementat és força elevat (amb el 75% dels píxels entre 4 kHz i 8 kHz per un sobrevoltatge de 1.4 V, Figura 4.b).

El circuit d'histograma analògic implementa la tècnica de mesura *time-gating* en un SPAD-píxel analògic, classificant els temps d'arribada dels fotons per a tota la corba de decaïment de la fluorescència en el mateix xip. El circuit divideix el període de mesura en 9 finestres temps (altrament dites *bins*) i mesura simultàniament el nivell d'intensitat que correspon a cada *bin*. A més, les finestres de temps es poden ajustar entre 168 ps i 4.9 ns (Figura 5.a) cobrint així el temps de decaïment de fluorescència de la majoria dels fluoròfors emprats en FLS. Cada una de les 9 finestres de temps té una resolució màxima de 13-bits (0,16mV/fotó), per una tensió màxima d'1.3 V (Figura 5.b). El píxel complet amb el circuit d'histograma ocupa una superfície total de 150 µm x 50 µm, on el circuit de processat analògic representa el 76%, demostrant l'eficiència del disseny en termes d'àrea. La Figura 6 mostra l'arquitectura del circuit amb 5 SPAD-píxels analògics.

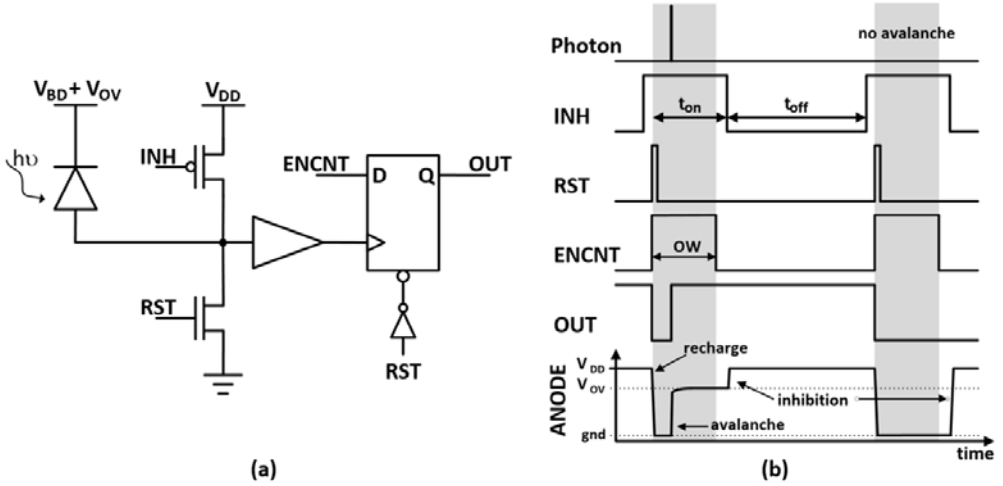

Figura 3 (a) Esquemàtic del SPAD-píxel. (b) Diagrama temporal amb les formes d'ona per operar el detector en mode time-gated.

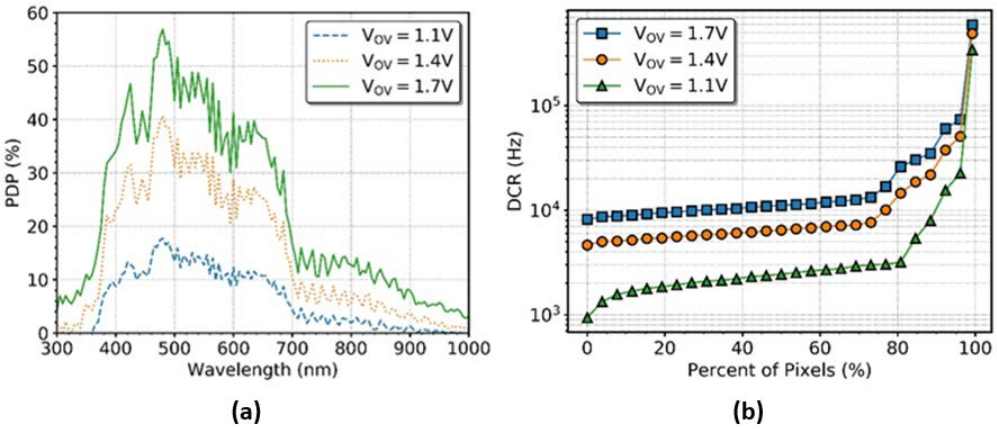

Figura 4 (a) Dependència espectral de la PDP d'un SPAD polaritzat a 1,1 V, 1,4 V i 1,7 V de sobretensió. El PDP mostra patrons d'interferència causats per les capes de passivació.

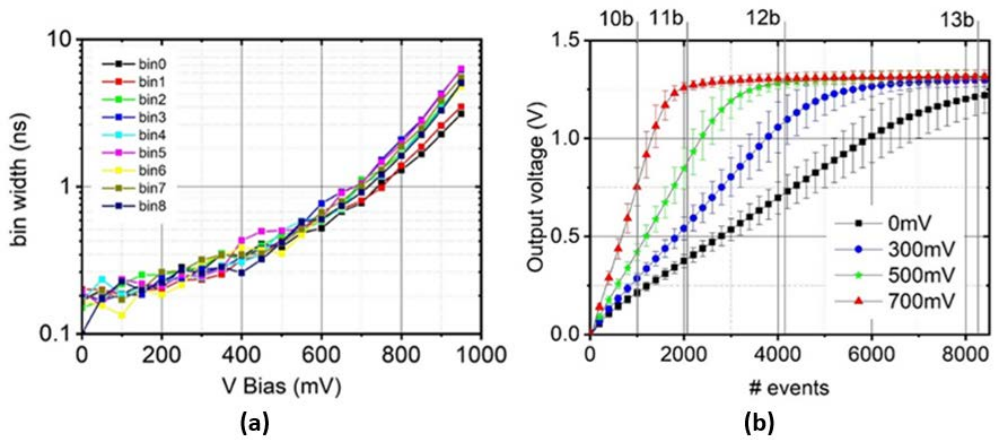

Figura 5 (a) La mitjana de l'amplada per les differents finestres de temps (bins) per a 10 xips en funció de Vbias. Per a Vbias que van des dels 150 fins als 750 mV, la desviació màxima de l'amplada del bin sempre era inferior al 10%. (b) Tensió de sortida mesurada en funció del nombre d'esdeveniments detectats per l'SPAD per diferents valors VbiasCI. Les barres d'error mostren desviacions bin-a-bin per 10 xips diferents [54].

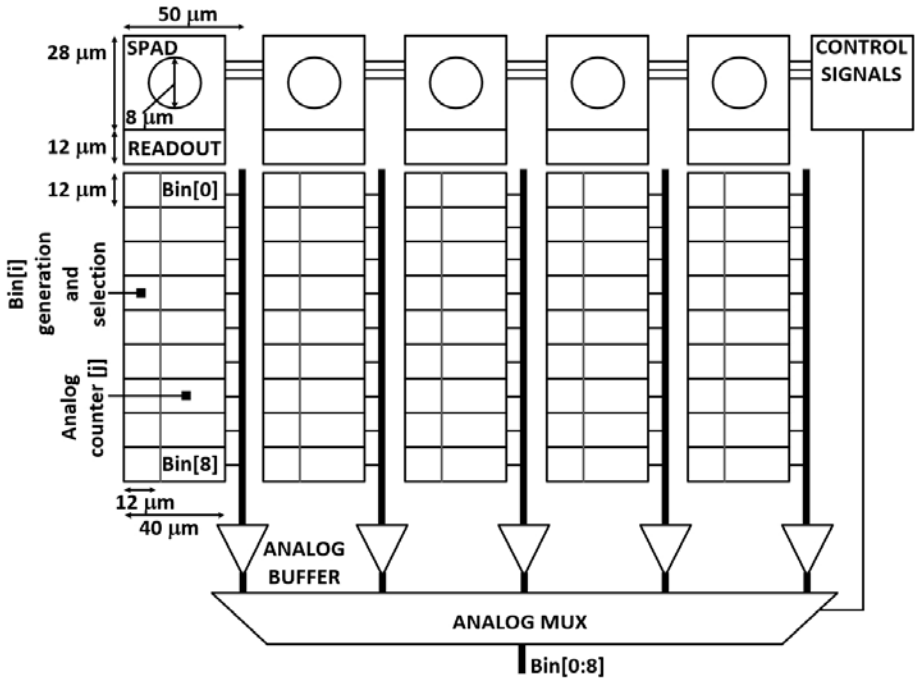

Figura 6 Arquitectura del circuit implementat de 5 SPAD-píxels amb generació histograma analògic amb les seves dimensions [54].

EMPAQUETAT DEL XIP SENSOR

El xip sensor es va muntar en una placa de circuit imprès dedicada (PCB, de l'anglès Printed Circuit Board), on es va connectar mitjançant *wire bond*. Aquesta substrat PCB tenia una obertura en la qual es podia inserir el xip. El xip es va enganxar amb una resina epoxi conductora (CW2400, Chemtronics Circuit Works) dins del rebaix deixant la seva superfície plana amb la PCB, permetent col·locar un cartutx microfluidic directament damunt seu. El SU-8 100 es va utilitzar per encapsular les conexions (Figura 7.a) i actuar com a barrera per al xip microfluídic (Figura 7 c i d).

CARTUTX MICROFLUÍDIC

Per introduir la mostra en el dispositiu es van dissenyar dos chips microfluídics de 1 i 3 microcanals en PDMS segellats amb un vidre de 150 µm d'espessor. Els microcanals estaven disposats perpendicularment a la matriu de SPADs i paral·lels

al costat llarg del xip, on es troben els contactes (Figura 7 b i c). Així doncs, l'estructura i geometria dels canals microfluídics van ser determinades per la geometria del circuit sensor i el seu empaquetat. Donat que el disseny fa que els microcanals es trobin aproximadament sobre de la matriu de SPADs, i l'amplada dels microcanals es més grans que la distancia entre SPADs, no és necessari alinear la matriu de SPADs i el conjunt de microcanals, ja que sempre hi ha un o diversos SPADs per sota (Figura 7.d).

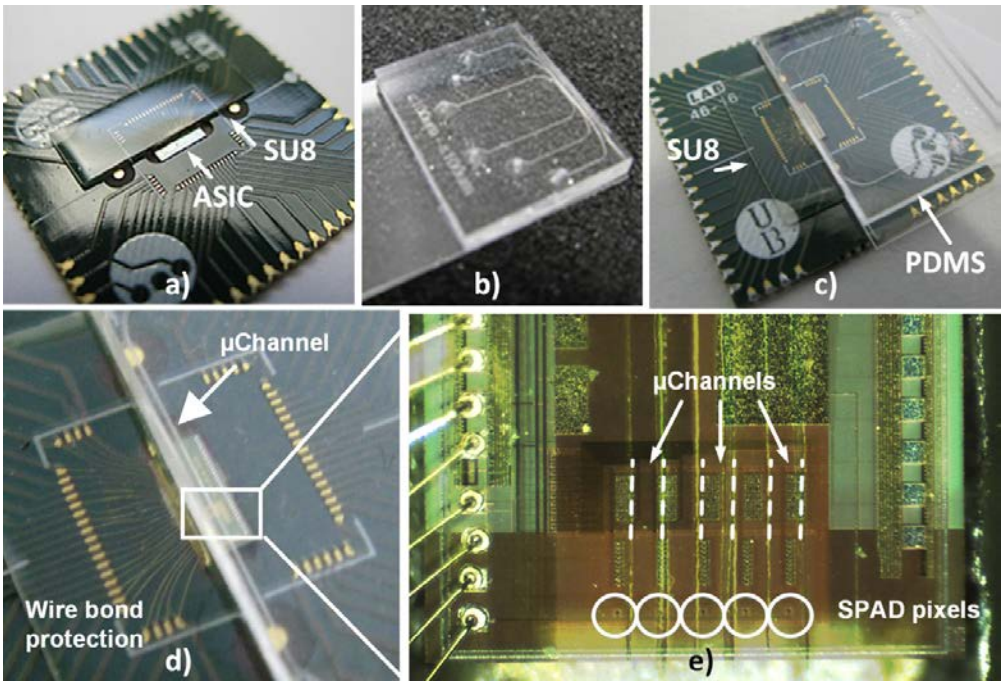

Figura 7 (a) Encapsulat del xip sensor amb el SU8 protegint les connexions entre el xip i la PCB. (b) Cartutx microfluídic de 3 canals. (c) SU-8 com a barrera per al xip microfluídic situat sobre la PCB del xip sensor. (d) Xip sensor amb un canal microfluídic al damunt. (e) Detall del xip microfluídic de tres canals sobre la matriu de 5 SPAD-píxels analògics [54].

FONT D'EXCITACIÓ

Per evitar l'ús de filtres, a més del funcionament temporitzat de l'SPAD, és necessària una font de llum que es pugui apagar ràpidament abans d'activar el detector. El temps d'apagat ha de ser el més ràpid possible per reduir el temps transcorregut

entre el pols d'excitació i la finestra d'observació, minimitzant així la pèrdua de senyal de fluorescència.

Mitjançant una revisió crítica de diferents treballs publicats sobre la generació de polsos òptics emprant LEDs i díodes làser (LD, de l'anglès Laser Diode), es van seleccionar i implementar dos circuits per polsar el díode làser de 405 nm seleccionat com a font d'excitació. Tot i que ambdós circuits són capaços de generar polsos òptics per sota de nanosegon (FWHM, de l'anglès Full Width Half Maximum), els polsos generats presentaven una cua de molt baixa intensitat, d'uns 15 ns aproximadament, que depenia principalment del díode làser.

INTEGRACIÓ I VALIDACIÓ DEL DISPOSITIU

Finalment, es van implementar dues versions del sistema de mesura (un per cada circuit implementat en el xip sensor) mostrant diferents nivells d'integració però seguint la mateixa estructura d'apilament de la Figura 1.

En ambdós sistemes es va emprar una FPGA (Zynq-7020 AP-SoC de Xilinx) per implementar l'electrònica de control i post-processat, així com la interfície de comunicació per transferir els paràmetres de la mesura i els histogrames resultants. La Figura 8 mostra una imatge del prototip final desenvolupat amb l'estructura "sandvitx" muntada sobre una placa dedicada, que està connectada a la placa de desenvolupament que conte la FPGA.

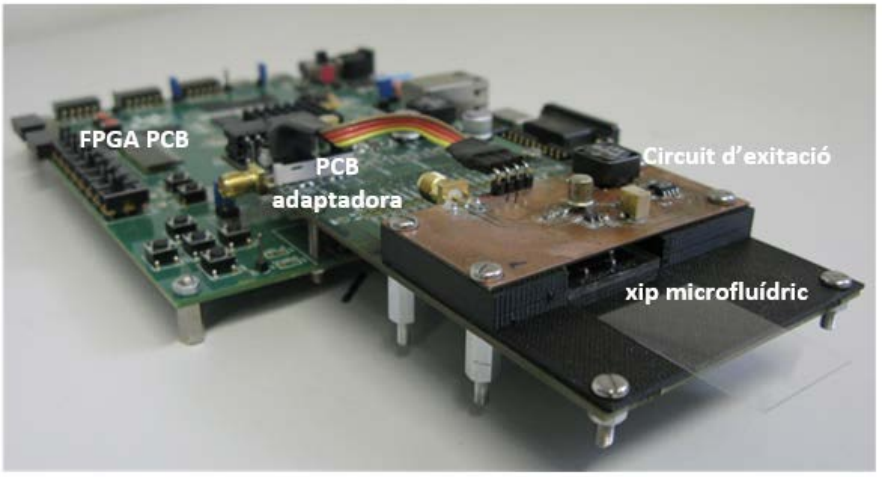

Figura 8 Imatge del prototip desenvolupat amb el cartutx microfluídic.

El primer prototip implementava la tècnica TCSPC (de l'anglès, Time-Correlated Single Photon Counting) a la Zynq-7020 per processar la sortida dels píxels de la matriu sense processat, i reconstruir d'aquesta manera, el perfil de decaïment de la fluorescència amb una resolució temporal mitja de 68 ps. La Figura 9 mostra l'arquitectura del sistema de control implementat on es realitza el processat de senyal per construir l'histograma, d'on posteriorment s'extreu el temps de vida de la fluorescència mitjançant un ajust exponencial.

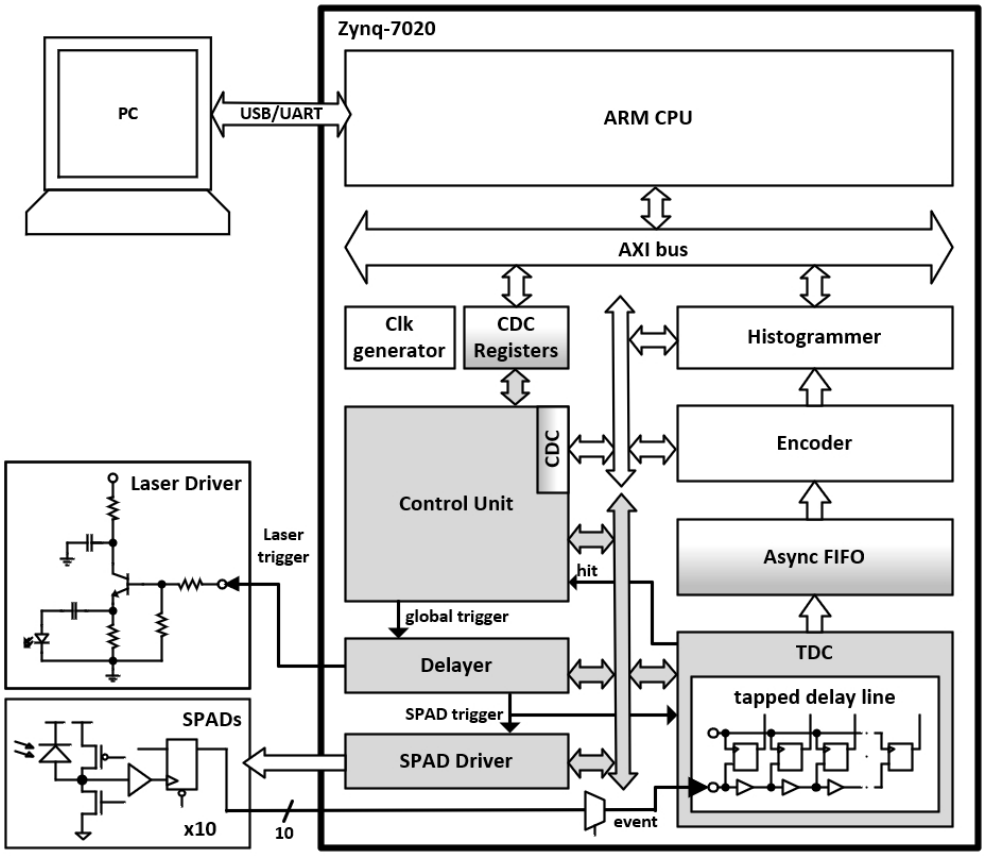

Figura 9 Arquitectura del sistema de mesura implementat a la Zynq-7020 per el primer prototip.

El segon prototip, utilitzava la matriu de SPAD-píxels analògics per reconstruir l'histograma del decaïment de la fluorescència. En aquest cas, el temps de vida s'extreu directament ajustant l'histograma generat en el chip a una corba de descomposició exponencial. La Figura 10 mostra l'arquitectura del sistema de mesura

i control implementats en la Zynq-7020, exhibint una clara simplificació en comparació amb el sistema dels SPAD-píxels sense processat. Aquesta simplificació és deguda a que la Zynq-7020 queda relegada a tasques de control de la mesura, de lectura dels histograma analògic generat mitjançant convertidors analògics-digitals (ADCs de l'anglès, Analog-to-Digital Convertes), així com de calibració i les comunicacions.

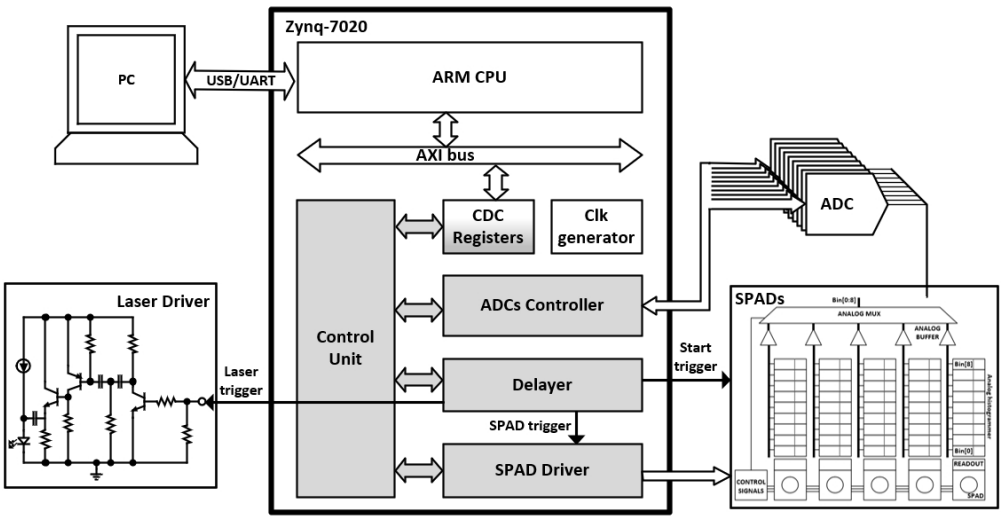

Figura 10 Arquitectura del sistema de mesura implementat a la Zynq-7020 pel segon prototip.

Les dues configuracions es van validar com a detectors de temps de vida de la fluorescència amb la configuració mostrada a la Figura 8. Es va emprar el cartutx microfluídic amb partícules fluorescents, situat entre làser d'excitació i el detector SPAD, per emular un assaig biomolecular en un dispositiu POC. En concret es van utilitzar quantum dots (QDs), que presenten un temps de vida de la fluorescència d'entre 20 i 50 ns, ideals per a sistemes basats en la temporització del sensor per treure el pols d'excitació de la finestra d'observació.

Es van realitzar experiments de dilució per concentracions d'1 µM a 31,25 nM de QDs diluits en solució salina tamponada amb fosfat (PBS PH7.4, de Gibco) que es van introduir cartutxos independents. Tots els experiments es van dur a terme en condicions que van assegurar un nombre prou baix de fotons emesos per evitar la saturació del sensor.

Els resultats van mostrar que tots dos sistemes són capaços de construir l'histograma del decaïment de fluorescència i extreure'n el temps de vida en pocs segons a partir de volums de mostres molt reduïts (20 nl, volum estimat de la mostra excitada) a nivells de concentració pràctics de 62,5 nM pel sistema basat en els SPAD-píxels sense electrònica de processat (Figura 11) i 125 nM en els SPAD-píxels amb generació d'histograma (Figura 12). La disminució del límit de detecció entre el primer i el segon dispositiu és deguda a que el circuit emprat per excitar la mostra no era el mateix per ambdós sistemes, ja que el circuit d'histograma analògic requeria una taxa de repetició alta (1 MHz) per evitar pèrdues en l'emmagatzematge dels bins analogics, a costa de genera poslos de menor potencia. No obstant això, aquest límit de detecció es pot millorar fàcilment posant la mostra més a prop, utilitzant un substrat més prim per segellar els microcanals.

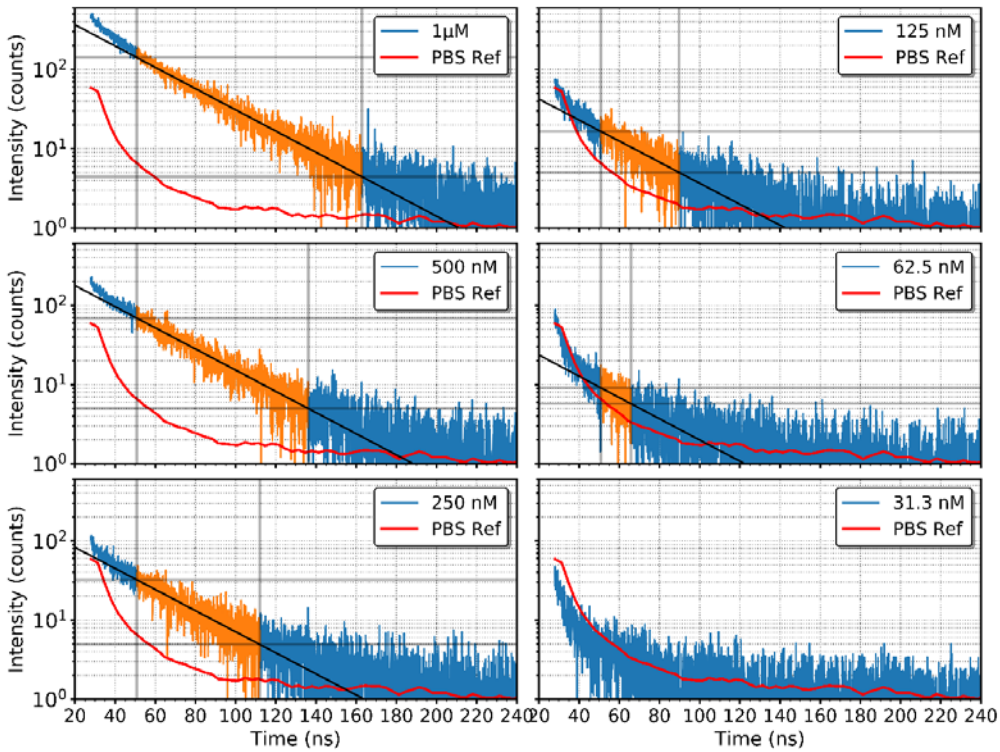

Figura 11 Ajustos mono-exponencials de les corbes de decaïment de la fluorescència mesurades per les diferents concentracions de QDs amb l'SPAD situat immediatament sota del microcanal. El temps de vida de la fluorescència obtingut és de ~32.7 ns. Els ajustos lineals i els temps de vida es van fer utilitzant només les dades ressaltades en taronja en cada cas [53].

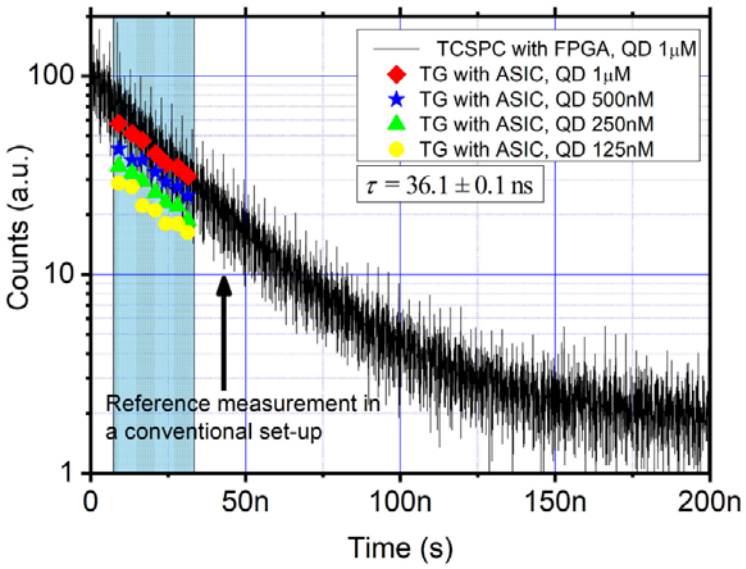

Figura 12 Ajust de la vida útil de les diferents concentracions de QDs a una corba de decaïment mono-exponencial. El temps de vida de la fluorescència obtingut va ser de ~36 ns. Els resultats es comparen amb la mesura TCSPC d'1 µM de la QDs [54].

Per altra banda, també es va estudiar la possibilitat de realitzar anàlisi simultànies utilitzant el mateix fluoròfors en diferent canals. El resultats van mostrar que no era possible, ja que la llum emesa per la mostra en un microcanal era detectada per tots els sensors de la matriu.

CONCLUSIONS

En aquest tesi s'ha demostrat que és possible desenvolupar un sistema compacte de baix cost per la diagnosi molecular basada en l'espectroscòpia de la fluorescència resolta en el temps. Per fer-ho s'ha dissenyat a mida el binomi format pel xip sensor basat en SPADs i el cartutx microfluidic, optimitzant la mesura per contacte, eliminant així els elements òptics tradicionals d'aquests tipus d'instruments. L'alt nivell d'integració aconseguit i la simplicitat en el muntatge, permeten posicionar la mostra directament sobre la matriu de sensors (a menys de 200 µm de la seva superfície) sense realitzar cap procediment d'alineament previ. A més, el dispositiu implementa la tècnica de temporització del sensor que permet prescindir de filtres. No obstant, la temporització del sensor limita el sistema a emprar marcadors fluorescents amb temps de vida llargs tals com els QDs.

Finalment, s'han implementar dues versions del sistema amb diferents nivells d'integració. El primer dispositiu empra una matriu de 10 píxels SPAD juntament amb el sistema TCSPC complet implementat en una Zynq-7020 AP-SoC (de Xilinx) per mesurar i reconstruir el perfil de decaïment de la fluorescència amb una resolució mitjana de 68 ps. En canvi, el segon dispositiu integra 5 píxels SPAD analògics amb capacitat de classificació del temps d'arribada dels fotons en el xip, on el temps de descomposició del QD es dedueix directament ajustant l'histograma generat en el mateix xip a una corba de descomposició exponencial.

Els resultats mostren que ambdós sistemes van ser capaços de construir l'histograma de la desintegració de fluorescència i mesurar la vida útil a partir de volums de mostres molt petits (20 nl) a uns nivells de concentració pràctics (de 62,5 nM i 125 nM pels circuits amb i sense generació d'histograma en el píxel, respectivament) en pocs segons. Tot i això, el límit de detecció queda determinat pel soroll del SPAD i la cua del pols de llum d'excitació, podent-se millorar fàcilment posant la mostra més a prop mitjançant un substrat més prim per segellar el xip microfluídic, per exemple amb una membrana de PDMS de 20 micres de gruix. Fins i tot amb aquestes limitacions, l'ús de components comercials combinat amb un detector de CMOS SPAD i un cartutx microfluídric d'un sol us fa que el POC sigui un sistema de baix cost amb una gran versatilitat, que ofereix un gran potencial d'aplicacions en un laboratori analític, diagnòstic clínic, al punt d'atenció o en un entorn limitat de recursos.

Finalment el camí cap a la industrialització d'aquest dispositiu passa per reduir la mida i el cost de l'electrònica satèl·lit. L'únic element no susceptible de ser directament industrialitzable és el cartutx microfluídic degut al material emprat en la seva construcció, ja que el PDMS, molt valorat en l'àmbit acadèmic per la seva simplicitat i rapidesa en prototipat, no és compatible amb els mètodes de fabricació industrial. Com alternativa industrial al PDMS proposem el Flexdym, un nou elastòmer termoplàstic (sTPE de l'anglès, soft Thermoplastic Elastomer) biocompatible, sense absorció de particules, transparent i amb baixa fluorescència, entre d'altres prestacions que és compatible amb els processos de fabricació industrials tals com el modelat per injecció o R2R (de l'anglès, Roll-to-Roll). Fora del context d'aquesta tesi es seguirà estudiant l'aplicació biomèdica dispositiu, així com la millora del límit de detecció.

List of Publications

Patents

- A. Dieguez, O. Alonso, J. Canals, and E. Vilella, “Signal processing method for histogram generation, and corresponding device and use,” PCT/EP2016/075211, 2017.

Journals Articles

- J. Canals, N. Franch, O. Alonso, A. Vilà, and A. Diéguez, “A Point-of-Care Device for Molecular Diagnosis Based on CMOS SPAD Detectors with Integrated Microfluidics,” Sensors, vol. 19, no. 3, p. 445, Jan. 2019. doi:10.3390/s19030445
- A. Dieguez, J. Canals, N. Franch, J. Dieguez, O. Alonso, and A. Vila, “A Compact Analog Histogramming SPAD-Based CMOS Chip for Time-Resolved Fluorescence,” IEEE Trans. Biomed. Circuits Syst., vol. 13, no. 2, pp. 343–351, Apr. 2019. doi:10.1109/TBCAS.2019.2892825

Conferences Proceedings

- J. Canals, N. Franch, O. Alonso, A. Vilà, and A. Diéguez, “A Portable Fluorescence Lifetime Spectroscopy Detector for Molecular Diagnosis,” Proceedings, vol. 1, no. 8, p. 758, Nov. 2017. doi:10.3390/proceedings1080758
- Franch, N., Alonso O., Canals, J., Vilà A., A., Diéguez, A., “A low cost fluorescence lifetime measurement system based on SPAD detectors and FPGA processing,” in Journal of Instrumentation, 2017, vol. 12, no. 02, pp. C02070. doi:10.1088/1748-0221/12/02/C02070.
- N. Franch, O. Alonso, J. Canals, A. Vila, A. Herms, and A. Dieguez, “A low cost fluorescence lifetime measurement system based on SPAD detectors and FPGA processing,” in 2016 Conference on Design of Circuits and Integrated Systems (DCIS), 2016, pp. 1–6. doi:10.1109/DCIS.2016.7845266

Conferences Contributions

- Dieguez, A, Canals, J., Franch, N., Moro, V., Alonso, O. Vilà, A. 'A miniaturized and low-cost sub-nanosecond fluorescence lifetime detector based on and array of CMOS SPAD detectors,', 28th Biosensors 2018, Miamí, USA.
- Canals, J., Franch, N., Alonso, O., Vilà, A., Diéguez, A. 'A portable fluorescence lifetime spectroscopy detector for molecular diagnosis' 5th International Symposium on Sensor Science. Barcelona, Spain, 2017 (Poster)
- Diéguez, A.; Canals, J.; Franch, N.; Diéguez, J.; Alonso, O.; Moreno, M.; Vilà, A. 'A compact lifetime fluorescence detector for clinical diagnosis' International Conference on Bio-Sensing Technology, Riva del Garda, Italy, 2017 (Poster)
- Franch, N.; Alonso, O.; Canals, J.; Vilà, A.; Diéguez, A. "A low cost fluorescence lifetime measurement system based on SPAD detectors and FPGA processing" Proceedings of the International Workshop On Radiation Imaging Detectors (IWORID2016), Barcelona, Spain, 2016 (Poster)